Doctoral Thesis

Experimental and Computational Approaches for Prevention and Remediation of Gas Hydrates in the Presence of Novel Inhibitors

Dongyoung Lee

Department of Urban and Environmental Engineering
(Environmental Science and Engineering)

Ulsan National Institute of Science and Engineering

2021

Experimental and Computational Approaches for Prevention and Remediation of Gas Hydrates in the Presence of Novel Inhibitors

Dongyoung Lee

Department of Urban and Environmental Engineering
(Environmental Science and Engineering)

Ulsan National Institute of Science and Engineering

Experimental and Computational Approaches for Prevention and Remediation of Gas Hydrates in the Presence of Novel Inhibitors

A thesis/dissertation submitted to
Ulsan National Institute of Science and Technology
in partial fulfillment of the
requirements for the degree of
Doctor of Philosophy

Dongyoung Lee

12. 15. 2020
Approved by

_____

Advisor
Yongwon Seo

Experimental and Computational Approaches for Prevention and Remediation of Gas Hydrates in the Presence of Novel Inhibitors

Dongyoung Lee

This certifies that the thesis/dissertation of Dongyoung Lee is approved.

12. 15. 2020

Signature

_____

Advisor: Yongwon Seo

Signature

_____

Young-Nam Kwon

Signature

_____

Sung-Deuk Choi

Signature

_____

Hoi Ri Moon

Signature

_____

Seungmin Lee

ABSTRACT

This dissertation investigated the synergistic inhibition effect of gas hydrate inhibitors, newly designed gas hydrate inhibitors, and gas hydrate remediation method development for the field of production chemistry of flow assurance. In order to perform above research topics, fundamental experimental studies of thermodynamic stability, structural analysis, gas uptakes, cage-filling molecular behaviors in the presence inhibitors were examined with computational methods and tried to synthesize eco-friendly and innovative gas hydrate inhibitors. The sigma (σ) profiles of inhibitor molecules obtained from the Conductor-Like Screening Model for Real Solvents (COSMO-RS) software were used to estimate inhibitor–water interactions for the pre-screening of potential inhibitors. From the σ profile results, candidates for thermodynamic hydrate inhibitor (THI) and kinetic hydrate inhibitor (KHI) were selected. In addition, the stability conditions in the presence of various inhibitors show that thermodynamic inhibition effect is related to molecular interaction between water and inhibitor. As is well known, intrinsic properties and the number of inhibitors are the biggest factors influencing the thermodynamic inhibition effect. Thus, even if two or more inhibitors mixed, it is hard to observe thermodynamic synergistic inhibition effect. Moreover, inhibitors hard to enclathrated in the gas hydrate structure because their sizes are too large (van der Waals radius values), so they reside on the outside of the cages or are partly involved in cages to disrupt the water-water networks. Furthermore, kinetic analyses were conducted to observe kinetic inhibition effect regarding onset temperature, growth rates and conversion of water into gas hydrates. It was confirmed that different results of onset temperature, growth rates and conversion of water into gas hydrates are shown according to types of inhibitor and inhibitor mixtures. Therefore, density functional theory (DFT) calculation, quantum theory of atoms in molecules (QTAIM) calculation, fourier-transform infrared (FT-IR) spectroscopy, and in-situ Raman spectroscopy were used to demonstrate inhibition mechanisms of each inhibitor. The DFT and QTAIM calculations indicated that each inhibitor has different interaction energy with cage, and the smaller negative interaction energy means that inhibitor significantly retards gas hydrate formation. The FT-IR was used to investigate the interaction sites of inhibitors toward water and find the peak shifts to observe the hydrogen bonding sites. In particular, in-situ Raman analysis verified inhibition mechanisms of inhibitors during nucleation and formation process, thus delaying behaviors of cages could be observed directly. The overall experimental and computational results in this dissertation provide invaluable information of THI and KHI, thus can contribute to the opening up a new field for flow assurance in oil and gas industries and CO_2 storage process.

TABLE OF CONTENTS

4.2.3. Sigma Profiles of potential inhibitors · · ·

List of Figures

List of Tables

Chapter 1. Introduction

1.1. Introduction of Gas Hydrates

1.1.1. Gas hydrate structures

Gas hydrates are ice-like inclusion crystalline compounds consisting of water molecules which form cages from hydrogen bonding with guest molecules such as methane, carbon dioxide, and nitrogen, trapped in the cages (Figure 1.1.1.). These cages are stabilized by van der Waals interactions between the small gas molecules (guests) and water molecules (hosts) [1-3]. Hydrate structures are generally divided into three types: structure I (sI), structure II (sII) and structure H (sH), and the hydrate structure depends on pressure, temperature, and guest molecule properties [1]. There have been many studies on sI and sII and as the sH hydrate is found in nature, many studies on sH are underway. The unit cell of the sI hydrate consists of 2 small (5^{12}) and 6 large ($5^{12}6^2$) cages. The unit cell of sII and sH hydrate consists of 16 small (5^{12}) and eight large ($5^{12}6^4$) cages, and 3 small (5^{12}), 2 medium ($4^3 5^6 6^3$) cages, and 1 large ($5^{12}6^8$) cage, respectively [1-3]. In general, small gas molecules such as methane and carbon dioxide form sI hydrates with the range of 4.2 and 6.0 Å. However, when the size of the guest is larger than 6.0 Å (propane, tetrahydrofuran), or much smaller gas molecules such as nitrogen and oxygen (guest size < 4.2 Å), form sII hydrates. In contrast to sI and sII hydrates, structure H hydrate needs large-sized guest molecules such as neohexane, methylcyclopentane (7.0 Å < guest size) with small-sized gas molecules, which were known as help gas (e.g. Xe, H_2, and CH_4) to stabilize the crystal structure. The representative gas hydrate structures and geometric crystallographic information are summarized in Figure 1.1.2. and Table 1.1.1.

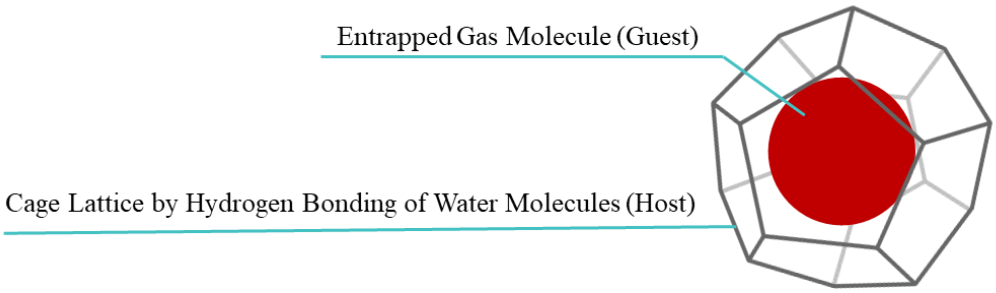

Water molecules form hydrogen-bonded frameworks where guest molecules are trapped.

[High(↑) Pressure and Low (↓) Temperature conditions]

Figure 1.1.1. Gas hydrate explanation.

Table 1.1.1. Geometry and Crystal cell structure.

Structure	**I**		**II**		**H**		
Crystal system (space group)	Cubic (Pm3n)		Cubic (Fd3m)		Hexagonal (P6/mmm)		
Cavity	small	large	small	large	small	medium	large
Number of cavities for unit cell	2 5^{12}	6 $5^{12}6^2$	16 5^{12}	8 $5^{12}6^4$	3 5^{12}	2 $4^35^36^3$	1 $5^{12}6^8$
Ideal unit cell formula	$6(5^{12})\cdot2(5^{12}6^2)\cdot46H_2O$		$16(5^{12})\cdot8(5^{12}6^4)\cdot136H_2O$		$3(5^{12})\cdot2(4^35^36^3)$ $1(5^{12}6^8)\cdot34H_2O$		
Average cavity radius (Å)	3.95	4.33	3.91	4.73	3.94	4.04	5.79
Lattice parameters	a = 12 Å $\alpha = \beta = \gamma = 90^\circ$		a = 17.3 Å $\alpha = \beta = \gamma = 90^\circ$		a = 12.2 Å c = 10.1 Å $\alpha = \beta = 90^\circ, \gamma = 120^\circ$		
Number of water molecules per cavity	20	24	20	28	20	20	36

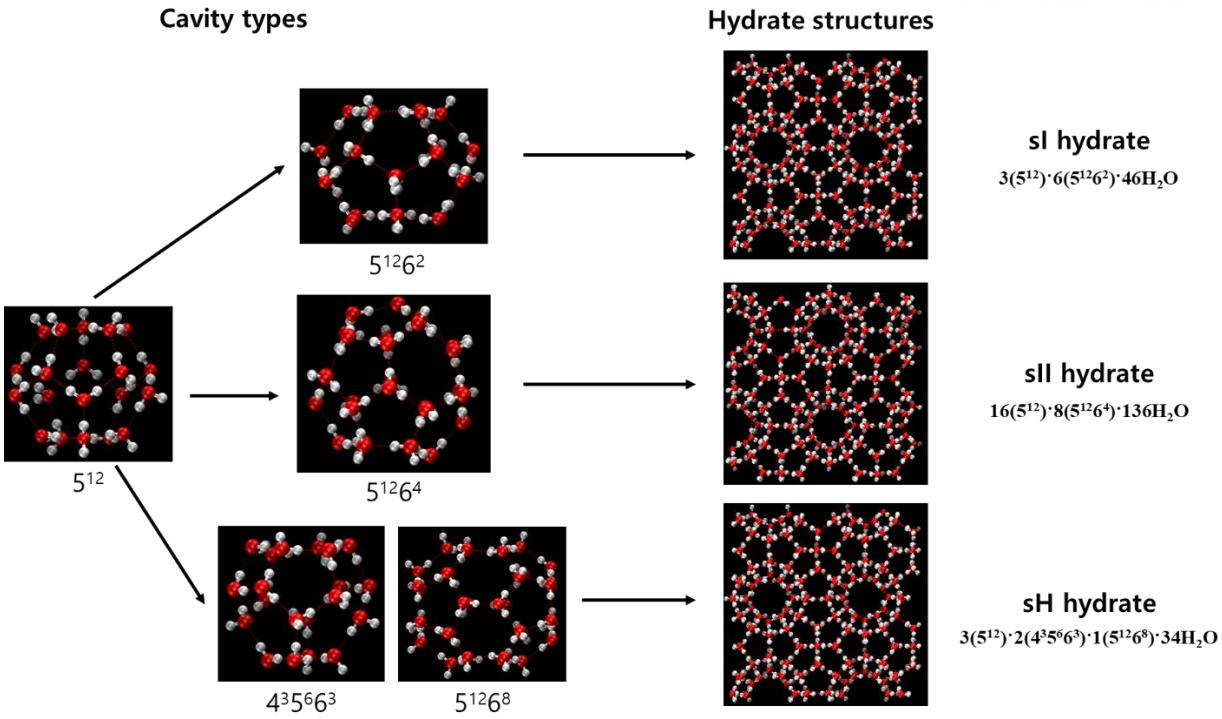

Figure 1.1.2. The representative gas hydrate structures.

1.1.2. Gas hydrate applications: flow assurance

Gas hydrates have been utilized in various fields: from exploitation of naturally occurring gas hydrates, natural gas storage and transportation, carbon dioxide capture and storage, to desalination [4-20]. However, gas hydrates often cause major problems in the petroleum and gas industries during gas and oil transportation through pipelines. Notably, prevention and management of gas hydrates in the production and transportation of hydrocarbon fluids, like natural gas and oil, are crucial, because gas hydrate formation can create a risk of explosion and enormous financial losses [21-24]. The condition of natural gas transportation is a favorable condition (low temperature, high pressure) for gas hydrate formation, resulting in pipeline plugging which can lead to the risk of explosion and enormous financial losses. Thus, prevention and management of gas hydrates in production and transport is one of the key areas in flow assurance. There are several methods to prevent gas hydrate formation and deposition including heating, injection of thermodynamic hydrate inhibitors (THIs) and low-dosage hydrate inhibitors (LDHIs), complete removal of water (dehydration), and modifying the gas phase with another gas. Among them, injection of thermodynamic hydrate inhibitors (THIs) and low-dosage hydrate inhibitors (LDHIs) is a promising technology to prevent pipeline plugging [25-30].

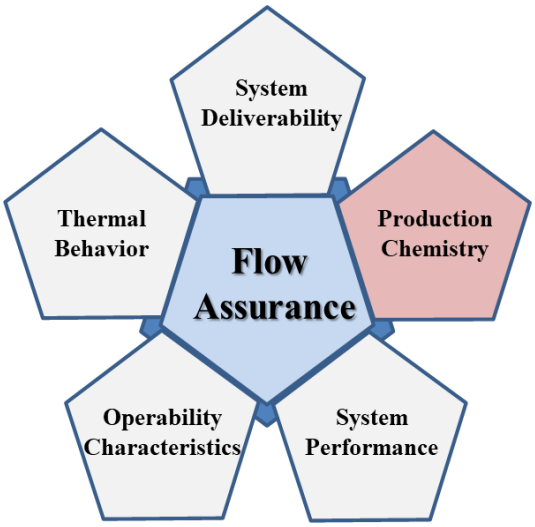

Pipeline Flow Assurance

Flow Assurance is now synonymous with wide range of issues, for example :

- **System Deliverability** : pressure drop versus production, pipeline size & pressure boosting.
- **Thermal Behavior** - temperature changes, insulation options & heating requirements.
- **Production Chemistry** - hydrates, waxes, asphaltenes, scaling, sand, corrosivity & rheology.
- **Operability Characteristics** - start-up, shut down, transient behavior(e.g. slugging etc.).
- **System Performance** - mechanical integrity, equipment reliability, system availability etc.

Figure 1.1.3. Explanation of flow assurance issues.

1.2. Gas Hydrate Inhibitors

1.2.1. Thermodynamic Hydrate Inhibitors (THIs)

Lab-scale research on gas hydrates has moved to the industrial scale due to the formation of gas hydrates in natural gas transmission pipelines and consequent blockage [24, 31]. Hammerschmidt reported problems of gas hydrate formation in the natural gas industry, which gave rise to industrial investment and the investigation of gas hydrate properties, such as composition, structure, formation conditions, and the applications of inhibitors [31]. At present, gas hydrates are still considered a hindrance to the oil and gas industry because the failure of gas hydrate prevention and management leads to significant safety concerns and enormous financial losses [21, 23, 32].

Transporting oil and gas have to be operated very carefully to avoid the gas hydrate formation as they are considered the largest concern at production chemistry in Figure 1.1.3. For many years, industries try to prevent hydrate-related risks has been the injection of thermodynamic hydrate inhibitors (THIs) at the wellhead (high concentrations 20-50 wt%), commonly methanol or mono-ethylene glycol (MEG) with salts (NaCl), to reduce water activity and shift hydrate formation regions to harsh conditions represented by higher pressure and lower temperature [21, 24], so that the operating conditions of offshore flowlines are outside of the hydrate formation conditions. However, THIs require high concentrations (20–50 wt%) in solutions to completely prevent gas hydrate formation, which results in high operational costs and environmental problems [33-35]. Furthermore, as the oil and gas industries are encountering more challenging conditions such as deeper waters, longer subsea tiebacks, and higher water cuts for the exploration and exploitation of hydrocarbons, pilot experiments are needed for the managing of gas hydrate formation in pipelines [21, 24-25, 35-36].

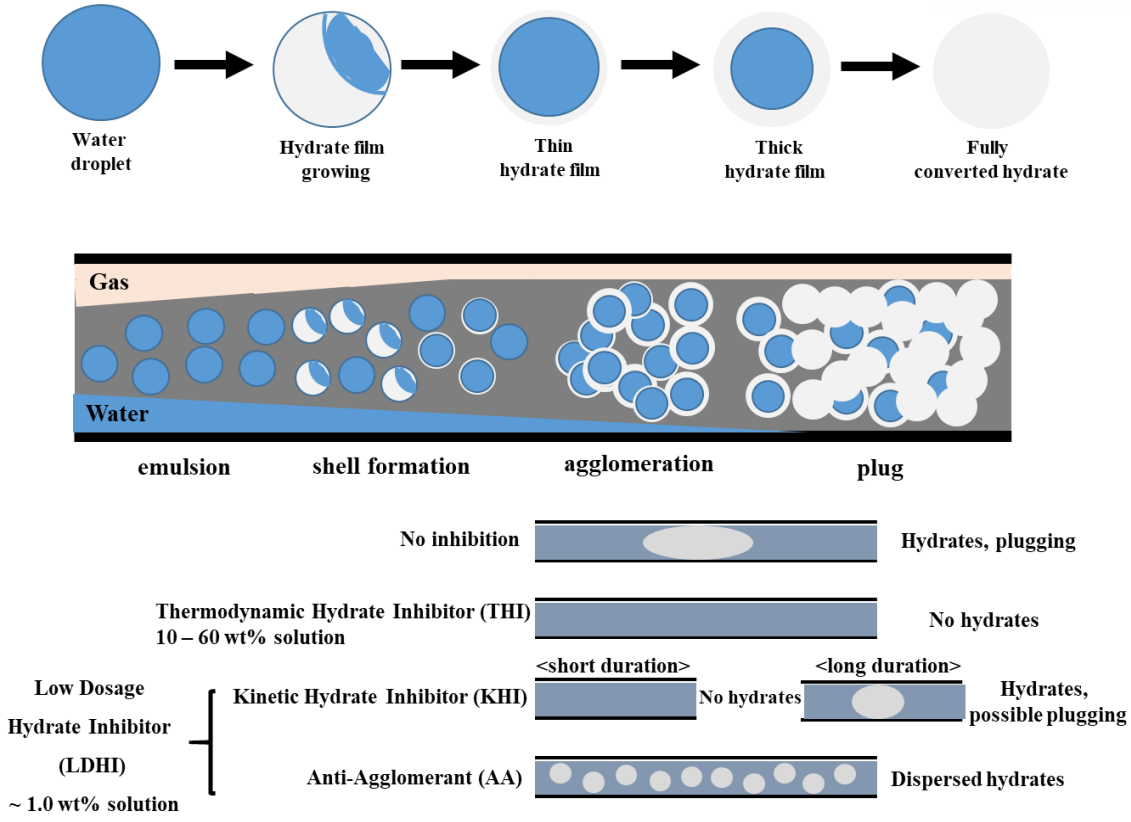

Figure 1.2.1. Explanation of gas hydrate inhibitors.

The addition of THIs can shift gas hydrate equilibrium curves to lower-temperature or higher-pressure regions and, thus, the insides of the pipelines can become thermodynamically unstable regions of gas hydrates. However, THIs should guarantee gas hydrate formation beyond gas hydrate-stable regions.

A THI, methanol, and MEG, have been widely used to prevent hydrate formation in extraction wells and pipelines for oil and gas over half a century because of low cost, and it has well established thermodynamic models are available for predicting the amount of THI required for hydrate prevention. However, environmental concerns about THI usage have been aroused because huge quantities of THI, which is flammable, toxic, and corrosive, are required for thermodynamic inhibition of gas hydrates, and particularly, the methanol used is rarely regenerated continuously in condensate and gas fields [24, 29, 37]. A new generation of THIs, which are effective and environmentally friendly, should therefore be identified and developed to meet stricter environmental regulations. Unlike THIs, much lower concentrations (usually l.0 wt%) are required for LDHIs.

1.2.2. Low Dosage Hydrate Inhibitors (LDHIs)

Low-dosage hydrate inhibitors (LDHIs) are alternatives to THIs and have been attracted researchers and industry for almost two decades. These inhibitors are known to be more effective, more environmental friendly, less corrosive and have lower capital and operational expenses even at low concentrations (usually 0.1 ~ 1 wt%). These inhibitors are usually classified to kinetic hydrate inhibitors (KHIs) and anti-agglomerants (AAs) [25, 28, 30, 38-39]. Most important issues for designing LDHIs are as follows: degree of sub-cooling, water cut (oil-water), salinity, gas composition, economical evaluations, safety, environmental issues, etc.

KHIs affect the induction time, delay nucleation, or slow down the crystal growth by prolonging the induction time of hydrate formation more than the residence time of free water in the pipeline. Poly(N-vinylpyrrolidone) (PVP) is a first-generation commercially available water-soluble polymer and poly(N-vinylcaprolactam) (PVCap) is a well-known KHIs for the oil and gas industry, in a hydrocarbon transport line [40-41]. Compared to KHIs, AAs allow gas hydrate formation, but they prevent the agglomeration and accumulation of gas hydrates into large masses, thereby resulting in effective at very high sub-cooling or shut-in conditions. Typical AAs are surfactants such as alkylsulfonic compounds and quaternary ammonium salts such as tetra-n-butylammonium bromide (TBAB) and tetra-n-butylammonium chloride (TBAC) [42-44]. Because KHIs retard hydrate nucleation and formation at low dosages (0.1–1 wt%), they can be advantageous with respect to the economy and environment due to their lower operational costs and reduced risk of spillage [38-39].

Several inhibition mechanisms of KHIs have been proposed from molecular dynamics (MD) [35, 45-48]. One of the proposed mechanisms is the adsorption of KHIs onto gas hydrates. The heterocyclic ring mainly contributes to adsorption and can preferentially adjust itself to come into contact with a hydrate semi-large-cage ($5^{12}6^2$). The polymer chain then stretches over the surface of gas hydrates, thereby inhibiting further growth [48-49]. However, it is not clear whether the properties of KHIs at the immobile interface (MD condition) are similar to those at the growing hydrate interface (experimental condition). Although the KHIs with limited concentrations have shown effective performance in delaying or retarding gas hydrate formation, they cannot ensure the reliable, long-term prevention of pipeline plugging. Many gas and oil companies therefore still use THIs or THI/KHI blends to avoid gas hydrate formation in subsea pipelines [21, 31-32].

However, there are still little experiments on the material understanding, environmental verification, certainty of the result, mechanism proof, and synergistic effect of gas hydrate inhibitors. Therefore, it is required to develop efficient research for gas hydrate inhibition phenomena using potential inhibitors

for application to flow assurance. From this respect, the following research topics are defined to help the basic research of this field.

1.3 Gas Hydrate Inhibitor suggestions for Gas and Oil Industries

Figure 1.3.1. Research objectives.

In this study, three different approaches (inhibition mechanisms, materials, systems) were investigated to verify the inhibition mechanisms of current inhibitors, and apply novel inhibitors in various environment. First, amino acids and ionic liquids were selected to verify the inhibition mechanisms because they are commonly studied as green hydrate inhibitors. In order to measure their thermodynamic and kinetic properties, stability conditions, structure characteristic, gas uptakes, cage-filling behaviors, onset temperatures were identified. Moreover, the computational methods such as Gaussian, COSMO-RS, QTAIM, molecular dynamic (MD) studies were combined with experimental methods to interpret the molecular inhibition mechanisms.

1.3.1. Amino Acids, Ionic Liquids, and their mixtures

Ionic liquids and amino acids have recently been introduced as green hydrate inhibitors, as well as dual function inhibitors, because they are environmentally friendly and have shown good performance as both THIs and KHIs [33-34, 36-37, 50-51]. Ionic liquids are salts that are generally composed of heterocyclic cations and inorganic anions. Ionic liquids are water-soluble, nonvolatile, and less toxic than methanol, and the thermodynamic inhibition performance of some ionic liquids is comparable to that of methanol [36, 37]. Ionic liquids are therefore good alternatives to methanol as THIs.

Also, ionic liquids can significantly retard hydrate nucleation and growth because cations and anions move freely around the solution and form hydrogen bonds with water molecules to interrupt hydrate nucleation and growth as KHI [36-37, 41].

Amino acids are organic compounds whose key elements are carbon (C), hydrogen (H), oxygen (O), and nitrogen (N), and which participate in the formation of human muscles and other tissues in the form of proteins. Amino acids can also readily form hydrogen bonds with water molecules because they consist of both amine ($-NH_2$) and carboxyl (-COOH) functional groups and have strong potential as THIs and KHIs. Their performance was comparable to that of conventional inhibitors owing to their strong hydrogen bonding capacity and zwitterionic nature. The inhibition mechanism of amino acids is associated with the perturbation of water molecules. It has been suggested that the perturbation of the local water structure caused by hydrophilic functional groups and hydrophobic side chains of amino acids increases the barrier to nucleation for gas hydrates [33-34, 51-52].

In this chapter, we focus on amino acids and ionic liquids as synergists. From the experimental and computational methods, the inhibition mechanisms of each inhibitor are verified. Then, the synergist effect of amino acid (glycine) + ionic liquid ([BMIM][BF_4]) was investigated as THI and KHI. From the results, the method of gas hydrate inhibition mechanism regarding synergistic effect was firstly introduced and it seems that the inhibition effect of synergist is similar as methanol (THI) and better than PVCap (KHI).

Second, we synthesized novel inhibitors such as MOF, DES, and FAN by applying new concepts. The following inhibitors have not yet been proposed as gas hydrate inhibitors, and since each material has physical and chemical advantages, it is necessary to study as a material that can replace the existing inhibitor for future applications.

1.3.2. Metal Organic Framework (MOF)

Metal–organic frameworks (MOFs) are a suitable class of materials for developing recoverable KHIs because they can be easily decorated with functional groups that interact strongly with water molecules [53-55]. UiO-66, which consists of $Zr_6O_4(OH)_4$ nodes and 1,4-benzenedicarboxylic (BDC) linkers, is the one of the best MOF candidates owing to its excellent thermal, aqueous, physical, and chemical stabilities [56-57]. In addition, several UiO-66 derivatives can be synthesized with BDC linkers substituted with other functional groups such as hydroxy, amine, halogen, and nitro [58-60]. In this work, to introduce a functionality capable of forming H-bonds with water molecules, UiO-66 derivatives with amine- and hydroxy-substituted BDC linkers (UiO-66-NH_2 and UiO-66-OH) were examined as KHIs and their performance was compared with that of PVP as an existing KHI and that of nonfunctionalized UiO-66. Moreover, the recovery of a MOF-based KHI was achieved by constructing a core–shell composite with magnetic Fe_3O_4 nanoparticles (NPs), and reusability was also

confirmed without a reduction in performance. This is the first attempt to develop recoverable and recyclable MOF-based KHIs.

1.3.3. Deep Eutectic Solvent (DES)

Choline chloride (ChCl) is a cheap, easily biodegradable ionic liquid that is safe for the environment compared to other ionic liquids [61]. Urea is an organic compound with the chemical formula of $CO(NH_2)_2$ that has two kinds of functional groups ($–NH_2$ and C=O) and is the main nitrogen-containing substance in the urine of mammals [63]. These two eco-friendly substances have been proven to function as THIs for CH_4 hydrates [61-64]. In addition, the mixture of ChCl and urea has an additional advantage over each single component in that it makes a deep eutectic solvent (DES) [65-66]. DESs are promising novel substances that can be used in many applications as solvents, reagents, and catalysts. They also have great potential for use as effective and eco-friendly THIs because they have functional groups capable of forming hydrogen bonds with water, have low toxicity, are biodegradable, and exhibit negligible vapor pressure [65-67]. DESs are generally formed by mixing hydrogen-bond donors (HBDs) with hydrogen-bond acceptors (HBAs), and their melting point is significantly lower than that of each of the original HBAs and HBDs [65-66]. Besides, regardless of the original phase of the HBAs and HBDs, formed DESs exist in a liquid state at room temperature, which makes it advantageous for DESs to be used as THIs in terms of handling, transport, and injection [65-66].

In this study, thermodynamic inhibition effects of ChCl, urea, and their mixture (DES) on CH_4 hydrates were investigated by adopting both experimental and computational approaches. σ-profiles of water, ChCl, urea, and DES were obtained using the COSMO-RS software to estimate the polarity of each substance. DES was synthesized from ChCl and urea, and its melting point was measured using a HP μ-DSC. The three-phase (gas hydrate (H) – liquid water (L_w) – vapor (V)) equilibria of CH_4 hydrates in the presence of ChCl (1.0, 3.0, and 5.0 mol%), urea (1.0, 3.0, and 5.0 mol%), and DES (3.0 mol%) were measured using a high-pressure autoclave to examine the equilibrium temperature shifts caused by the addition of potential THIs. Furthermore, hydrogen bond energy at (3, -1) BCPs between water molecules in hydrate cages and inhibitor molecules (ChCl, urea, and DES) was calculated using the QTAIM method.

1.3.4. Fused Aromatic Network (FAN)

As one of unique subclass of COFs (Covalent Organic Frameworks), FANs (Fused Aromatic Networks) have attracted considerable attention due to their outstanding physiochemical stability coming from structural nature [67-69]. Their organic building blocks are periodically incorporated into network structures with fully fused aromatic rings without rotatable single-bond connectivity, which endow them with extraordinary stability against hydrolysis and novel electronic properties. Hence, a number of FAN

structures have been reported as promising materials for practical applications in energy conversion and storage, electronics, gas storage and the uptake of hazard chemicals.

we employed two kinds of novel FAN materials as KHIs which are intriguing three-dimensional (3D) pyrazine-based FAN structure (3D-CON) and poly(benzimidazobenzophenanthroline)-based FAN structure (V2D-BBL structure) [70-71]. Both materials have been successfully synthesized via simple wet-chemical reaction as gram-scale and exhibited not only superior stability against moisture, heat and chemicals, but also high surface area with remarkable gas storage performances.

Especially, V2D-BBL structure has pyrrolidone moiety which is structurally similar to lactam-based PVCap. As a result, the V2D-BBL revealed comparable performance as methane hydrate inhibitor and was superior as carbon dioxide hydrate inhibitor compared to PVCap. Moreover, prepared FAN structures exhibited better biodegradability compared to PVP and PVCap, which suggests again designed FAN structures can be promising alternative of commercial polymers. As a result, the present work provides a new avenue to design and develop a novel class of KHI materials that have not been studied to date.

Overall, the outcomes and findings of novel gas hydrate inhibitors broadens the practical applicability of each material and may contribute to lessening the environmental impact of gas hydrate inhibitors for flow assurance in oil and gas pipelines.

Chapter 2. Experimental Investigation

2.1. Materials

CH_4 gas with a purity of 99.95% was supplied by MS Gas Co. (Republic of Korea). The two ionic liquids, 1-butyl-3-methylimidazolium tetrafluoroborate ([BMIM][BF_4], 97%) and 1-butyl-3-methylimidazolium iodide ([BMIM][I], 98%), were obtained from Merk KGaA (Germany). Two amino acids (glycine and alanine) with 99% purity were purchased from Sigma-Aldrich Chemical Co. (USA). Methanol with 99.5% purity was supplied by Samchun Pure Chemical Co. (Republic of Korea). PVCap (Mw = 5000 and polydispersity = 1.303) with a purity of 98% was obtained from Luviskol PlusTM (BASF, Germany), which is a solution of PVCap (60 wt%) and ethanol. Double-distilled deionized water was used in this study.

2.2 Experimental Apparatus and Procedure

2.2.1 Thermodynamic method

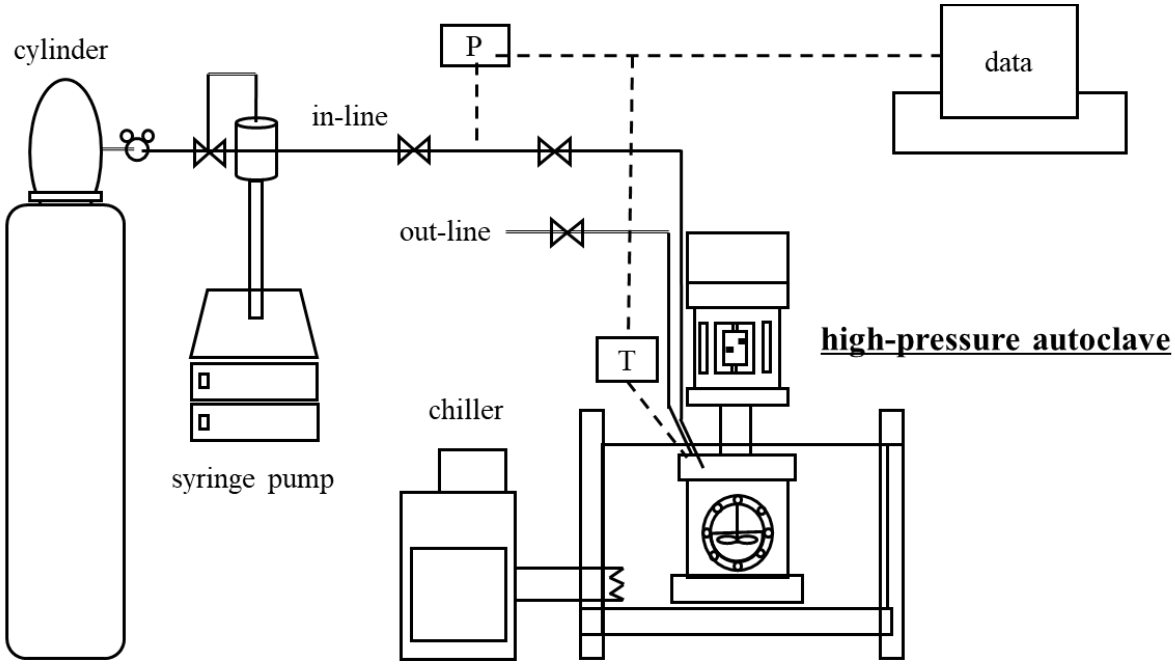

Figure 2.2.1. High-pressure autoclave

To measure the hydrate phase equilibria, the equilibrium cell was charged with 35-50 cm^3 of inhibitor solution (3.0 mol%). A specially designed equilibrium cell, made of 316 stainless steel, was used. The cell had an internal volume of approximately 150 cm^3 and was immersed in a water bath, whose temperature was controlled by an external circulator (RW-2025G, JEIO Tech, Republic of Korea). The solution containing inhibitors was vigorously agitated by an impeller-type stirrer during all experiments. A resistance temperature detector (RTD) sensor, calibrated from 268.15 to 305.15 K using an ASTM 63C (H-B Instrument Company, USA) with an accuracy of ± 0.02 K, was used to measure the temperature of the cell. A pressure transducer (S-10, WIKA, Germany) was used to measure the pressure of the system and calibrated using a Heise Bourdon tube pressure gauge (CMM, Ashcroft, Inc, USA) with a maximum error of ± 0.02 MPa. To flush out the residual air in the equilibrium cell, the CH_4 gas was purged three times before each run of the experiment. CH_4 gas was then injected into the equilibrium cell until it reached the desired pressure. The experiment was conducted using an isochoric method with step heating and cooling. The equilibrium cell was cooled at 1.0 K/h to induce hydrate nucleation. Sufficient time was given after the abrupt pressure drop, due to hydrate formation, was observed. The temperature was then slowly raised in a stepwise manner at 0.1 K/90 min for CH_4 hydrate dissociation. The three-phase (H–L_w–V) equilibrium point was determined by the intersection between the dissociation line of CH_4 + inhibitor hydrates and the thermal expansion line. The equilibrium temperature difference between CH_4 hydrate and CH_4 + inhibitor hydrate at 8.0 MPa was obtained by interpolation from corresponding H–L_w–V equilibrium curves.

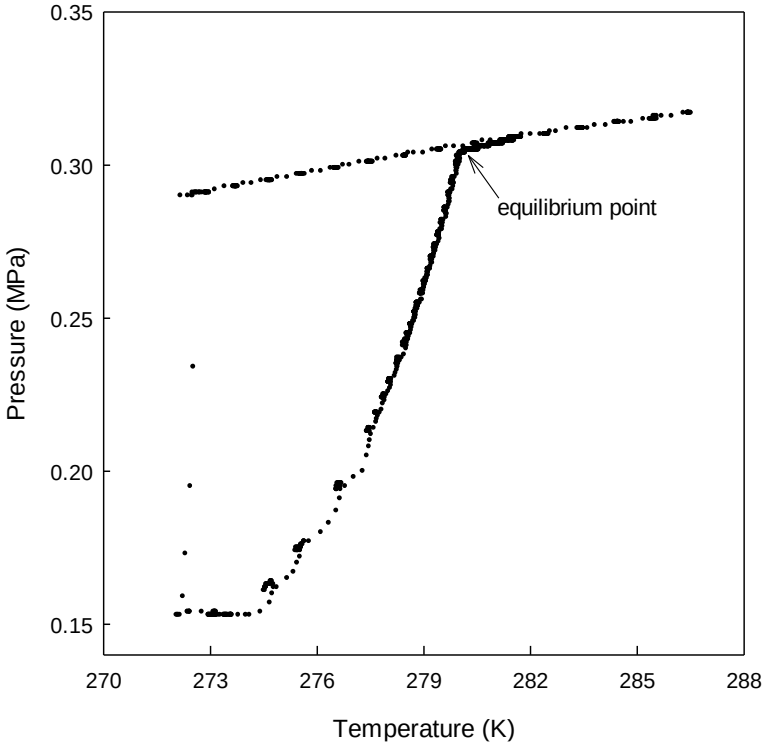

Figure 2.2.2. Determination of equilibrium point of CH_4 hydrate.

2.2.2 Kinetic method

A high-pressure micro-differential scanning calorimeter (HP μ-DSC VII evo, Setaram Inc., France) was used to measure the onset temperature of CH_4 hydrate for the performance evaluation of inhibitors. The HP μ-DSC consisted of a reference cell and a sample cell, which were designed to operate at up to 40 MPa and at a temperature range from 228.15 K to 393.15 K. A customized "sample holder" with four depressions and a support rod was fabricated for more accurate detection of CH_4 hydrate formation. After each depression was filled with 1 mg of solution using a micro-syringe, the sample holder was placed in the sample cell and the sample cell was pressurized to 10 MPa. The temperature was lowered from 273.15 K to 256.15 K at a rate of 0.2 K/min for CH_4 hydrate formation. The temperature at the point at which the exothermic peak appeared was determined to be the onset temperature of CH_4 hydrate in the HP μ-DSC method. For each inhibitor solution, experimental runs were repeated at least five times, and the obtained onset temperatures were averaged.

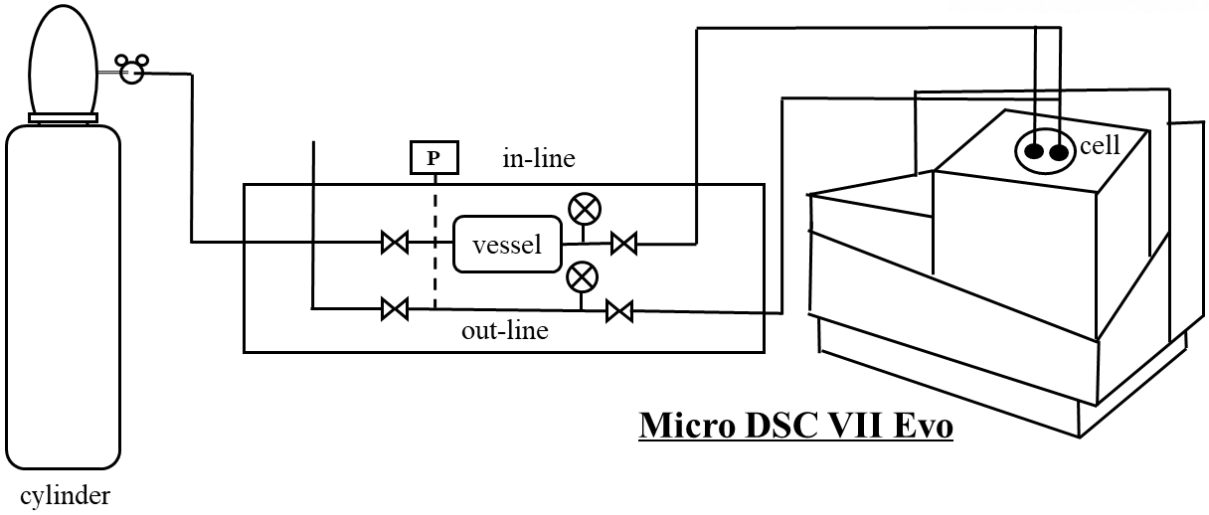

Figure 2.2.3. High-pressure micro-differential scanning calorimeter.

A specially designed equilibrium cell, which was made of 316 stainless steel with an internal volume of approximately 70 cm^3, was used to measure the onset temperature of CH_4 hydrate in the presence of inhibitors. The equilibrium cell was charged with 30 cm^3 of solution with or without inhibitors. The solution in the cell was vigorously agitated by an impeller-type stirrer. The cell temperature was measured using a resistance temperature detector (RTD), which was calibrated from 268.15 to 305.15 K using an ASTM 63C (H-B Instrument Company, USA) with an accuracy of ± 0.02 K. The cell pressure was measured using a pressure transducer (S-10, WIKA, Germany) and calibrated using a Heise Bourdon tube pressure gauge (CMM, Ashcroft, Inc, USA) within a maximum error of ± 0.02 MPa. After being purged three times with CH_4 gas, the cell was pressured to 10 MPa at 285.8 K. After sufficient stabilization at 10 MPa at 285.8 K, the cell was cooled down from 285.8 K to 272.7 K at 0.02 K/min. CH_4 hydrate nucleation and subsequent formation was detected by an abrupt pressure drop during the cooling process. The temperature at the point at which the abrupt pressure drop occurred was determined to be the onset temperature of CH_4 hydrate in the high-pressure autoclave method. For each inhibitor solution, the average onset temperatures were obtained after at least seven experimental runs. The pressure drop (ΔP) was determined from the pressure difference between the start point and the end point of hydrate formation.

Gas uptake during hydrate formation was measured at 8.0 MPa and sub-cooling temperature (ΔT) of 4 K. The pressure during the experiment was kept constant using the constant pressure mode of a micro-flow syringe pump (500D, Teledyne ISCO, USA). The consumed volume of CH_4 gas during gas hydrate formation was recorded at intervals of 10 min. The ratio of moles of consumed gas to moles of initially

charged water (nCH_4/nH_2O) was calculated from volume change data. The percent conversion of water into hydrates (C_{WH}) was calculated using equation (1).

$$C_{WH} = (nCH_4/nH_2O) \times N_{hyd} \times 100\% \quad (1)$$

Where N_{hyd} is the hydration number, which is known to be 6.0 for CH_4 hydrate.

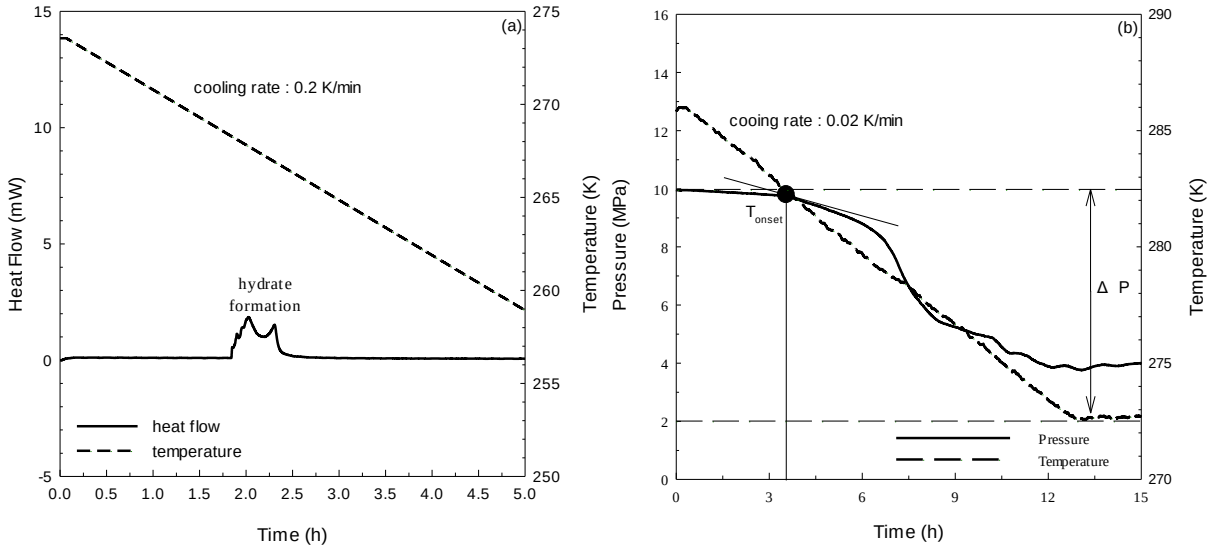

Figure 2.2.4. Determination of the onset temperature for CH_4 hydrate in the temperature-ramping method: (a) HP μ-DSC; (b) high-pressure autoclave.

2.2.3 Microscopic method

For PXRD measurements, the gas hydrate samples were formed at hydrate-stable conditions and then finely powdered with a 50 μm sieve in a liquid N_2 vessel. The PXRD patterns were obtained by the PLS-II 6D C&S UNIST-PAL beamline of the Pohang Accelerator Laboratory (Republic of Korea). The energy of the synchrotron beamline was 12.658 keV (λ = 0.9795 Å). All 2θ angles were scanned with an exposure time of 60 s at 127 K. The two-dimensional patterns obtained (Q-spacing, nm-1) were converted into one-dimensional diffraction patterns for comparison with the conventional PXRD patterns. The acquired patterns were analyzed with Rietveld refinement using the Fullprof program.

An in-situ fiber-coupled Raman spectrometer (SP550, Horiba, France), equipped with a multichannel air-cooled CCD detector and a 1,800 groove/mm grating, was used to monitor CH_4 hydrate formation

behavior and enclathration of CH_4 gas in the hydrate cages at 8.0 MPa and $\Delta T = 4$ K. Time-dependent Raman spectra were collected using a fiber-optic Raman probe that was attached to the water-jacketed reactor.

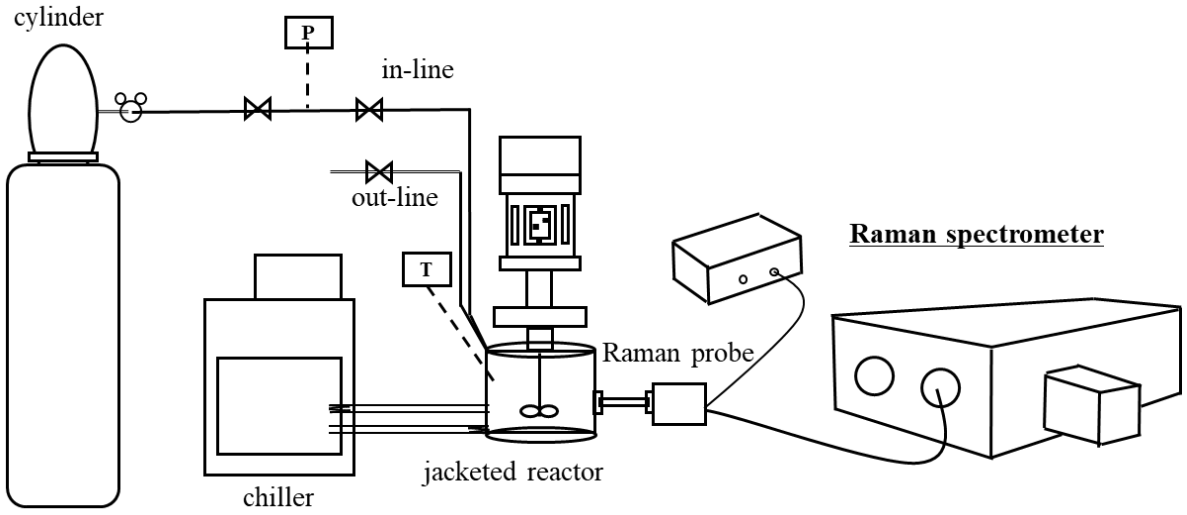

Figure 2.2.5. Schematic diagram of an experimental setup for in situ Raman measurement.

2.2.4 Computational method

COSMO-RS software (Software for Chemistry & Materials B.V., the Netherlands) was used to provide the σ profiles of amino acids and ionic liquids. All studied molecules were taken from ADFinput software for geometry optimization and saved in the COSMO-RS database. The σ profile is the 3D screening charge distribution, which represents the specific charge density of a molecular surface, and can be divided into polar regions (hydrogen bond (H-bond) acceptor and donor) and nonpolar regions.

Density functional theory (DFT) is a powerful tool for estimating host-guest interaction, intermolecular interaction, and interaction energy between gas hydrates and inhibitors. In this study, the Gaussian 09 program (B3LYP/6-311G**) was used to calculate interaction energy between a hydrate cage and an inhibitor molecule and the self-consistent field (SCF) convergence criteria was set to be 1.0×10^{-6} hartrees. From the DFT calculation using the Gaussian 09 program, the optimized energies of a small (5^{12}) cage (E_{cage}), an inhibitor ($E_{inhibitor}$), and the overall configuration of the hydrate cage and inhibitor ($E_{overall}$) were obtained. The interaction energy ($E_{interaction}$) was calculated using the following equation:

$$E_{interaction} = E_{overall} - (E_{cage} + E_{inhibitor}) \qquad (2)$$

QTAIM method was used to validate and support experimental results about the inhibition performance of inhibitors on CH_4 hydrates. To investigate how each substance molecule affected the formation of CH_4 hydrate structure, hydrate cages of sI were built based on Bernal–Fowler rules. One sI small cage (5^{12}) and one sI large cage ($5^{12}6^2$) were glued and stabilized in a Merck Molecular Force Field (MMFF94). In addition, complete geometry optimization of hydrate cages was done using the semi-empirical parametric method 6 (PM6) available in Gaussian09W software. To identify the thermodynamic inhibition effects of ChCl, urea, and DES on CH_4 hydrate, optimization of inhibitor molecules and built sI hydrate cages was conducted at the same time. ChCl, urea, and DES all formed hydrogen bonds automatically with water molecules of the hydrate cages upon the given calculation level. Then, the QTAIM method was applied using the Multiwfn software to find BCPs between attached inhibitor molecules and CH_4 hydrate cages. Among the four types of BCPs, the (3, -1) type is highly related to the hydrogen bonds. Therefore, (3, -1) BCPs' physical properties were investigated to calculate the hydrogen bond strength between inhibitor molecules and hydrate cages. To derive the hydrogen bond energy between attached inhibitor molecules and water molecules in the hydrate cages, the following equation suggested by Espinosa et al. was used, where all parameters can be yielded from the topological information of (3, -1) BCPs.

$$E_{HB} = \frac{V(r)}{2} \quad (1)$$

V(r) denotes potential energy density and E_{HB} denotes hydrogen bond energy. Furthermore, previous studies demonstrated that charge densities have a linear relationship with intermolecular energy values:

$$E_{HB} = A\rho + B \quad (2)$$

Here, ρ denotes calculated electron charge density at (3, -1) BCPs, and A and B are linearly fitted parameters that are obtained by the linear regression of E_{HB} and ρ.

Chapter 3. Investigations into Amino Acid and Ionic Liquid Mixture as Gas Hydrate Inhibitors

3.1. Experimental and Computational Investigation of Methane Hydrate Inhibition in the Presence of Amino Acids and Ionic Liquids

This chapter includes the published contents:

Lee D, Go W, Seo Y. Experimental and computational investigation of methane hydrate inhibition in the presence of amino acids and ionic liquids. Energy 2019;182:632-40. Reproduced with permission.

3.1.1. Abstract

Amino acids (glycine and alanine) and ionic liquids ([BMIM][BF_4] and [BMIM][I]) were examined for their inhibition effects on CH_4 hydrates with experimental and computational approaches. Both amino acids and ionic liquids functioned well as thermodynamic hydrate inhibitors, by shifting equilibrium curves of CH_4 hydrates toward harsh conditions. However, powder X-ray diffraction patterns indicated that amino acids and ionic liquids did not affect the hydrate structure because they were not included in the hydrate cages due to their large molecular size. Gas uptake measurements showed that the conversion of water into gas hydrates and the formation rates of CH_4 hydrate were significantly influenced by inhibitors. Density functional theory calculations indicated that [BMIM][BF_4] had a larger potential than glycine to inhibit gas hydrate formation by giving a more negative interaction energy between a cage and an inhibitor molecule. The time-dependent Raman spectra collected during CH_4 hydrate formation demonstrated that [BMIM][BF_4] hindered CH_4 molecules from occupying small (5^{12}) cages, whereas glycine had a strong influence on large ($5^{12}6^2$) cages of sI hydrates. The experimental and computational results provide a better understanding of inhibition mechanisms of gas hydrates and thus can contribute to the improved control of hydrate formation in oil and gas pipelines.

3.1.2. Influence of inhibitors on thermodynamic stability

The three-phase equilibria (hydrate (H) – liquid water (L_w) – vapor (V)) of CH_4 hydrate in the presence of various inhibitors were measured to observe and compare the performance of the inhibitors. The thermodynamic inhibition effects of various substances (3.0 mol %), including methanol, glycine, alanine, [BMIM][BF_4], and [BMIM][I], are presented in Figure 3.1.1. and Table 3.1.1. As expected, the hydrate equilibrium curves of inhibitor-added systems were shifted to higher-pressure and lower-temperature regions.

Salts and alcohols are the most common THIs; ions disrupt the hydrogen bonds of host water frameworks, and alcohols have the potential to form hydrogen bonds with host water molecules, leading to the weakening of thermodynamic stability of hydrate lattices. Inhibitor molecules generally consist of polar functional groups that contain highly electronegative atoms such as F, O, and N [1, 21, 24]. These functional groups attract the hydrogen atoms of water molecules in the host frameworks of the hydrate structure, which ultimately result in the shift of H–L_w–V equilibrium curves to harsh conditions. In this manner, ionic liquids ([BMIM][BF_4] and [BMIM][I]) and amino acids (glycine and alanine) displayed significant thermodynamic inhibition effects on CH_4 hydrate, as shown in Figure 3.1.1.

The equilibrium temperature differences between pure CH_4 hydrate and CH_4 + THI hydrates at 8.0 MPa are depicted in Figure 3.1.2. The equilibrium temperature differences of ionic liquids and amino acids were generally comparable to, or slightly smaller than, those of methanol. Notably, the inhibition effect of glycine was almost the same as that of methanol.

Amino acids (glycine and alanine) showed slightly better thermodynamic inhibition than ionic liquids ([BMIM][BF_4] and [BMIM][I]). This was attributable to different inhibition mechanism in the presence of amino acids and ionic liquids. The amino acids, such as glycine and alanine were reported that they could retard hydrate nucleation and growth because the balance between the hydrophilic functional groups and hydrophobic side chains of amino acids causes perturbation of the local water structure [33-35]. On the other than, ionic liquids are readily ionized as soon as they dissolve in water. The anions (BF_4^- or I^-) of ionic liquids are small enough to move freely around the solution and can thus reduce the probability of hydrate formation and growth effectively [36-38]. Though previous studies have suggested that hydrate inhibition is closely related to the interaction between host water and inhibitor molecules, the precise inhibition mechanism of gas hydrates in the presence of various inhibitors is still unclear.

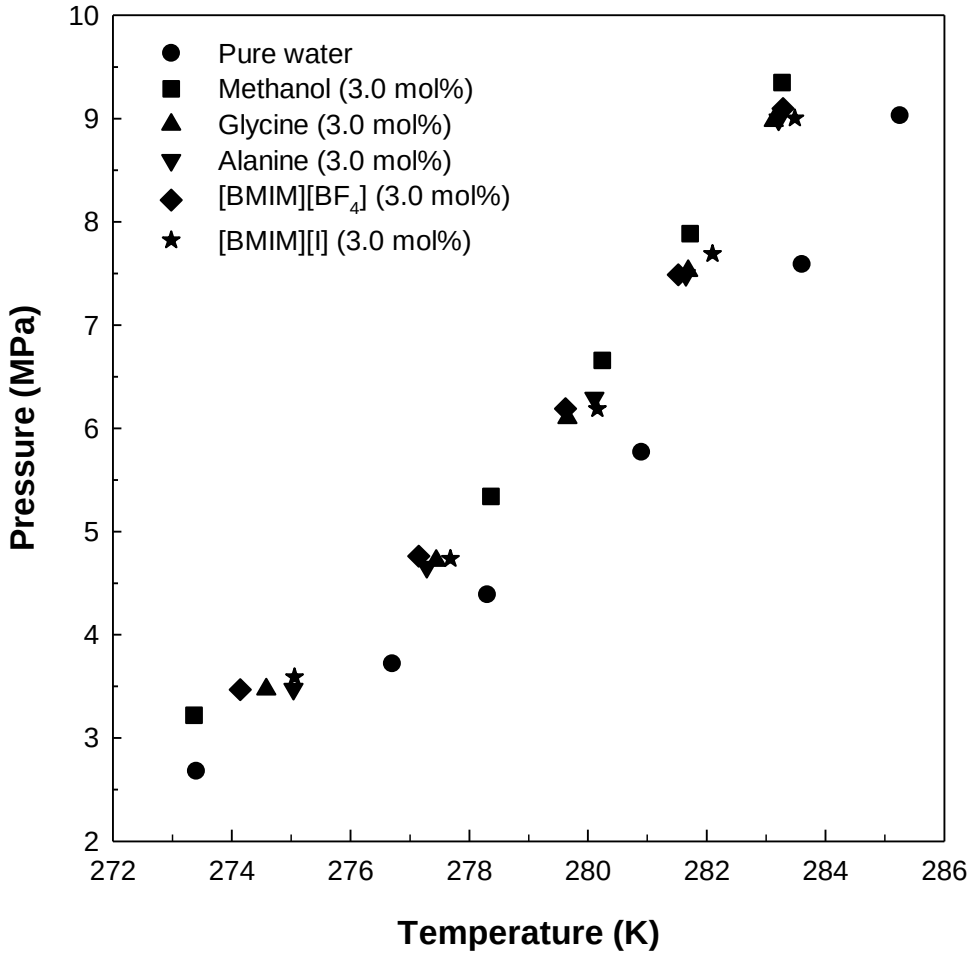

Figure 3.1.1. Phase equilibria of CH_4 hydrate in the presence of inhibitors [78].

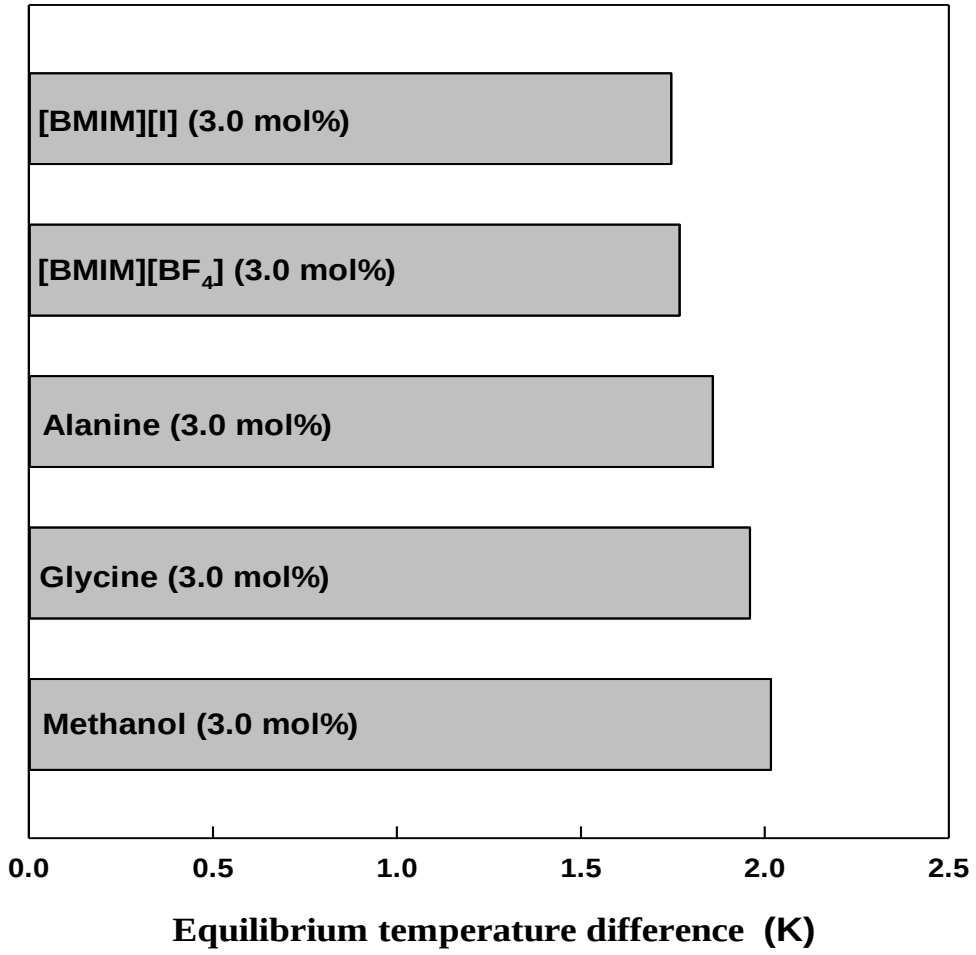

Figure 3.1.2. Equilibrium temperature differences between CH_4 hydrate and CH_4 + inhibitor hydrates at 8.0 MPa [78].

Table 3.1.1. Hydrate phase equilibrium data of the CH_4 + inhibitor (3.0 mol%) + water systems.[a]

Methanol		**Glycine**		**Alanine**		**[BMIM][BF$_4$]**		**[BMIM][I]**	
T (K)	P (MPa)	T (K)	P (MPa)	T (K)	P (MPa)	T (K)	P (MPa)	T (K)	P (MPa)
273.4	3.22	274.6	3.47	275.0	3.47	274.1	3.47	275.1	3.59
278.4	5.34	277.4	4.72	277.3	4.66	277.2	4.76	277.7	4.74
280.2	6.66	279.7	6.10	280.1	6.30	279.6	6.19	280.2	6.19
281.7	7.89	281.7	7.53	281.7	7.48	281.5	7.49	282.1	7.69
283.3	9.35	283.1	8.98	283.2	8.99	283.3	9.10	283.5	9.00

[a] Standard uncertainties u are u(T) = 0.1 K and u(P) = 0.02 MPa.

3.1.3. Structural analysis through PXRD

Structure identification is the first step in clarifying the influence of inhibitors on the CH4 hydrate. PXRD was used to identify the hydrate structure in the presence of inhibitors (3.0 mol%). The PXRD patterns presented in Figure 3.1.3. demonstrate that all the peak positions of CH_4 + inhibitor hydrates overlapped with those of the pure CH_4 hydrate. Pure CH_4 hydrate is cubic sI (space group Pm3n) and its lattice parameter is a = 11.87 Å. The structure of CH_4 + inhibitor hydrates were also identified as cubic sI (space group Pm3n) and their lattice parameters were consistent with those of the pure CH_4 hydrate (Table 2). This implies that the amino acids and ionic liquids had no influence on the hydrate crystal structure. PXRD results indicated that ionic liquids and amino acids were not incorporated in the hydrate cages because they are too large to fit into the cages of sI hydrate. Ionic liquids and amino acids resided on the outside of the cages disrupting the hydrogen-bonded water molecular network.

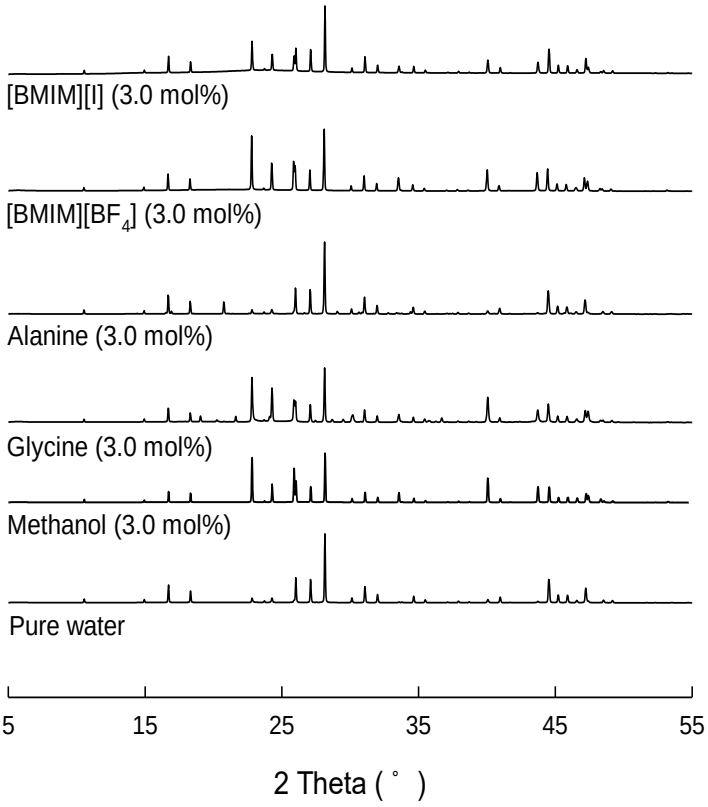

Figure 3.1.3. PXRD patterns of CH_4 hydrates in the presence of inhibitors (3.0 mol%).

Table 3.1.2. Structure and lattice parameters of CH_4 hydrates in the presence of inhibitors.

	Concentration (mol %)	Structure type	Lattice parameter (Å)	R_{wp} (%)
Pure water	-	Structure I	11.8505 ± 0.0002	6.6
Methanol	3.0	Structure I	11.8490 ± 0.0005	6.2
Glycine	3.0	Structure I	11.8645 ± 0.0003	15.5
Alanine	3.0	Structure I	11.8643 ± 0.0004	20.7
[BMIM][BF_4]	3.0	Structure I	11.8715 ± 0.0002	7.8
[BMIM][I]	3.0	Structure I	11.8526 ± 0.0002	5.8

3.1.4. Gas uptakes

Gas uptake measurements were conducted to examine the hydrate growth behavior and to measure the hydrate formation rate in the presence of inhibitors. The amount of gas consumed during the hydrate formation is equal to the total amount of gas trapped in the cages of gas hydrates. Therefore, the ratio of the moles of consumed gas (nCH_4) to moles of initially charged water (nH_2O) was used to express the gas uptake. The amount of CH_4 dissolved in water was neglected due to the extremely low solubility of CH_4 in water compared to the amount of CH_4 enclathrated in the hydrate cages.

Figure 4 shows the gas uptake curves and C_{WH} in the presence of inhibitors for 340 min. As shown in Figure 3.1.4 (a), the gas uptake (nCH_4/nH_2O) of pure CH_4 hydrate increased rapidly after nucleation and reached 0.14 after approximately 110 min. The final nCH_4/nH_2O value of pure CH_4 hydrate was slightly lower than the theoretical value (0.17), mainly due to occluded water in the formed gas hydrate crystals for the bulk water system.

The gas uptakes of CH_4 + inhibitor (3.0 mol%) hydrates were significantly lower than that of pure CH_4 hydrate. The addition of inhibitors also had an influence on the growth behavior of CH_4 hydrate. [BMIM][BF_4] consistently reduced the growth rate of CH_4 hydrate for about 250 min, whereas glycine did not retard the hydrate growth at the initial stage of hydrate formation. However, the final nCH_4/nH_2O value of the CH_4 + glycine (3.0 mol%) hydrate was almost the same as that of the CH_4 + [BMIM][BF_4] (3.0 mol%) hydrate. As seen in Figure 3.1.4 (b), the conversion of water into gas hydrate (C_{WH}) for pure water was 87.6%, whereas C_{WH} for the glycine (3.0 mol%) and [BMIM][BF_4] (3.0 mol%) solutions was 60.1% and 62.6%, respectively. This again indicates that [BMIM][BF_4] and glycine can affect the conversion of water into gas hydrate, as well as the hydrate growth behavior.

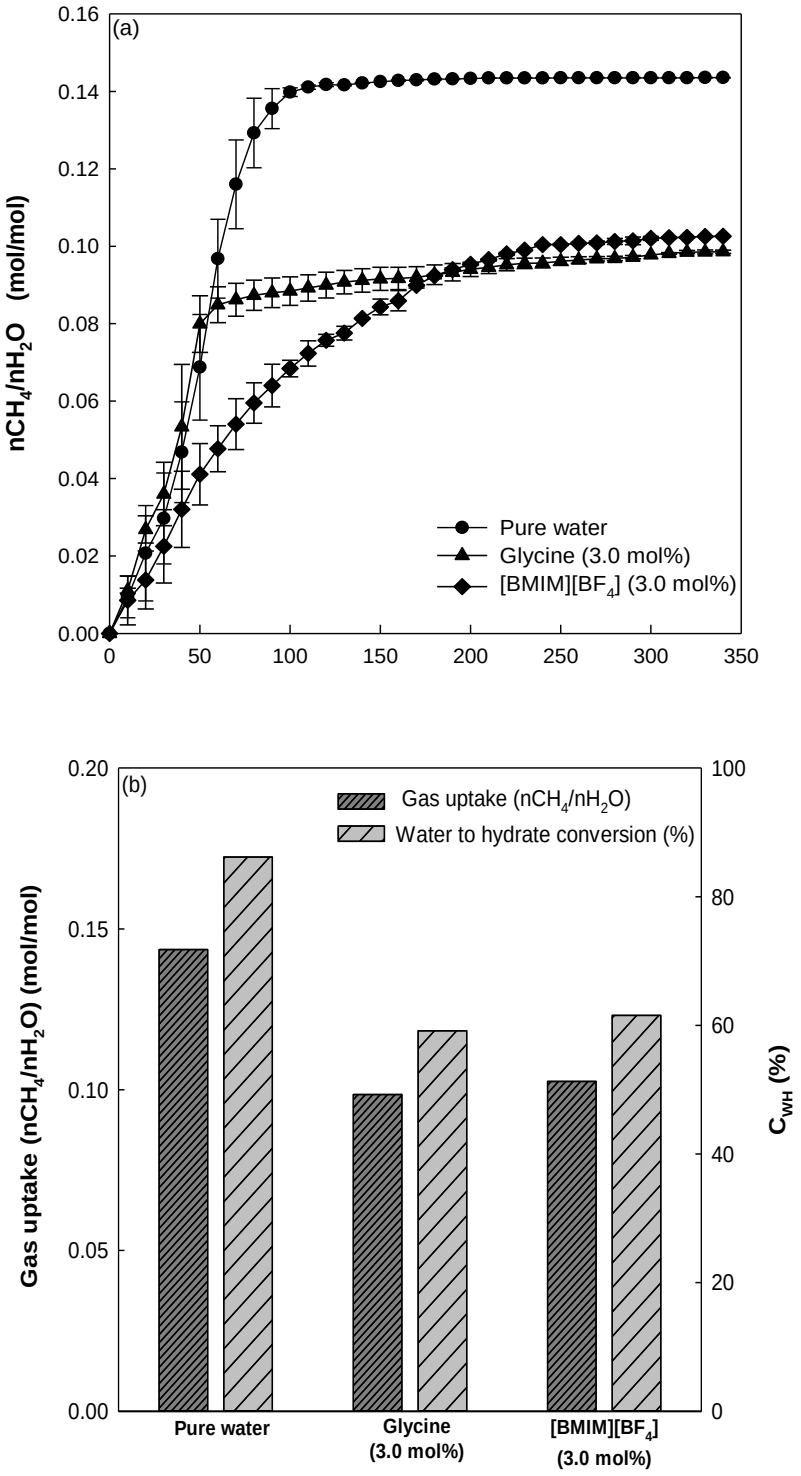

Figure 3.1.4. (a) Gas uptakes during hydrate formation in the presence of inhibitors. (b) Comparison of gas uptakes and percent conversion of water into hydrates for pure CH_4, CH_4 + glycine, and CH_4 + [BMIM][BF_4] hydrates.

3.1.5. Computational methods

In this study, DFT was applied to calculate the interaction energy between a hydrate cage and an inhibitor molecule. DFT is a useful tool for quantifying molecular interaction and evaluating the performance of hydrate inhibitors. Negative interaction energy between a host water molecule and an inhibitor molecule indicates attractive interaction, whereas positive interaction energy means repulsive interaction [39, 40]. The structure configurations of a cage with an inhibitor molecule (glycine and [BMIM][BF_4]), optimized for DFT calculations, are presented in Figure 5, and the calculated interaction energies are listed in Table 3.1.3.

The interaction energies between a cage and an inhibitor molecule were found to be -94.13 kcal/mol for [BMIM][BF_4] and -12.55 kcal/mol for glycine. Anderson et al. found, through molecular dynamic simulations, that the effectiveness of the inhibitors is closely related to the free energy of binding between the inhibitor molecules and the hydrate surface, and thus the stronger inhibitors have more negative binding energies [41]. In this study, the interaction energies between the inhibitor molecule and the hydrate cage were found to be negative for both [BMIM][BF_4] and glycine. [BMIM][BF_4] has more negative interaction energy than glycine and, thus, stronger attraction existed between [BMIM][BF_4] and the hydrate cage, which led to the slower formation rate of CH_4 hydrate in the presence of [BMIM][BF_4]. The results from gas uptake and DFT calculations imply that [BMIM][BF_4] can function better as an inhibitor during CH_4 hydrate formation and that inconsistent hydrate growth behaviors in the presence of inhibitors may be caused by different inhibition mechanisms of the inhibitors used. The cage-specific inhibition effect of ionic liquids and amino acids can affect gas uptakes, hydrate conversion, and formation behaviors of CH_4 + inhibitor hydrates and thus, the direct evidence for different inhibition mechanisms of the inhibitors should be examined by observing growth behaviors of each cage in CH_4 + inhibitor hydrates via in-situ Raman spectroscopy.

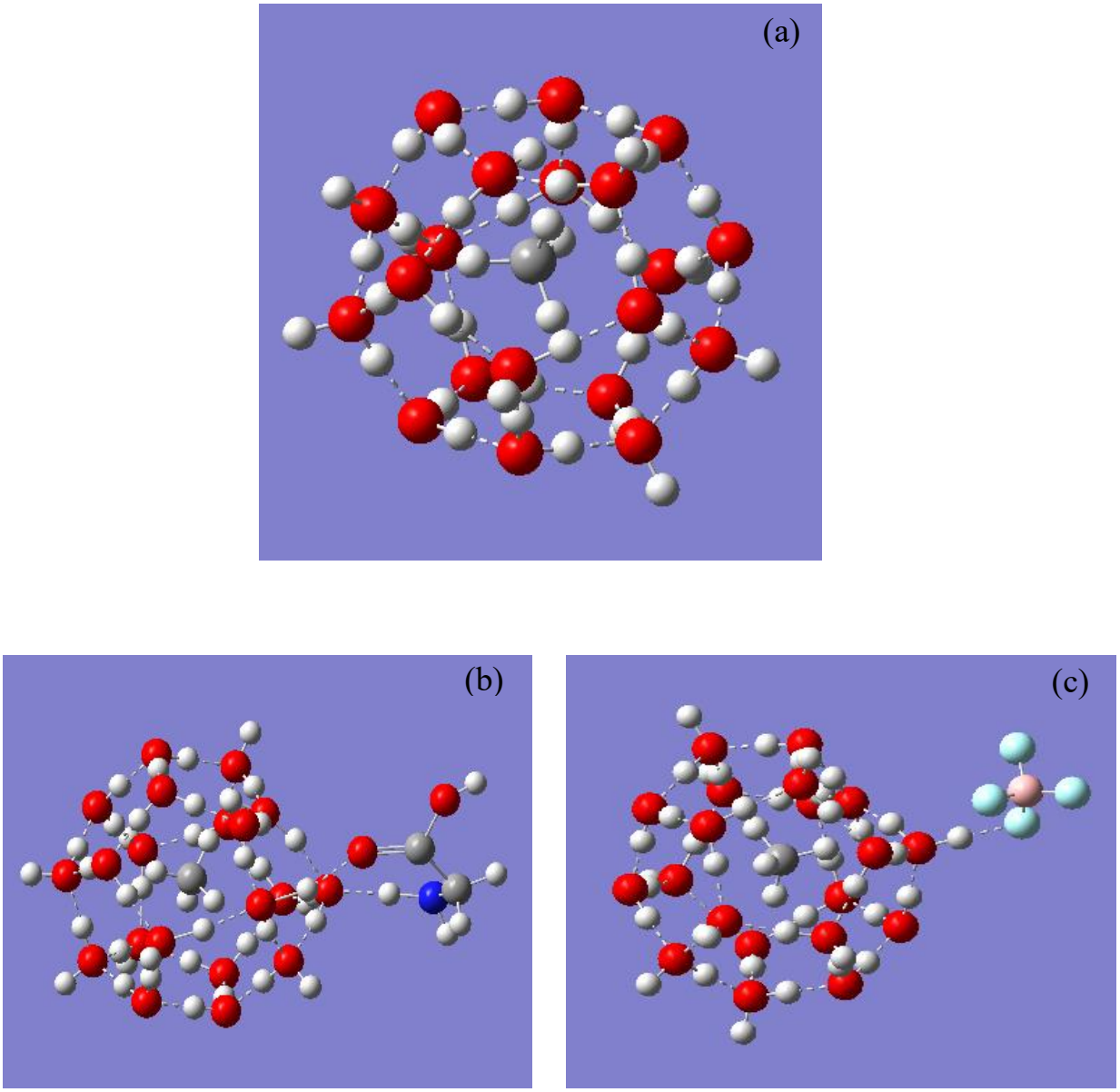

Figure 3.1.5. Structure configuration of (a) small (5^{12}) cage, (b) small (5^{12}) cage with a glycine molecule, and (c) small (5^{12}) cage with [BF_4^-]. The dashed line indicates a hydrogen bonding.

Table 3.1.3. Calculated interaction energy between a small (5^{12}) cage and an inhibitor using density functional theory (B3LYP/6-311G**).

Case	Cage + Inhibitors ($E_{overall}$) (Hartree)	Cage only (E_{cage}) (Hartree)	Inhibitors ($E_{inhibitors}$) (Hartree)	Interaction Energy ($E_{interaction}$) (Kcal/mol)
5^{12} cage only	-1568.30	-1568.30	0	0
5^{12} cage + glycine	-1852.68	-1568.30	-284.36	-12.55
5^{12} cage + [BMIM][BF_4]	-1992.79	-1568.30	-424.34	-94.13

3.1.6. In-situ Raman spectroscopy

In-situ Raman spectroscopy is very useful in observing the enclathration of gas molecules in the gas hydrate cages and confirming the hydrate structure. Figure 3.1.6. shows time-dependent Raman spectra of pure CH_4, CH_4 + glycine (3.0 mol%), and CH_4 + [BMIM][BF_4] (3.0 mol%) hydrates after hydrate nucleation. The pure CH_4 hydrate exhibited two Raman peaks at 2905 and 2915 cm^{-1}, which were assigned to CH_4 molecules captured in the large ($5^{12}6^2$) and small (5^{12}) cages of sI hydrate, respectively. The two Raman peaks at 2905 and 2915 cm^{-1} were also observed when glycine and [BMIM][BF_4] were added, which also supports the PXRD result that neither glycine nor [BMIM][BF_4] affected the hydrate structure.

In addition, in-situ Raman spectroscopic results can provide further insights into inhibition mechanisms by offering information about cage-dependent guest distributions and occupation during hydrate formation. The time-dependent Raman spectra of pure CH_4 hydrate are presented in Figure 3.1.6 (a). The Raman peaks corresponding to both small (5^{12}) and large ($5^{12}6^2$) cages of pure CH_4 hydrate began to grow simultaneously after hydrate nucleation. The intensities of the small and large cages of pure CH_4 hydrate increased steadily over time, and became almost constant after approximately 110 min. However, CH_4 + inhibitor hydrates demonstrated significantly different cage-filling behaviors during hydrate formation, as seen in Figures 3.1.6 (b) and (c). The overall growth patterns of small (5^{12}) and large ($5^{12}6^2$) cages in the CH_4 + glycine (3.0 mol%) hydrate seemed to be similar to those of pure CH_4 hydrate, but the intensity of large ($5^{12}6^2$) cages in the CH_4 + glycine (3.0 mol%) hydrate was somewhat lower than that in pure CH_4 hydrate and, therefore, the intensity ratio of large ($5^{12}6^2$) to small (5^{12}) cages in the CH_4 + glycine (3.0 mol%) hydrate was lower than that in pure CH_4 hydrate throughout hydrate formation. This was attributed to the fact that glycine molecules inhibited primarily the large ($5^{12}6^2$) cages and, hence, the encapsulation of CH_4 molecules in the large ($5^{12}6^2$) cages was hampered during the hydrate growth stage. As seen in Figure 3.1.6 (c), the growth patterns of the CH_4 + [BMIM][BF_4] (3.0 mol%) hydrate were quite different from those of pure CH_4 and CH_4 + glycine (3.0 mol%) hydrates. For the CH_4 + [BMIM][BF_4] (3.0 mol%) hydrate, the Raman peak corresponding to CH_4 molecules captured in the large ($5^{12}6^2$) cages grew fast at the early stage of hydrate formation, and then continued to grow slowly over time, whereas the intensity of the Raman peak for the small (5^{12}) cages was almost constant for 200 min. This indicates that [BMIM][BF_4] has a specific influence on the small (5^{12}) cages, hindering CH_4 molecules from occupying the small (5^{12}) cages.

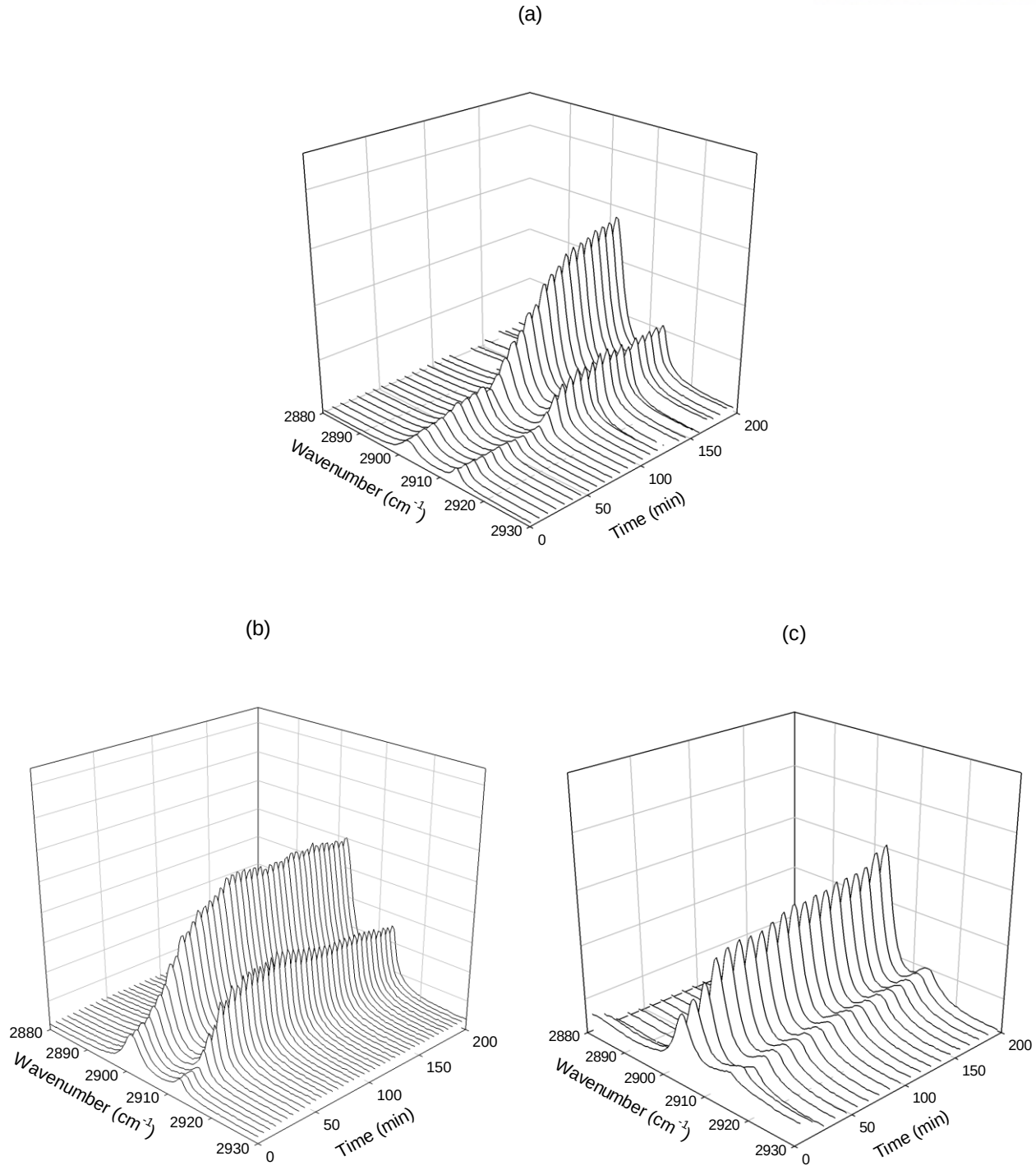

Figure 3.1.6. In-situ Raman spectra of (a) pure CH_4 hydrate, (b) CH_4 + glycine (3.0 mol%) hydrate, and (c) CH_4 + [BMIM][BF_4] (3.0 mol%) hydrate.

Fractional cage occupancy (θ) of CH_4 in both small (5^{12}) and large ($5^{12}6^2$) cages of sI hydrate at a given time during hydrate formation was obtained to fully understand cage-specific guest occupation and the precise roles of each inhibitor during hydrate formation. The thermodynamic expression, which indicates the chemical potential of water in sI hydrate, should be combined with the relative integrated areas of the Raman spectra to determine cage occupancy of CH_4 [42].

$$\mu_\omega(h) - \mu_\omega(h^\circ) = \frac{RT}{23}[3\ln(1-\theta_L) + \ln(1-\theta_S)] \qquad (3)$$

Here, $\mu_\omega(h^\circ)$ is the chemical potential of water molecules of a hypothetical empty lattice, and θ_L and θ_S are the fractional occupancies of CH_4 molecules in the large ($5^{12}6^2$) and small (5^{12}) cages of sI hydrate, respectively. When the gas hydrate is in an equilibrium with ice, the left side of eq. (3) becomes $-\Delta\mu_\omega(h^\circ)$. $\Delta\mu_\omega(h^\circ)$, which is known to be 1,297 J/mol for sI hydrate. In addition, the ratio (A_L/A_S) of area of CH_4 molecules trapped in the large ($5^{12}6^2$) cages to that of the small (5^{12}) cages, and the resulting cage occupancy ratio (θ_L/θ_S), were calculated from each time-dependent Raman spectrum in Figure 3.1.6. The changes in both A_L/A_S and θ_L/θ_S during hydrate formation for pure CH_4, CH_4 + glycine (3.0 mol%), and CH_4 + [BMIM][BF_4] (3.0 mol%) hydrates are depicted in Figure 3.1.7.

For pure CH_4 hydrate, the A_L/A_S value increased gradually until 110 min and finally reached 3.3, which is slightly higher than the theoretical value (3.0). The small (5^{12}) cages were slightly more populated at the initial stage, but as hydrate formation proceeded, the θ_L value became slightly higher than the θ_S value (Figure 3.1.7 (a)). However, for the CH_4 + glycine (3.0 mol%) hydrate, the A_L/A_S value was lower than that for pure CH_4 hydrate for the entire hydrate formation period (Figure 3.1.7 (b)), which confirms that glycine has a strong inhibition effect on the large ($5^{12}6^2$) cages.

Due to the cage-specific inhibition of glycine, the θ_L value (~ 0.8) was much lower at the initial stage of hydrate formation, gradually increased after 60 min, and finally reached 0.94, while the θ_S value was almost constant (0.99) throughout the hydrate formation. As expected from Figure 3.1.6 (c), [BMIM][BF_4] specifically affected small (5^{12}) cages of CH_4 hydrate, not only at the initial stage, but also at the final stage of hydrate formation (Figure 3.1.7 (c)). The θ_S value of the CH_4 + [BMIM][BF_4] (3.0 mol%) hydrate was found to be 0.66 at the initial stage and 0.54 at the final stage, which was much lower than those for pure CH_4 and CH_4 + glycine (3.0 mol%) hydrates. Furthermore, the final A_S/A_L value of CH_4 + [BMIM][BF_4] hydrate was 5.4, which was much higher than those for pure CH_4 hydrate (3.3) and CH_4 + glycine hydrate (2.9). Figure 3.1.7 (c) clearly indicates that [BMIM][BF_4] was very effective in inhibiting CH_4 molecules from occupying the small (5^{12}) cages, leaving a large fraction of small (5^{12}) cages vacant during hydrate formation.

Gas uptakes, hydrate conversion, and formation behaviors of CH_4 + inhibitor hydrates were

significantly dependent on the types of inhibitors used, because in the presence of inhibitors, cage-specific guest occupation occurred during CH_4 hydrate formation. Further studies about possible synergism that might occur when two inhibitors with different inhibition mechanisms are mixed together should therefore be conducted for a complete understanding of host-inhibitor interaction and cage-specific inhibition mechanisms.

(a)

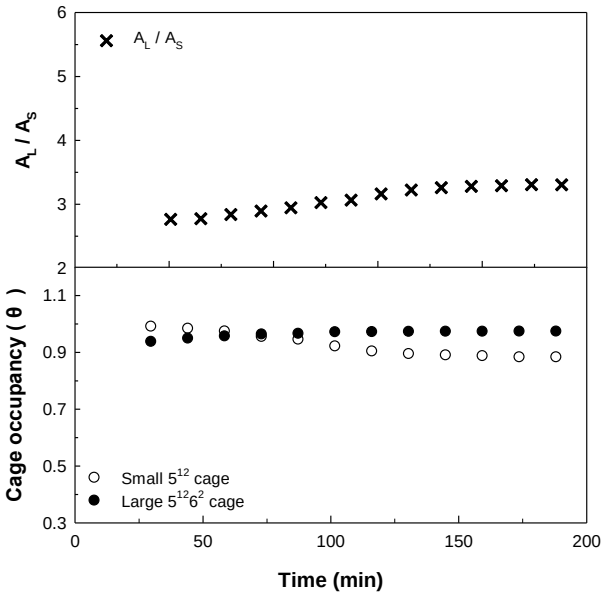

(b)

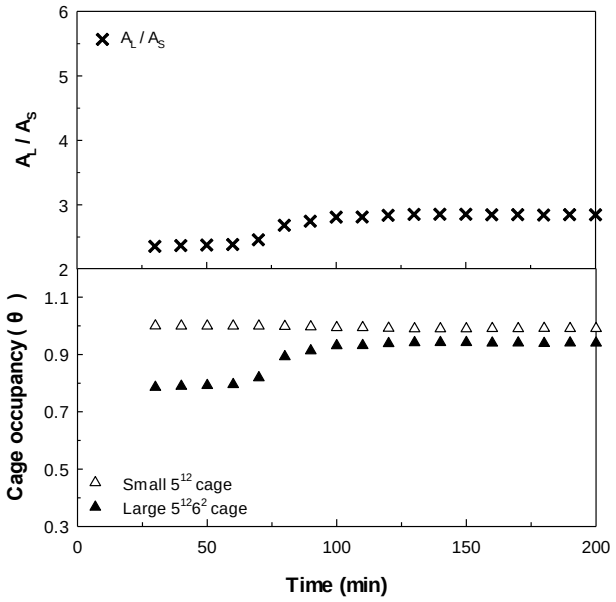

(c)

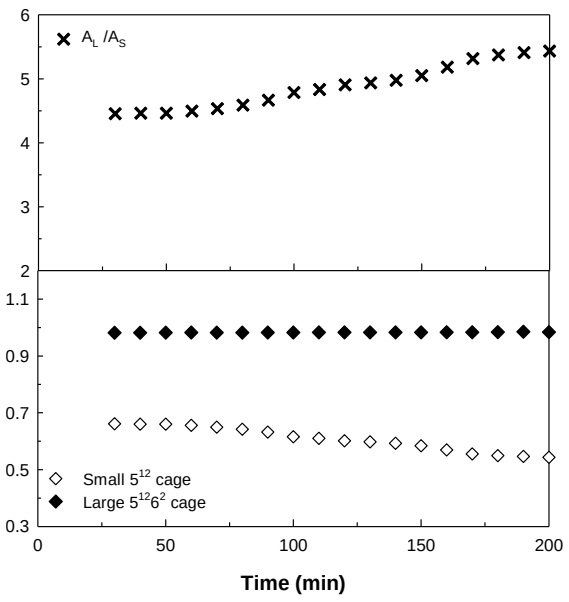

Figure 3.1.7 Changes in A_L/A_S and cage occupancy (θ_L and θ_S) at a given time during hydrate formation of (a) Pure water, (b) Glycine (3.0 mol%), and (c) [BMIM][BF_4] (3.0 mol%) solutions.

3.1.7. Conclusions

In this study, the thermodynamic and kinetic characteristics of CH_4 hydrate in the presence of amino acids and ionic liquids were examined with both experimental and computational approaches to determine the inhibition mechanism of gas hydrates**.** Through the experimental results, both ionic liquids ([BMIM][BF_4] and [BMIM][I]) and amino acids (glycine and alanine) showed significant thermodynamic inhibition effects on CH_4 hydrate. It was found from PXRD results that the addition of inhibitors had no effect on the crystal structure of CH_4 hydrate. However, gas uptakes, hydrate conversion, and formation behaviors of CH_4 + inhibitor hydrates were significantly dependent on the types of inhibitors used. The gas uptakes (nCH_4/nH_2O) and C_{WH} of CH_4 + inhibitor (3.0 mol%) hydrates were significantly lower than those of pure CH_4 hydrate and, in particular, the growth rate of CH_4 + [BMIM][BF_4] (3.0 mol%) hydrate was much lower than those of other hydrates. The DFT calculations showing interaction energy between a cage and an inhibitor molecule indicated that [BMIM][BF_4]-added system had a higher probability of inhibiting hydrate formation because they showed more negative interaction energy (-94.13 kcal/mol) than glycine-added system (-12.55 kcal/mol). Finally, the real-time Raman spectra collected during the formation of CH_4 hydrates offered direct evidence of the cage-specific inhibition mechanisms of glycine and [BMIM][BF_4]. Glycine had a strong influence on the large ($5^{12}6^2$) cages, while [BMIM][BF_4] inhibited CH_4 molecules from being captured in the small (5^{12}) cages. The outcomes and findings of this study obtained through experimental and computational approaches contribute to providing new insights into inhibition mechanisms of gas hydrates in the presence of various inhibitors, and suggest that their different inhibition mechanisms could bring synergy effects when mixed each inhibitor.

3.2. Synergistic Inhibition Effect of Amino Acid and Ionic Liquid Mixture on Methane Hydrate Formation

This chapter includes the published contents:

Lee D, Go W, Ko G, Seo, Y. Inhibition synergism of glycine (an amino acid) and [BMIM][BF_4] (an ionic liquid) on the growth of CH_4 hydrate. *Chem Eng J* 2020;124466. Reproduced with permission.

3.2.1. Abstract

Observed inhibition effects that glycine (amino acid) inhibits the enclathration of CH_4 into the large $5^{12}6^2$ cages and [BMIM][BF_4] (ionic liquid) strongly prevents entering of CH_4 molecules into the small 5^{12} cages are presented in previous paper. In this respect, our study firstly attempted to prove whether the synergy effect is caused by cage-specific inhibition effect of each inhibitor when the two inhibitors were mixed. In order to verify the synergy effect, thermodynamic, microscopic, and kinetic studies were experimented. First, the three-phase equilibria of CH_4 hydrate with inhibitor mixtures indicated that there is no synergistic effect on hydrate phase equilibria. In addition, powder X-ray diffraction (PXRD) represents that there are no structural characteristic differences on various inhibitors on CH_4 hydrate. However, gas uptake results indicate that glycine + [BMIM][BF_4] mixture retard hydrate growth significantly compare to other solutions at $\Delta T = 4$ K. This growth tendency was also observed from in-situ Raman spectroscopy. The nucleation time of small cages is much longer than large cages, and the hydrate growth pattern of both cages totally different to pure CH_4 hydrate. The results of this study will provide a broad understanding of fundamental hydrate inhibition mechanism and improve the synergistic effect concepts of hydrate inhibitors for natural gas production and transportation.

3.2.2. Influence of inhibitors on thermodynamic stability condition

The thermodynamic stability of CH_4 hydrate in the presence of various inhibitors (3.0 mol%) is essential to predict the pressure and temperature conditions for operating conditions in flow assurance. In order to measure the influence of inhibitor mixture on the stability conditions of CH_4 hydrates, three-phase equilibria (hydrate (H) – liquid water (L_w) – vapor (V)) of CH_4 hydrate in the presence of inhibitors were compared with the three-phase (H–L_W–V) equilibria of the pure CH_4 hydrate and the experimental results are presented in Figure 3.2.1. and Table 3.2.1. The hydrate equilibrium lines of inhibitor-added systems appeared at significantly lower-temperature and higher-pressure regions compared to pure CH_4 hydrate. These thermodynamic inhibition effects are due to the effect of inhibitors on cage stability through hydrogen bonding with water, which disrupt the formation of CH_4 hydrate lattices.

For the CH_4 hydrates in the presence of pure inhibitor (3.0 mol%) show that inhibition effect of glycine and [BMIM][BF_4] was generally shown to be similar to methanol (currently commercialized). It is because hydrate formation is inhibited through hydrogen bonding with water is the same for each inhibitor, but the inhibition mechanisms are different. Glycine has two functional groups (-NH_2 and –COOH), so it can easily from hydrogen bonds with water molecules. In addition, the ionic liquid of [BMIM][BF_4] contains electronegative anion (BF_4^-), which freely moves around the solution and interact with host water molecules to inhibit hydrate formation [36, 73-77]. Although each proposed inhibition mechanisms are not perfect, it has been fully explained by previous papers that the inhibitor mechanisms are different and the extent to which they act on hydrates is different. Moreover, our previous paper demonstrated that the inhibition mechanism of each inhibitor when hydrates are formed is different [81]. In this respect, two inhibitors were mixed and compared with each phase equilibria to observe if mixtures with different inhibition mechanisms had a more synergistic effect than that of a single inhibitor.

It is hard to observe significant thermodynamic inhibition effect in Figure 3.2.1., so equilibrium temperature differences (ΔT) between pure CH_4 hydrate and CH_4 + THI hydrates at 8.0 MPa were employed to more clearly identify the differences in the thermodynamic inhibition effects. As seen in Figure 3.2.2., they showed similar values (Δ T = 2 K) with methanol (3.0 mol%), a conventional inhibitor, and no synergistic effect could be confirmed in all mixtures (1.5 mol% + 1.5 mol%). The thermodynamic inhibition effects of mixture were found to be the value between the inhibition effects of the two inhibitors. Thus, it should be noted that thermodynamic synergistic effect was found to be insignificant even if the two inhibitors had different inhibition mechanisms because it is related to molecular interaction between water and inhibitor. As is well known, intrinsic properties and the number of water inhibitors are the biggest factors influencing the thermodynamic inhibition effect [21, 24].

However, the two inhibitors are unlikely to cause chemical reactions in water, so there is no significant difference in the number of molecules and their nature, resulting in no thermodynamic synergy

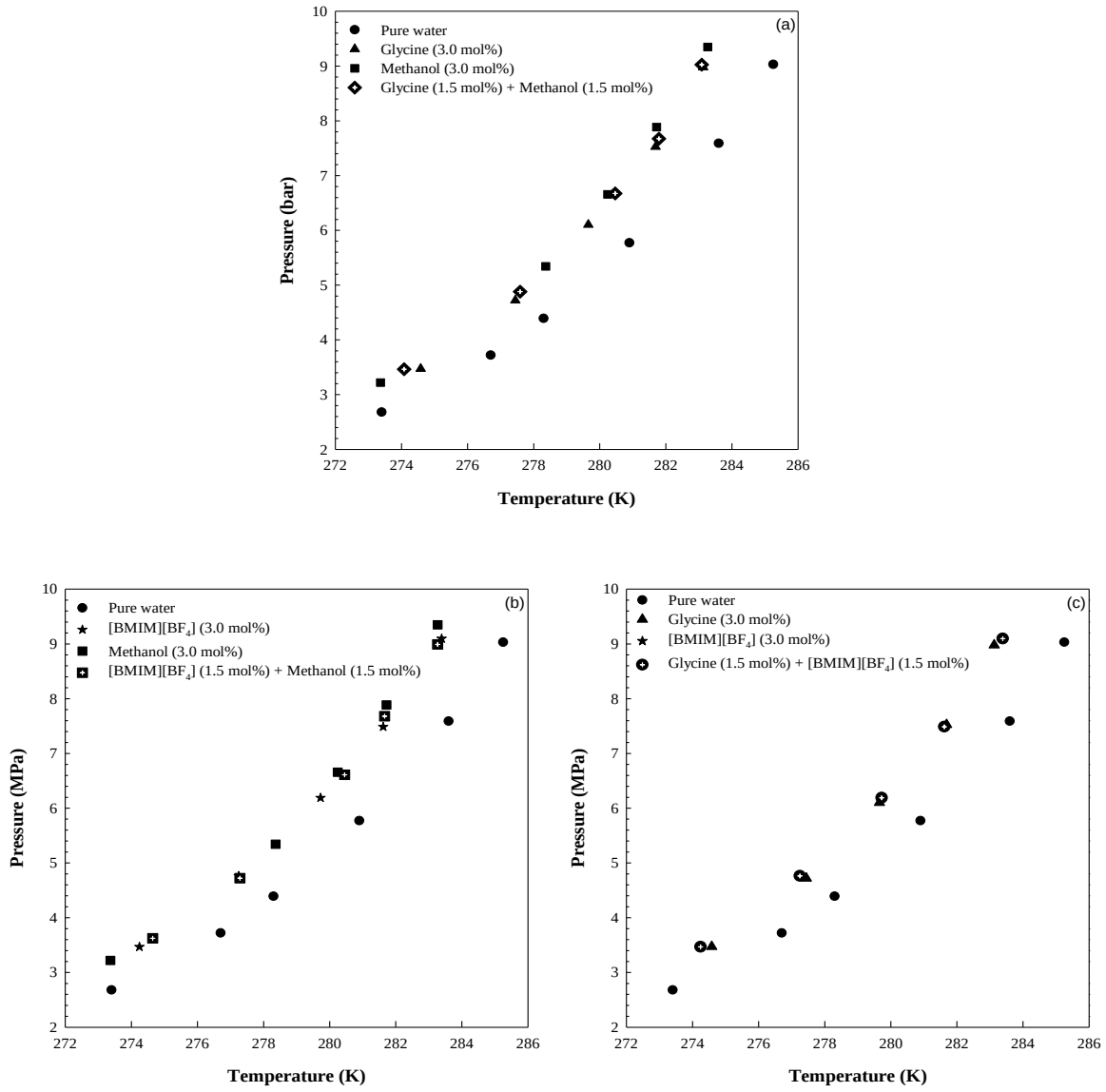

Figure 3.2.1. Phase equilibria of CH_4 hydrate with inhibitor mixtures [78, 81].

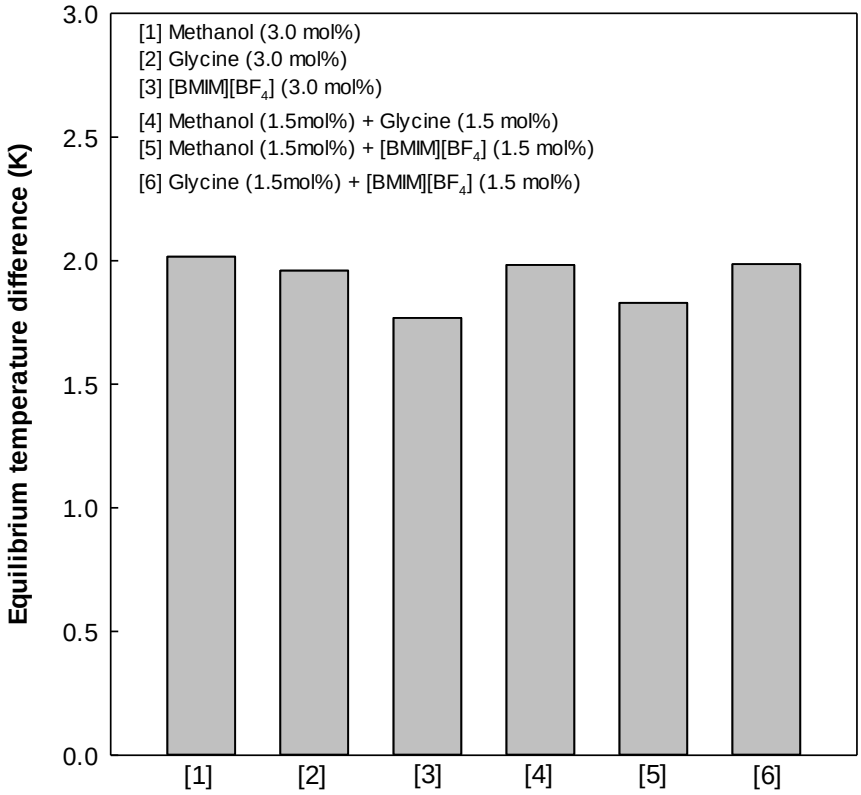

Figure 3.2.2. Equilibrium temperature differences between CH_4 hydrate and CH_4 + inhibitor hydrates at 8.0 MPa [78, 81].

Table 3.2.1. Hydrate phase equilibrium data of the CH_4 + inhibitor mixture (1.5 mol% + 1.5 mol%) + water systems.[a]

Methanol + Glycine		Methanol + [BMIM][BF_4]		Glycine + [BMIM][BF_4]	
T (K)	P (MPa)	T (K)	P (MPa)	T (K)	P (MPa)
274.1	3.47	274.6	3.62	275.0	3.51
277.6	4.88	277.3	4.72	277.7	4.73
280.5	6.67	280.4	6.61	280.4	6.60
281.8	7.67	281.7	7.68	281.8	7.71
283.1	9.02	283.3	8.99	283.0	9.04

[a] Standard uncertainties u are u(T) = 0.1 K and u(P) = 0.02 MPa.

3.2.3. Structure characteristic configuration

The PXRD analysis of gas hydrates is a powerful method for identifying information on their crystal structure, and clarify the influence of inhibitors on the CH_4 hydrate. Figure 3.2.3. present PXRD patters and reliable factors (lattice parameter, R_{wp}) of hydrate structure in the presence of methanol (3.0 mol%) and inhibitor mixtures (1.5 mol% + 1.5 mol%). As expected, pure CH_4 hydrates was identified as cubic sI (space group *Pm3n*) and a lattice parameter of a = 11.85 Å. In addition, the CH_4 + methanol, CH_4 + methanol + glycine, CH_4 + methanol + [BMIM][BF_4], CH_4 + glycine + [BMIM][BF_4] hydrates were also identified as cubic sI (space group *Pm3n*) with lattice parameters of 11.85 Å, 11.86 Å, 11.86 Å, 11.86 Å, respectively. It should be suggested that glycine, and [BMIM][BF_4] are too large to enclathrated in the small 5^{12} and large $5^{12}6^2$ cages of sI hydrates because of van der Waals radius values, so they reside on the outside of the cages or are partly involved in cages to disrupt the water-water networks.

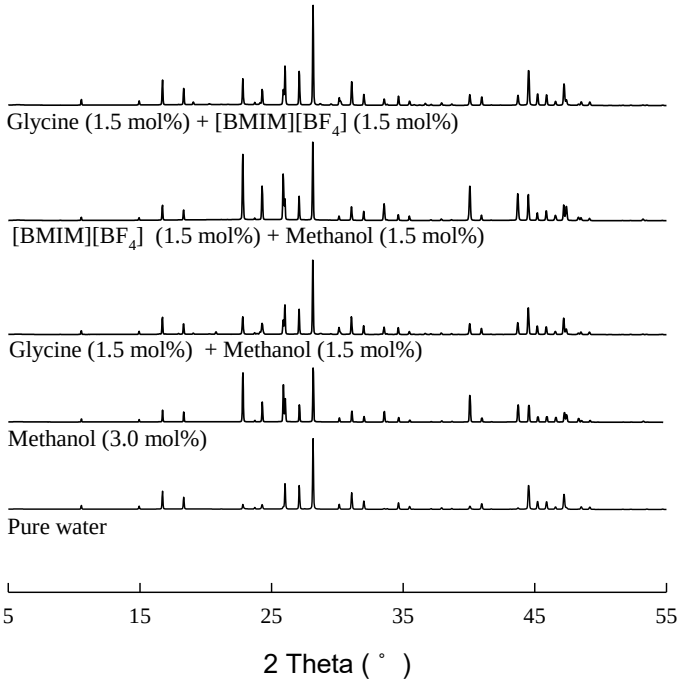

Figure 3.2.3. PXRD patterns of CH_4 hydrates in the presence of inhibitor mixtures (1.5 mol% + 1.5 mol%) [81].

3.2.4. Gas uptake analysis

It was confirmed that thermodynamic synergistic effects were not observed in all mixtures, but it implied that the kinetic properties will be different because they show different cage-specific inhibition mechanisms during CH_4 hydrate formation. In this regard, the gas uptake analysis is a fundamental study to examine the hydrate growth pattern and measure the initial stage of hydrate formation rate in the presence of inhibitors to observe the kinetic synergy effect of each mixture. The Figure 3.2.4. shows gas uptake curves (a) and percent conversion of water into CH_4 hydrates (C_{WH}) (b) in the presence of methanol (3.0 mol%) and inhibitor mixtures (1.5 mol% + 1.5 mol%), and they were compared with pure CH_4 hydrate. The amount of consumed gas during the hydrate formation were expressed as the ratio of moles of consumed gas to moles of initially charged water, and are closely related to the total amount gas trapped in the empty cages of hydrates.

The experimental results clearly show that the amount of gas captured in CH_4 hydrates + various inhibitors is smaller than pure CH_4 hydrate at given temperature and pressure conditions. For the pure CH_4 hydrate, gas uptake dramatically increased after nucleation, and gas uptake ratio reached 0.14 and C_{WH} was 88.3 % at the end of hydrate formation, which was smaller than theoretical ratio because of low driving force ($\Delta T = 4$ K). In addition, CH_4 hydrate formations in the presence of methanol, glycine + methanol, and [BMIM][BF_4] + methanol did not significantly inhibit hydrate growth after the nucleation of CH_4 hydrates, but they were good in terms of C_{WH} (low hydrate conversion). In all cases, the C_{WH} was less than 60%, with methanol showing the lowest amount of hydrate conversion (C_{WH} = 48.6 %), which was close to half of pure CH_4 hydrate (C_{WH} = 88.3 %). In addition, CH_4 hydrates in the presence of glycine + methanol and [BMIM][BF_4] + methanol systems indicate that gas consumption increased abruptly during initial stage (approximately 0-50 min), but they growth slowly after initial stage. Moreover, C_{WH} of glycine + methanol and [BMIM][BF_4] + methanol on CH_4 hydrates indicate 56.7% and 57.2%, respectively. This suggests that the intrinsic kinetics of each inhibitor affected hydrate growth tendency and conversion of water during hydrate formation.

Furthermore, the most notable point was that in the glycine + [BMIM][BF_4] system, CH_4 entered the cage very slowly from the initial to the final of the hydrate formation. These results can be seen as cage-specific inhibition mechanisms from the previous study, which demonstrated that glycine and [BMIM][BF_4] have a large effect on large $5^{12}6^2$ and small 5^{12} cages, respectively, preventing CH_4 molecules from entering the cages. Thus, glycine and [BMIM][BF_4] have a significant effect on each cage, then considerably reduced the growth rate of CH_4 hydrates. To support this kinetic synergism of glycine and [BMIM][BF_4] mixture on CH_4 hydrate, next section will demonstrate the synergy effect of

glycine and [BMIM][BF_4] by measuring the captured CH_4 molecules in small and large cages using in-situ Raman spectroscopy.

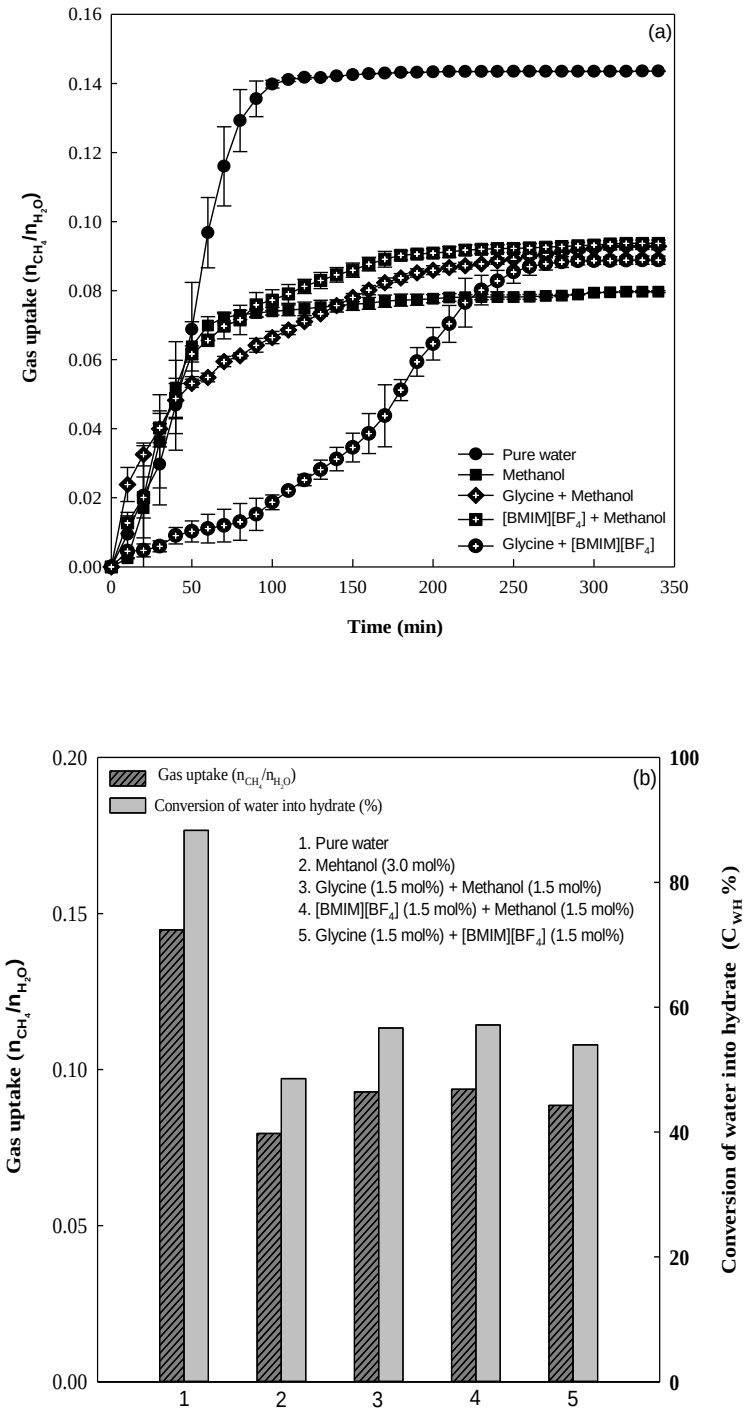

Figure 3.2.4. (a) Gas uptakes during hydrate formation in the presence of inhibitors. (b) Comparison of gas uptakes and percent conversion of water into hydrates for pure CH_4, CH_4 + glycine, and CH_4 + [BMIM][BF_4] hydrates [81].

3.2.5. Microscopic evidence of synergism of glycine and [BMIM][BF_4] mixture on CH_4 hydrate

To examine the enclathration of gas and identify the hydrate crystal structure during hydrate formation in the presence of glycine (1.5 mol%) + [BMIM][BF_4] (1.5 mol%), time-dependent Raman spectra for the enclathrated CH_4 molecules under $\Delta T = 4$ K condition was collected in the range of 2880-2930 cm^{-1}. It is known that the captured CH_4 molecules in large cages and small cages of sI hydrate was observed at 2905, and 2915 cm^{-1}, respectively. These results were confirmed in the Figure 3.2.5. and 6., and no structural singularities were found in the PXRD results, so they were sI hydrates.

Figure 3.2.5. gives the Raman spectra of pure CH_4 hydrate nucleation (a) and formation (b). The CH_4 peaks of small 5^{12} cages and large $5^{12}6^2$ cages were observed to grow simultaneously at 2905 and 2915 cm^{-1} 30 min after the stirring was started. In addition, both cages continued to grow and became almost completed approximately 150 min after the hydrate growth. In contrast to pure CH_4 hydrate, the time-dependent Raman spectra of CH_4 hydrate in the presence of glycine (1.5 mol%) and [BMIM][BF_4] (1.5 mol%) mixture indicates that the induction time (the time period necessary for the appearance of the very first hydrate cluster) was approximately 100 min because glycine and [BMIM][BF_4] also work as KHI not only THI in Figure 3.2.6 (a). In addition, Figure 3.2.6 (b) shows the growth pattern of glycine (1.5 mol%) and [BMIM][BF_4] (1.5 mol%) mixture. The initial growth pattern of glycine and [BMIM][BF_4] mixture shows a different growth tendency than pure CH_4 hydrate. The two cages grow simultaneously in pure CH_4 hydrates, whereas the glycine and [BMIM][BF_4] mixture initially inhibit the growth of the small 5^{12} cages for 80 minutes and both cages increased gradually rather than abruptly, like pure hydrate, and reached constant approximately at 260 min.

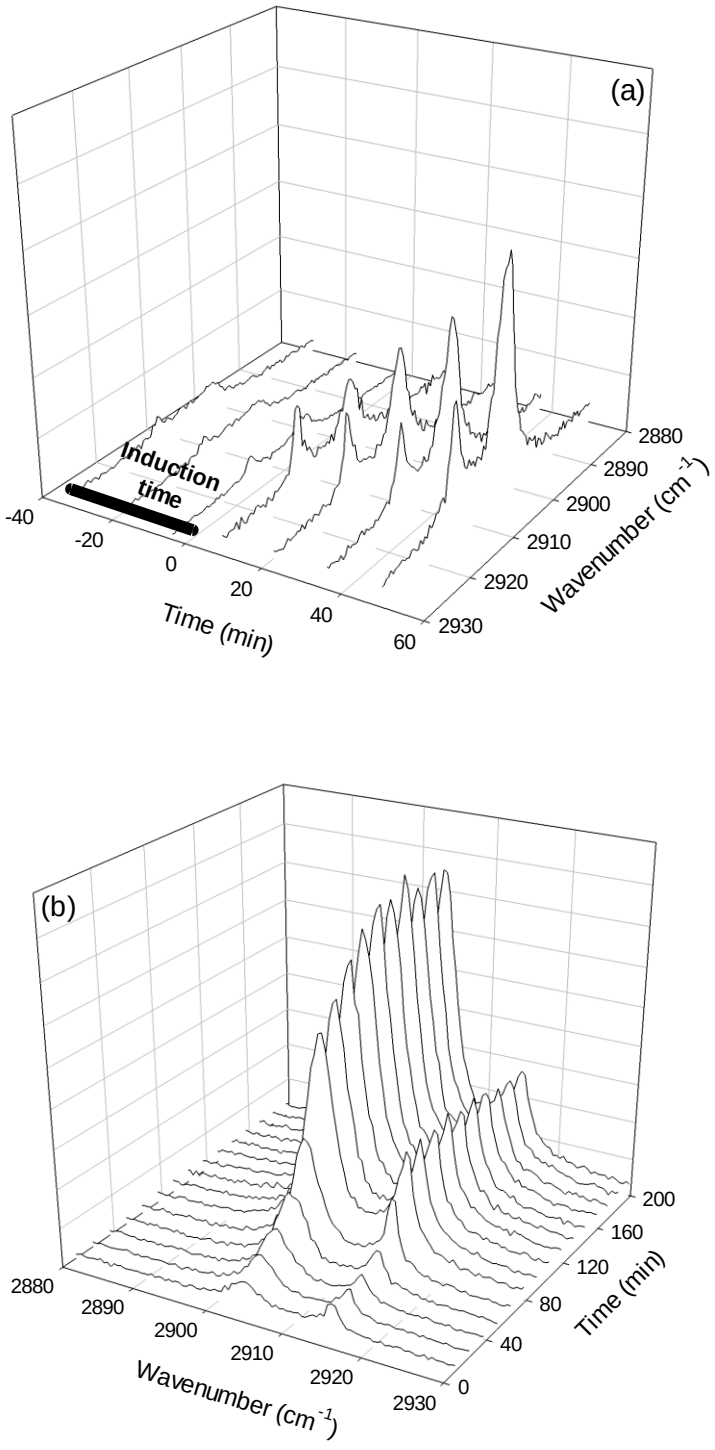

Figure 3.2.5. (a) Measurement of induction time and (b) in-situ Raman spectra of pure CH_4 hydrates growth at 8.0 MPa and $\Delta T = 4.0$ K.

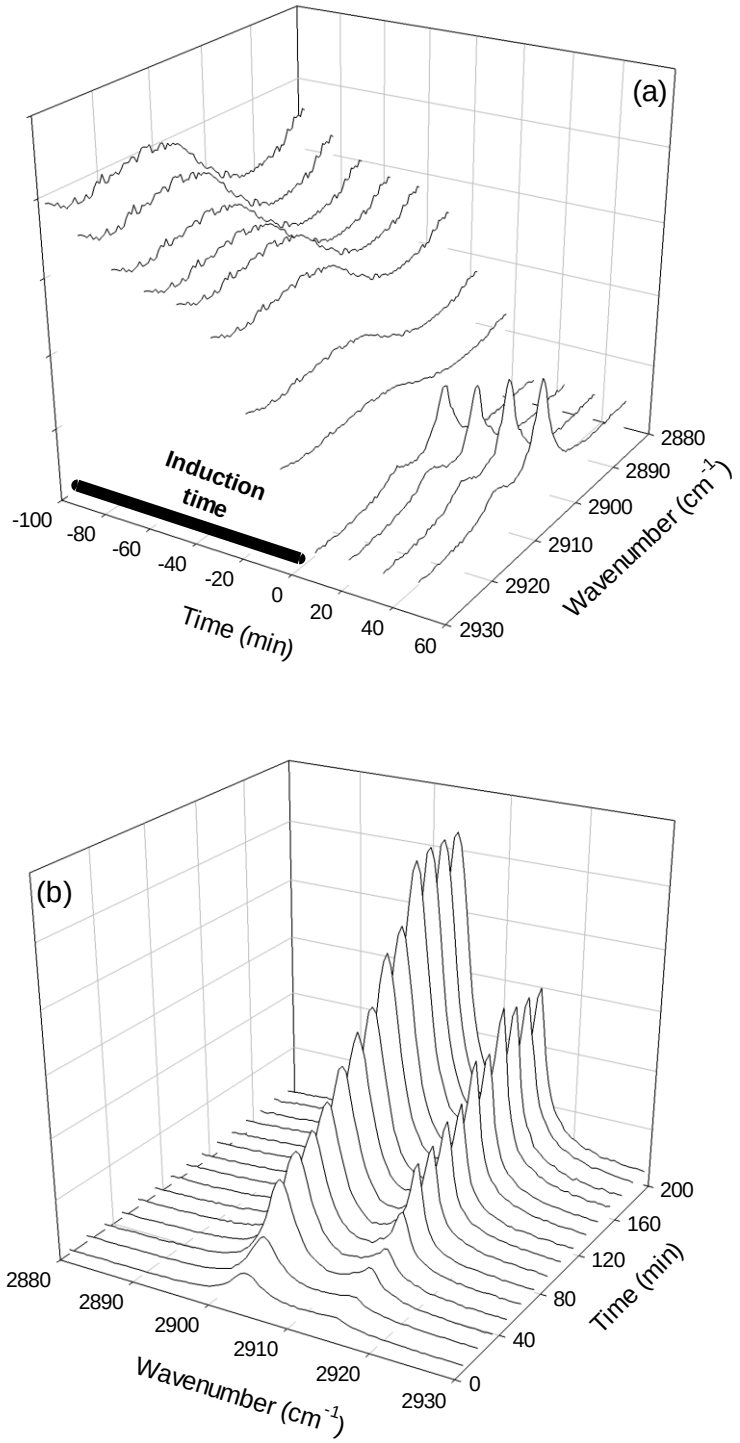

Figure 3.2.6. (a) Measurement of induction time and (b) in-situ Raman spectra of CH_4 + Glycine (1.5 mol%) + [BMIM][BF_4] (1.5 mol%) hydrates growth at 8.0 MPa and ΔT = 4.0 K.

To identify these growth patterns more clearly, changes in the area ratio (A_L/A_S) of two Raman peaks and the resulting fractional cage occupancy (θ) in both the small 5^{12} cages (θ_S) and large $5^{12}6^2$ cages (θ_L) of CH_4 hydrate with and without inhibitor mixture were obtained in Figure 3.2.7. In the case of pure CH_4 hydrate, the A_L/A_S gradually increased and converged to 3.15 after 150 min. At this time, most methane molecules are trapped in the small cages in the early stages of hydrate formation, resulting θ_S closes to 1.00 and decreased slightly (0.92) after 150 min. Moreover, the θ_L exhibits a value of 0.60 at the beginning of the hydrate formation, suggesting that methane molecules prefer to enter the small 5^{12} cages rather than large $5^{12}6^2$ cages. These trends change as the hydrate formation progresses and the CH_4 molecules participate in the large $5^{12}6^2$ cages, then θ_L converges to 0.97.

However, CH_4 hydrate growth tendency of A_L/A_S, θ_S and θ_L in the presence of glycine (1.5 mol%) and [BMIM][BF_4] (1.5 mol%) mixture was totally different from that of pure CH_4 hydrate. Due to cage-specific inhibition of [BMIM][BF_4] on small 5^{12} cages, the CH_4 molecules are hard to be captured in small 5^{12} cages during initial hydrate growth, so CH_4 molecules only enclathrated in large $5^{12}6^2$ cages. However, after 80 minutes, CH_4 were also captured in the small 5^{12} cages, which resulted in the θ_S value reached to 1.00. This suggests that [BMIM][BF_4] prevents the CH_4 molecule from entering into the small 5^{12} cages, but after a certain period of time, the inhibition effect is reduced and the CH_4 molecules rapidly enter the small 5^{12} cages. In addition, large $5^{12}6^2$ cages are also affected by glycine during hydrate growth, while [BMIM][BF_4] has a large effect on the initial stage of hydrate growth. The initial θ_L value was 0.66 and increased slightly as the hydrate was grown, but not as rapidly as pure CH_4 hydrate. Moreover, θ_L value after the reaction was 0.88, which was much smaller than the value of pure CH_4 hydrate (0.97), so it could be suggested that glycine continues to affect large $5^{12}6^2$ cage growth, consequently preventing CH_4 molecules from entering the large cages. As a result, the cage-specific inhibition effects identified in the previous studies were confirmed once again, which worked differently on cage growth over time. Occupancy of CH_4 molecules in the small cages was very low in the early stage of hydrate growth due to the influence of [BMIM][BF_4], and glycine generally prevented the incorporation of CH_4 molecules into the large cages during hydrate formation, resulting in slower growth rate, lower θ_L and lower final A_L/A_S (2.65) values. Thus, the study of gas hydrate inhibitor using cage-specific inhibition mechanism for the first time in this study is not only very novel, but also very valuable as a fundamental study to be applied to the actual field to pursue the injection of eco-friendly and efficient inhibitors.

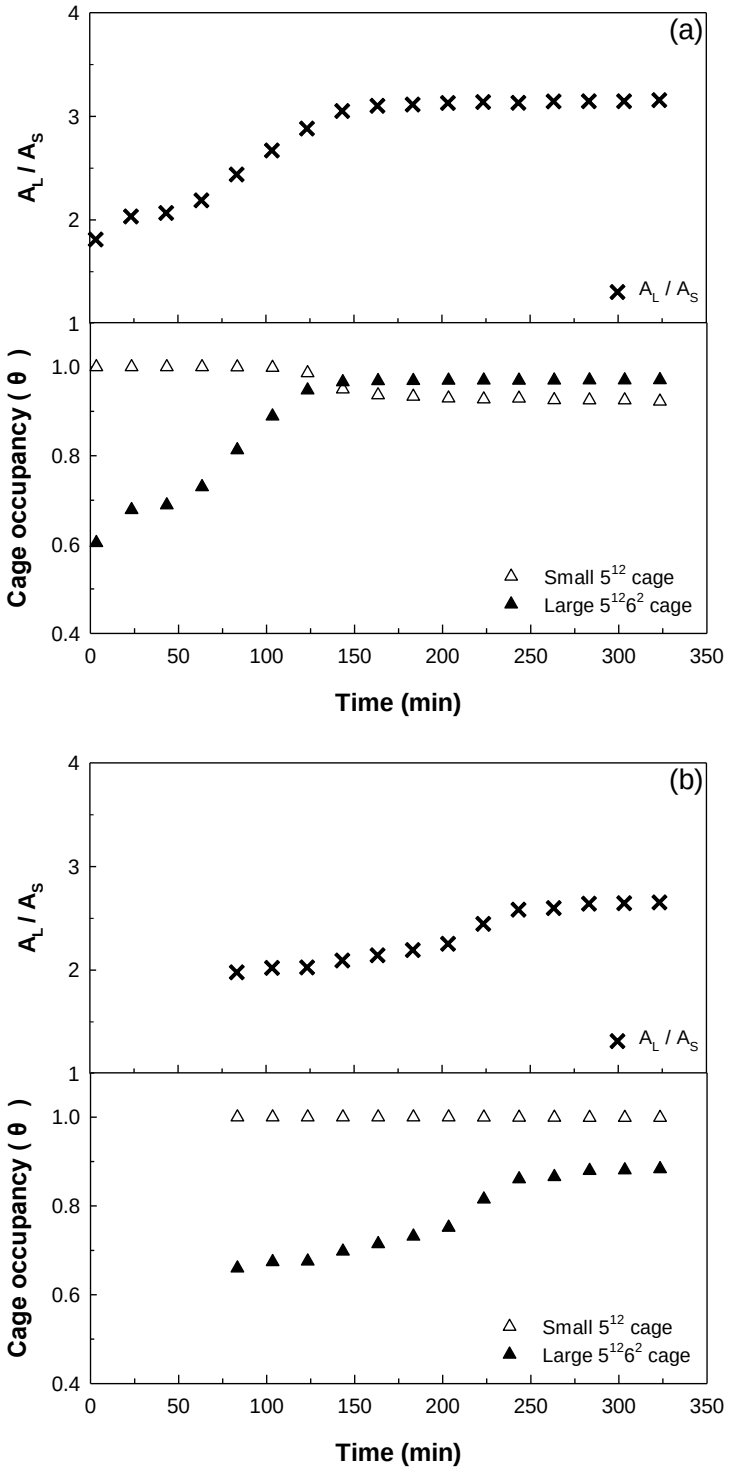

Figure 3.2.7. Changes in A_L/A_S and cage occupancy (θ_L and θ_S) at a given time during hydrate formation of (a) pure water, (b) glycine (1.5 mol%) + [BMIM][BF_4] (1.5 mol%) solutions.

3.2.6. Conclusions

In this study, thermodynamic, microscopic and kinetic experiments have been conducted on the synergistic effects of cage-specific inhibition mechanisms for their potential applications in flow assurance. The phase equilibria of the CH_4 hydrates in the presence of inhibitor mixtures indicated that thermodynamic synergy effects were hard to be observed for all cases. Besides, PXRD analyses demonstrated that the inhibitor mixtures did not affect on cage characteristics, so all CH_4 hydrates with and without inhibitors were identified as cubic sI. It is because they inhibit the formation of cages through hydrogen bonding and CH_4 molecules entering the cage, not the structure itself. Contrary to the above results, noticeable synergistic inhibition effect was observed in kinetic analyses. Gas uptake results confirmed that gas hydrate growth was slow in all mixtures, but glycine (1.5 mol%) + [BMIM][BF_4] (1.5 mol%) mixture considerably retard gas uptake. Furthermore, their C_{WH} is much smaller than without inhibitors, which may provide evidence that even if hydrates are generated in the actual field, they can have fluidity. Finally, hydrate growth patterns and induction time of CH_4 hydrate in the presence of glycine (1.5 mol%) + [BMIM][BF_4] (1.5 mol%) mixture were measured by in-situ Raman spectroscopy. Two inhibitors with the different inhibition mechanisms can be mixed to create a synergistic effect on each cage, thus delaying the nucleation and formation of cages significantly. Therefore, the synergistic inhibition concept presented for the first time in this study may be advantageous in terms of economy and environment due to their reduced operational costs and risk of spillage, which may be helpful to open up the new insights of practical applications for flow assurance.

3.3. Synergistic Kinetic Inhibition of Amino Acids and Ionic Liquids on CH_4 Hydrate for Flow Assurance

This chapter includes the published contents:

Lee D, Go W, Seo Y. Synergistic kinetic inhibition of amino acids and ionic liquids on CH_4 hydrate for flow assurance. Fuel 2020;263:116689.

3.3.1. Abstract

In this study, the kinetic inhibition effects of amino acids and ionic liquids and the potential synergism of their mixtures on CH_4 hydrates were investigated by adopting three different approaches. The sigma (σ) profiles of inhibitor molecules obtained from the Conductor-Like Screening Model for Real Solvents (COSMO-RS) software were used to estimate inhibitor–water interactions for the pre-screening of potential inhibitors, and thus glycine (an amino acid) and [BMIM][BF_4] (an ionic liquid) were selected as candidates for kinetic hydrate inhibitors (KHIs). A non-stirred high-pressure micro-differential scanning calorimeter (HP μ-DSC) revealed that the glycine (0.5 wt%) and [BMIM][BF_4] (0.5 wt%) mixture showed a synergism for CH_4 hydrate as a KHI. The kinetic inhibition synergism of the glycine (0.5 wt%) and [BMIM][BF_4] (0.5 wt%) mixture on CH_4 hydrate was double-checked using a stirred high-pressure autoclave. The onset temperature of the glycine (0.5 wt%) and [BMIM][BF_4] (0.5 wt%) mixture was found to be lower than that of poly(*N*-vinylcaprolactam) (PVCap; 1.0 wt%). Time-dependent Raman spectra demonstrated that the cage-specific inhibition of glycine and [BMIM][BF_4] caused kinetic inhibition synergism and the consequent slow growth rate of CH_4 hydrate. The synergistic kinetic inhibition of amino acids and ionic liquids will be helpful in understanding the accurate roles of inhibitors in inhibitor–water interactions and will contribute to opening up a new field related to the synergism of eco-friendly inhibitors for flow assurance in oil and gas pipelines.

3.3.2. Pre-screening of potential KHIs via σ profiles

The possibility and strength of hydrogen bonding between potential inhibitors (amino acids and ionic liquids) and water molecules were estimated using COSMO-RS by obtaining their σ profiles. The σ profiles of substances are helpful in understanding their precise molecular nature in terms of hydrophobicity and hydrophilicity. Each substance has a different σ-profile pattern that depends on its molecular structure and properties [80-83]. In this study, the σ profiles of five amino acids and five ionic liquids were obtained to examine their interaction with a water molecule and to elucidate their inhibition potential. Generally, a σ-profile pattern can be divided into three regions: polar hydrogen bond (H-bond) donor region, nonpolar region, and polar H-bond acceptor region. In Figure 3.3.1 (a) and Figure 3.3.2 (a), the peaks in the range of -0.0300 to -0.0084 e/Å^2 indicate the polar H-bond donor region, the peaks in the range of -0.0084 to +0.00084 e/Å^2 indicate the nonpolar region, and the peaks in the range of +0.0084 to +0.0300 e/Å^2 indicate the polar H-bond acceptor region.

As seen in Figure 3.3.1 (a) and Figure 3.3.2 (a), a water molecule has broad peaks in the polar H-bond donor and acceptor regions but relatively small peaks in the nonpolar region. It has been suggested that substances with σ-profile patterns similar to that of a water molecule can have strong inhibitor–water interactions through hydrogen bond formation between an inhibitor and water [82, 84]. However, the degree of polarity and the similarity of the σ profile should also be considered to accurately estimate the inhibitor–water interaction and to predict the potential of substances as inhibitors. In the σ profile of a substance, the peaks appearing in the polar regions represent the polarity (hydrophilicity) of a substance, whereas the ones in the nonpolar regions indicate the nonpolarity (hydrophobicity) of a substance. The degree of polarity of a certain substance can therefore be estimated by integrating the area of peaks separately in the polar regions and nonpolar regions.

The σ profiles of five amino acids and the areas of each σ profile corresponding to polar and nonpolar regions are depicted in Figure 3.3.1. Like water, all amino acids tested in this study exhibited several σ-profile peaks in the polar H-bond donor and acceptor regions, indicating that amino acids can have strong interactions with water and thus have the potential to interrupt hydrate nucleation. However, unlike water, the amino acids also had significant peaks in nonpolar regions. In order to quantify the σ-profile peaks and separate them into the contributions from polar regions and nonpolar regions, the peak areas of the σ profile of each amino acid were integrated in three different regions. Figure 3.3.1 (b) shows the area of the H-bond donor region (A_d), the area of the H-bond acceptor region (A_a), the total area of the polar H-bond regions ($A_{t\text{-}p} = A_d + A_a$), and the area of the nonpolar region ($A_{n\text{-}p}$) of amino acids. Because a substance with larger $A_{t\text{-}p}$ (higher polarity) and smaller $A_{n\text{-}p}$ (lower nonpolarity) is likely to form hydrogen bonds with water, an amino acid with a smaller difference between $A_{n\text{-}p}$ and $A_{t\text{-}$

$_p$ can be a better candidate as a gas hydrate inhibitor. As seen in Figure 3.3.1 (b), although glycine and alanine exhibited slightly smaller $A_{t\text{-}p}$, they had a much smaller difference between $A_{n\text{-}p}$ and $A_{t\text{-}p}$ than other amino acids due to their significantly smaller $A_{n\text{-}p}$. Valine, leucine, and isoleucine showed a larger difference between $A_{n\text{-}p}$ and $A_{t\text{-}p}$ because they had significantly larger $A_{n\text{-}p}$ despite the slightly larger $A_{t\text{-}p}$. Judging from the σ-profile patterns of amino acids examined in this study, glycine, with the smallest difference between $A_{n\text{-}p}$ and $A_{t\text{-}p}$, is expected to be the best candidate as a KHI.

The σ profiles of ionic liquids with a fixed cation, 1-butyl-3-methylimidazolium ($[BMIM]^+$), and five different anions are provided in Figure 3.3.2 (a). The peaks from the cation ($[BMIM]^+$) were mostly placed in the nonpolar region, whereas those from anions appeared in the polar H-bond acceptor region. A long alkyl chain group of the cation $[BMIM]^+$ contributed to the strong intensity of the σ profile in the nonpolar region, whereas anions with high electronegativity and polarity accounted for the sharp and strong peaks in the polar H-bond acceptor region. It should be noted that the ionic liquids examined in this study had relatively stronger peak intensities of the σ profiles than amino acids due to their longer alkyl chain group in the cation and higher electronegativity and polarity in the anions. The integrated areas of the σ profiles for five different ionic liquids are presented in Figure 3.3.2 (b). The difference between An-p and At-p for [BMIM][BF_4] and [BMIM][I] was smaller than that for other ionic liquids, and thus [BMIM][BF_4] and [BMIM][I] are expected to perform well in effectively inhibiting gas hydrate formation. It appears that ionic liquids containing $[SbF_6]^-$ and $[PF_6]^-$ as anions have little potential to be used as KHIs because a small part of the σ profiles for $[SbF_6]^-$ and $[PF_6]^-$ was also placed in the nonpolar region.

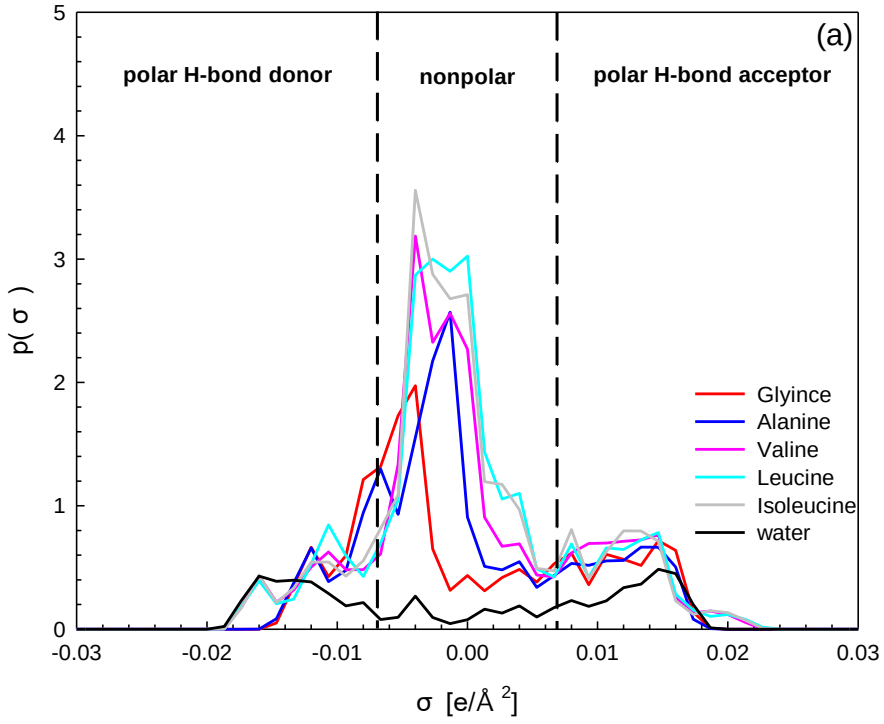

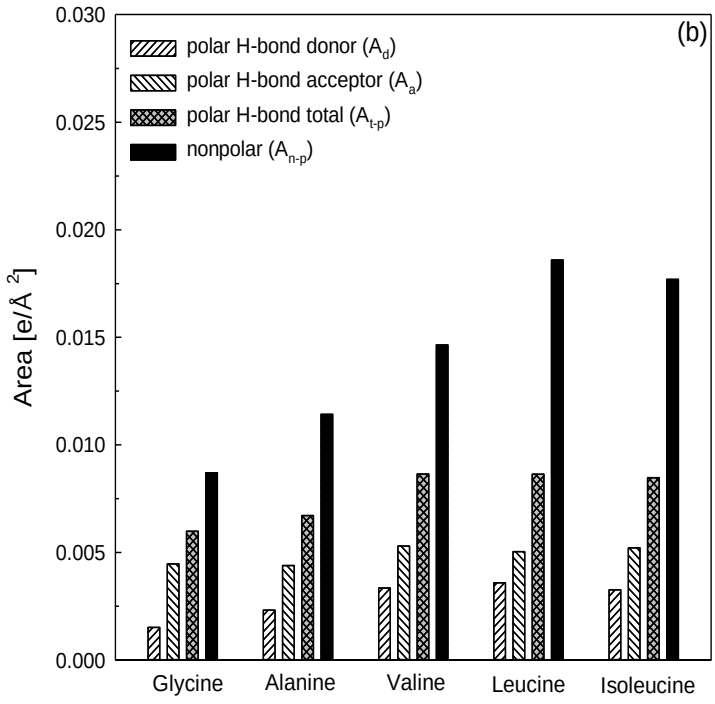

Figure 3.3.1. (a) The σ profiles of amino acids and water; (b) integrated areas of σ-profile peaks for amino acids in polar and nonpolar regions.

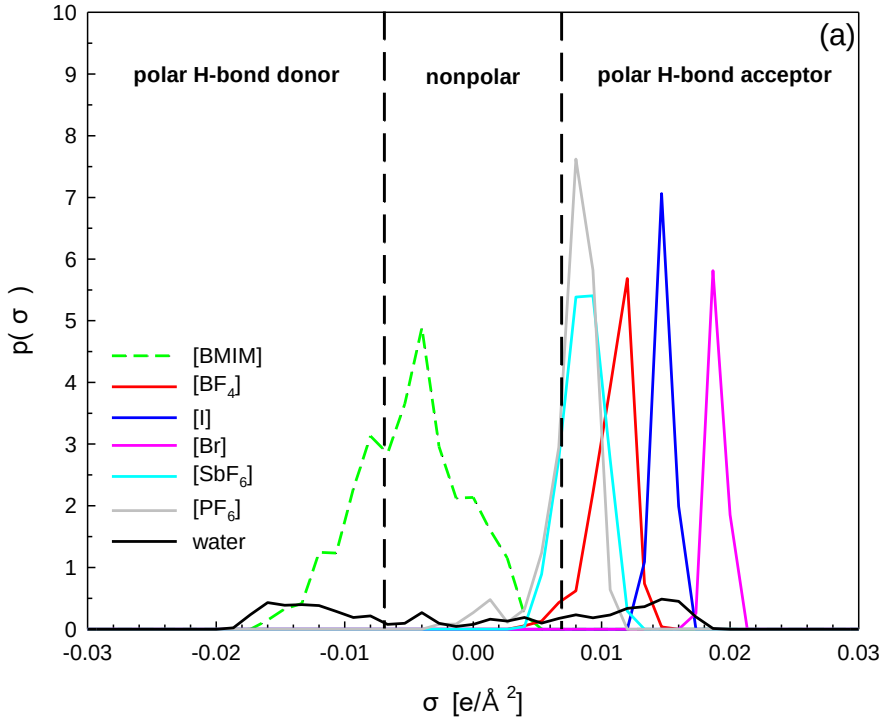

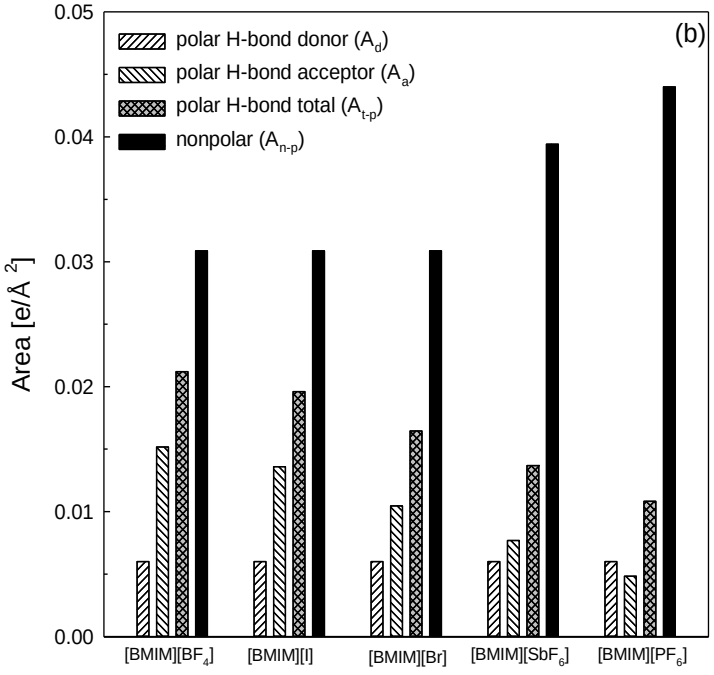

Figure 3.3.2. (a) The σ profiles of ionic liquids and water; (b) integrated areas of σ-profile peaks for ionic liquids in polar and nonpolar regions.

3.3.3. Onset temperature measurements of CH_4 hydrate using the high-pressure (HP) μ-DSC

From the σ-profile analysis using COSMO-RS, two amino acids (glycine and alanine) and two ionic liquids ([BMIM][BF_4] and [BMIM][I]) were found to be promising inhibitors and accordingly selected as candidates for potential KHIs. In this study, the temperature-ramping method with a constant cooling rate was adopted to measure the onset temperature of CH_4 hydrate in the presence of KHIs. There are several conventional apparatuses to measure the onset temperature of gas hydrates, including a high-pressure autoclave and a rocking cell. However, these apparatuses require a large amount of inhibitor solution for gas hydrate formation; thus, a longer time must be spent scanning the entire temperature range for the onset temperature measurement because a larger amount of solution requires a longer stabilization time for each temperature step. In contrast, the amount of solution required for the HP μ-DSC method was only approximately 4 mg, and thereby controlling the scanning rate was much easier [85-86]. Therefore, the HP μ-DSC is an ideal instrument for testing novel and expensive inhibitors without any prior or specific information because it requires less time and a smaller amount of solution to measure the onset temperature. In this study, the HP μ-DSC was first used to examine the kinetic inhibition performance and the potential synergism of each inhibitor, as well as the mixture of inhibitors. Figure 3.3.3 and Table 3.3.1 show the average onset temperatures of CH_4 + inhibitor hydrates measured by the HP μ-DSC. In the presence of KHIs, the onset temperatures were lowered due to the delayed and retarded nucleation of CH_4 hydrate, meaning the lower the onset temperature, the better the performance of the KHIs. It should be noted that at 10.0 MPa the onset temperature of CH_4 hydrate was 267.7 K, far below 273.15 K, due to the absence of stirring in the HP μ-DSC. In the presence of each pure inhibitor (1.0 wt%), PVCap was the most effective in delaying the nucleation of CH_4 hydrate and accordingly lowering the onset temperature. Ionic liquids ([BMIM][I] and [BMIM][BF_4]) performed slightly better than amino acids (glycine and alanine) in the non-stirred system. PVCap, glycine, and [BMIM][BF_4] were selected to examine potential synergism as KHIs when each pair was mixed together. As seen in Figure 3.3.3, it is very interesting to note that the mixture of glycine (0.5 wt%) + [BMIM][BF_4] (0.5 wt%) gave the lowest onset temperature (261.0 K), which was lower than that of each pure inhibitor (1.0 wt%) (263.5 K for glycine and 262.3 K for [BMIM][BF_4]) and lower than even that of PVCap (1.0 wt%) (261.1 K). However, no notable synergism was observed for the mixtures of PVCap (0.5 wt%) + glycine (0.5 wt%) and PVCap (0.5 wt%) + [BMIM][BF_4] (0.5 wt%) in the non-stirred system. The experimental results obtained from the HP μ-DSC method clearly showed that the mixture of glycine (0.5 wt%) + [BMIM][BF_4] (0.5 wt%) demonstrated kinetic inhibition synergism, was able to overcome the inhibition performance of each pure glycine (1.0 wt%) and pure [BMIM][BF_4] (1.0 wt%), and outperformed PVCap (1.0 wt%).

However, the above results were obtained in the non-stirred system using the HP μ-DSC, and thus the

performance of the abovementioned inhibitors should be double-checked in a stirred system using a high-pressure autoclave.

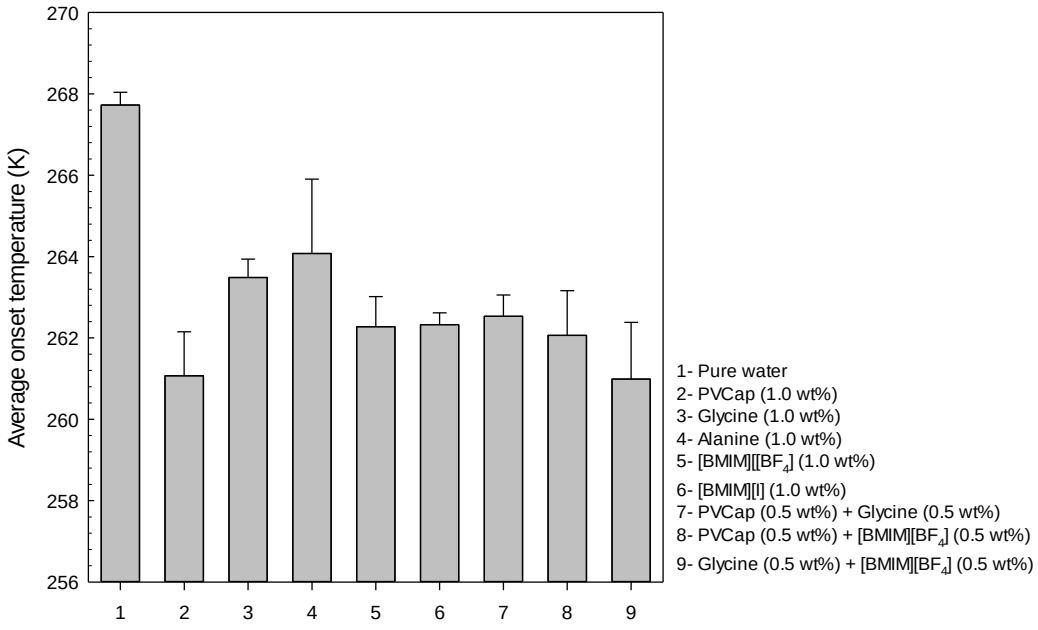

Figure 3.3.3. Average onset temperatures of CH_4 hydrates in the presence of PVCap, amino acids, ionic liquids, and inhibitor mixtures (HP μ-DSC).

Table 3.3.1. Average onset temperatures of CH_4 hydrates in the presence of inhibitors (HP μ-DSC).

Samples	Average onset temperature (K)	Onset temperature difference between pure water and inhibitor solution	rank	Group
pure water	267.7	0	-	-
PVCap (1.0 wt%)	261.1	6.6	2	1
Glycine (1.0 wt%)	263.5	4.2	7	3
Alanine (1.0 wt%)	264.1	3.6	8	3
[BMIM][BF_4] (1.0 wt%)	262.3	5.4	4	2
[BMIM][I] (1.0 wt%)	262.3	5.4	5	2
PVCap (0.5 wt%) + Glycine (0.5 wt%)	262.5	5.2	6	2
PVCap (0.5 wt%) + [BMIM][BF_4] (0.5 wt%)	262.1	5.6	3	2
Glycine (0.5 wt%) + [BMIM][BF_4] (0.5 wt%)	261.0	6.7	1	1

3.3.4. Onset temperature measurements of CH_4 hydrate using the high-pressure (HP) autoclave

The onset temperatures of CH_4 hydrates in the presence of inhibitors were also determined by the pressure drop using a high-pressure autoclave with mechanical stirring; they are presented in Figure 3.3.4 (a) and Table 3.3.2. As in the HP μ-DSC, for pure inhibitors (1.0 wt%) the onset temperature (277.9 K) of PVCap (1.0 wt%) was also the lowest in the high-pressure autoclave. The onset temperatures of amino acids (glycine and alanine) were similar to or slightly lower than ionic liquids (([BMIM][I] and [BMIM][BF_4]) under stirring conditions.

The onset temperatures of the PVCap (0.5 wt%) + glycine (0.5 wt%), PVCap (0.5 wt%) + [BMIM][BF_4] (0.5 wt%), and glycine (0.5 wt%) + [BMIM][BF_4] mixtures are provided in Figure 3.3.4 (b) and Table 3.3.2. Considering the onset temperatures of each pure inhibitor (1.0 wt%), it is clear that the PVCap + [BMIM][BF_4] and glycine + [BMIM][BF_4] mixtures showed synergism as KHIs. The synergism of the PVCap + [BMIM][BF_4] mixture was not surprising because several researchers have already reported that ionic liquids demonstrate the synergistic inhibition effect for delaying hydrate nucleation when mixed with polymer-based inhibitors in the stirred system [87-88]. However, this is the first discovery of a glycine + [BMIM][BF_4] mixture exhibiting the synergistic inhibition effect on CH_4 hydrate formation in both stirred and non-stirred systems. The onset temperatures of the glycine (0.5 wt%) + [BMIM][BF_4] (0.5 wt%) and PVCap (0.5 wt%) + [BMIM][BF_4] (0.5 wt%) mixtures were lower than that of PVCap (1.0 wt%) alone in the stirred system. The synergism of amino acids + ionic liquids and PVCap + ionic liquids would be of great importance in understanding the inhibition mechanism of each inhibitor and reducing the use of polymer-based inhibitors by partially replacing them with eco-friendly inhibitors like amino acids and ionic liquids.

The average pressure drops after CH_4 hydrate formation and the pressure drop profiles during CH_4 hydrate formation in the presence of inhibitors measured using the high-pressure autoclave are presented in Figure 3.3.5. As shown in Figure 3.3.5 (a), the pressure drops after CH_4 hydrate formation were dependent on the types of inhibitors used. The magnitude of the pressure drop after gas hydrate formation is proportional to the amount of gas hydrate formed during reaction. In the presence of PVCap (1.0 wt%), the pressure drop was significantly smaller than that of pure water. However, when amino acids (glycine and alanine) or ionic liquids ([BMIM][BF_4] and [BMIM][I]) were added, the final pressure drops were comparable to or slightly higher than that of pure water. The inhibitor mixtures containing PVCap showed relatively lower pressure drops, whereas the pressure drop of the glycine + [BMIM][BF_4] mixture was larger than that of other inhibitor combinations.

As seen in Figure 3.3.5 (b), for pure water, CH_4 hydrate formation detected by a pressure drop started at a higher temperature and continued for a longer time. However, for PVCap (1.0 wt%) and the glycine

(0.5 wt%) + [BMIM][BF_4] (0.5 wt%) mixture, the pressure drop occurred abruptly at a much lower temperature, indicating that both PVCap (1.0 wt%) and the glycine (0.5 wt%) + [BMIM][BF_4] (0.5 wt%) mixture functioned well as KHIs. It should be noted that even though so-called catastrophic growth of CH_4 hydrate occurred after a long delay of gas hydrate nucleation for both PVCap (1.0 wt%) and the glycine (0.5 wt%) + [BMIM][BF_4] (0.5 wt%) mixture, the final pressure drop for the glycine (0.5 wt%) + [BMIM][BF_4] (0.5 wt%) mixture, which is equivalent to the conversion of water into CH_4 hydrate, was much larger than that for PVCap (1.0 wt%). Because the types of inhibitors can affect hydrate conversion and the delay of nucleation, not only the induction time before gas hydrate formation but also the growth behavior after gas hydrate formation should be considered in inhibitor selection and the performance evaluation of the inhibitors for actual applications.

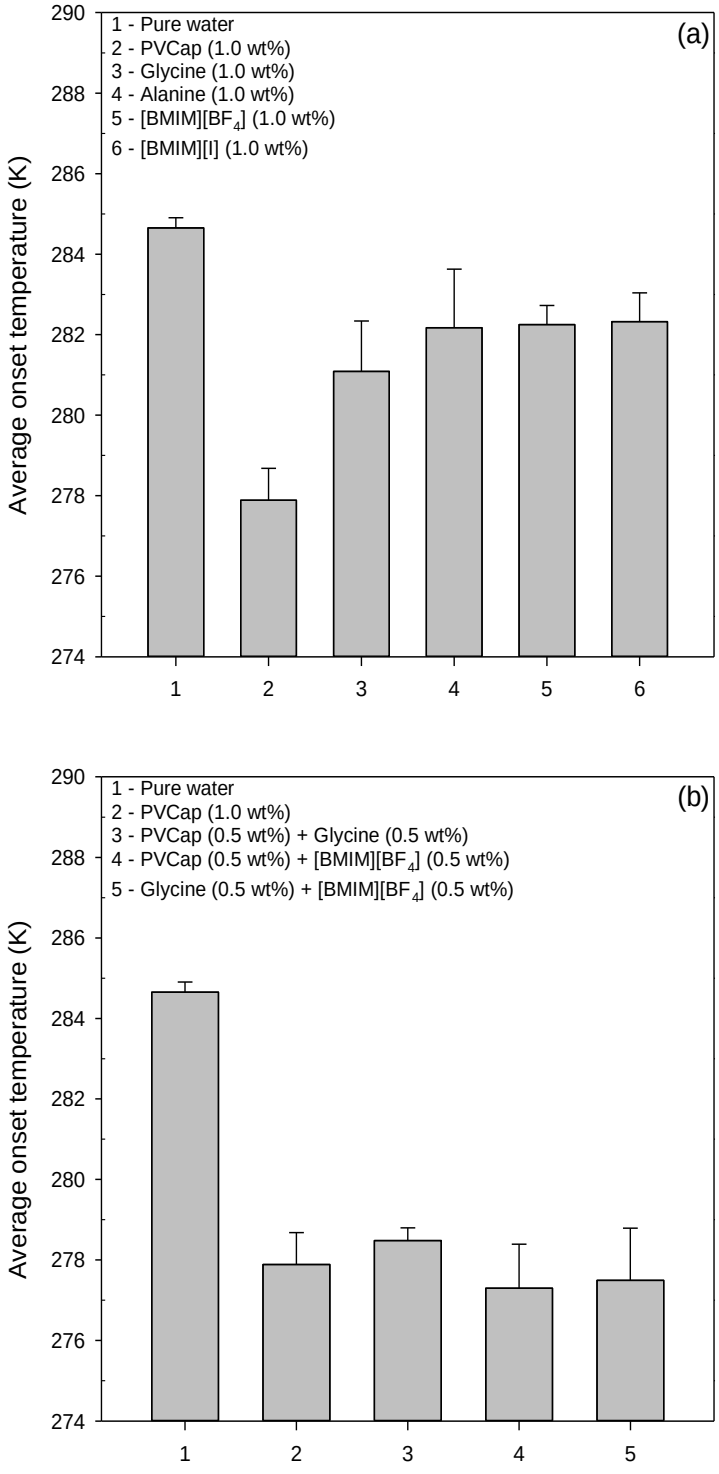

Figure 3.3.4. Average onset temperatures of CH_4 hydrates (high-pressure autoclave) (a) in the presence of PVCap, amino acids, and ionic liquids. (b) Average onset temperatures in the presence of PVCap and inhibitor mixtures.

Table 3.3.2. Average onset temperatures of CH_4 hydrates in the presence of inhibitors (high-pressure autoclave).

Samples	Average onset temperature (K)	Onset temperature difference between pure water and inhibitor solution	rank	Group
pure water	284.7	0	-	-
PVCap (1.0 wt%)	277.9	6.8	3	1
Glycine (1.0 wt%)	280.1	4.6	5	4
Alanine (1.0 wt%)	282.9	1.8	8	3
[BMIM][BF_4] (1.0 wt%)	282.3	2.4	6	3
[BMIM][I] (1.0 wt%)	282.3	2.4	7	3
PVCap (0.5 wt%) + Glycine (0.5 wt%)	278.5	6.2	4	2
PVCap (0.5 wt%) + [BMIM][BF_4] (0.5 wt%)	277.3	7.4	1	1
Glycine (0.5 wt%) + [BMIM][BF_4] (0.5 wt%)	277.5	7.2	2	1

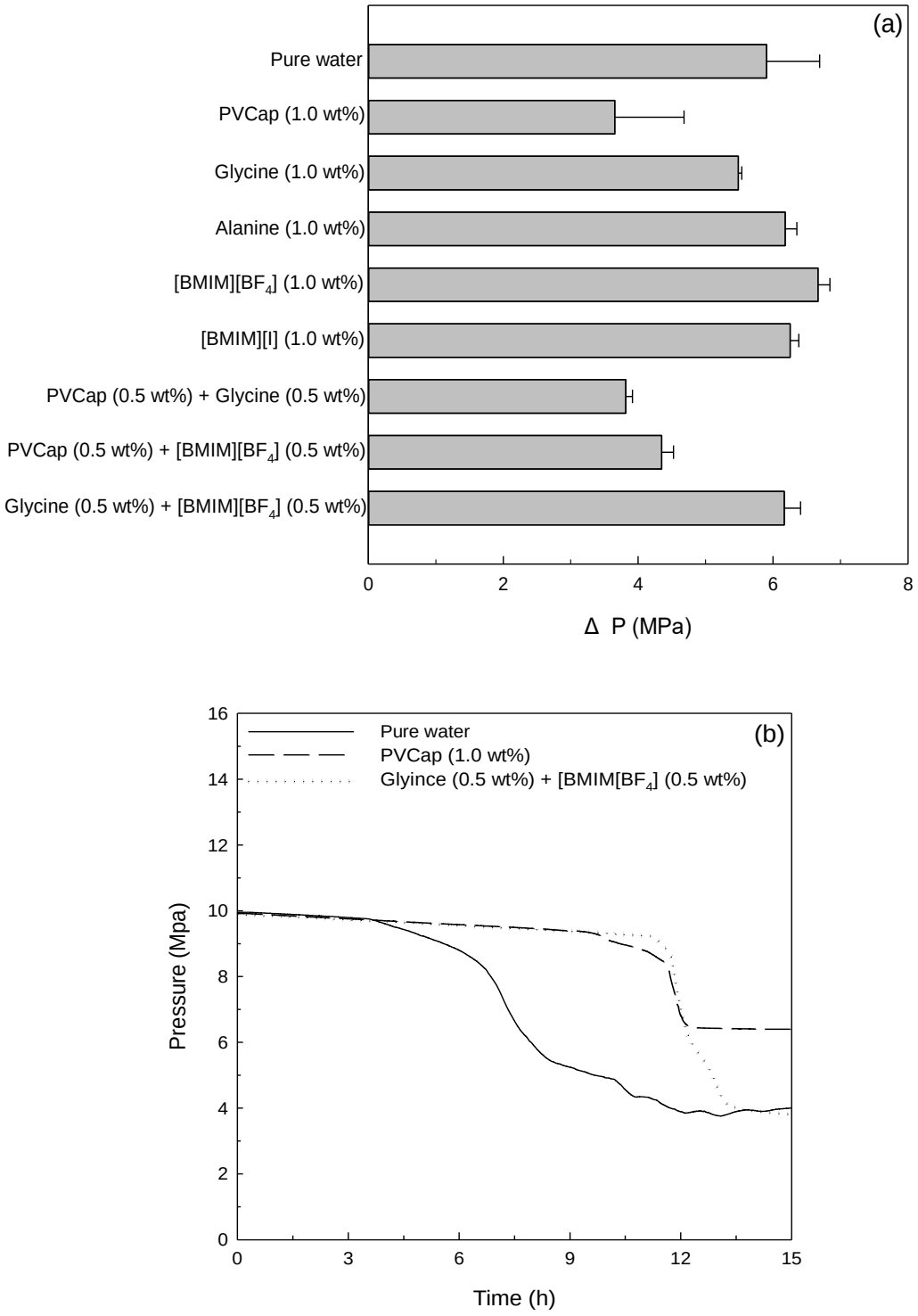

Figure 3.3.5. (a) Average pressure drops during CH_4 hydrate formation in the presence inhibitors; (b) pressure profiles during CH_4 hydrate formation for pure water, PVCap (1.0 wt%), and glycine (0.5 wt%) + [BMIM][BF_4] (0.5 wt%).

3.3.5. Growth patterns of methane hydrate in the presence of inhibitor mixtures

In situ Raman spectroscopy was used to investigate the kinetic inhibition synergism of the glycine (0.5 wt%) + [BMIM][BF_4] (0.5 wt%) mixture on CH_4 hydrate formation. Figure 3.3.6 shows the time-dependent Raman spectra of pure CH_4 hydrate and CH_4 + glycine (0.5 wt%) + [BMIM][BF_4] (0.5 wt%) hydrate. As the CH_4 hydrate formation progressed, both systems exhibited two Raman peaks at 2905 cm^{-1} and 2915 cm^{-1}, which correspond to CH_4 molecules enclathrated in the large $5^{12}6^2$ and small 5^{12} cages of sI hydrate, respectively. For the pure CH_4 hydrate shown in Figure 3.3.6 (a), two Raman peaks grew slowly at the early stage of CH_4 hydrate formation, enlarged rapidly after approximately 60 min, and then reached a plateau after 100 min. In contrast to pure CH_4 hydrate, the CH_4 + glycine (0.5 wt%) + [BMIM][BF_4] (0.5 wt%) hydrate showed different growth patterns despite the same driving force being used. As seen in Figure 3.3.6 (b), the growth rate of two Raman peaks was significantly reduced in the presence of the glycine (0.5 wt%) + [BMIM][BF_4] (0.5 wt%) mixture, and thereby CH_4 hydrate formation was completed after 150 min. In particular, the growth of the Raman peak corresponding to the small 5^{12} cages was strongly inhibited at the initial stage.

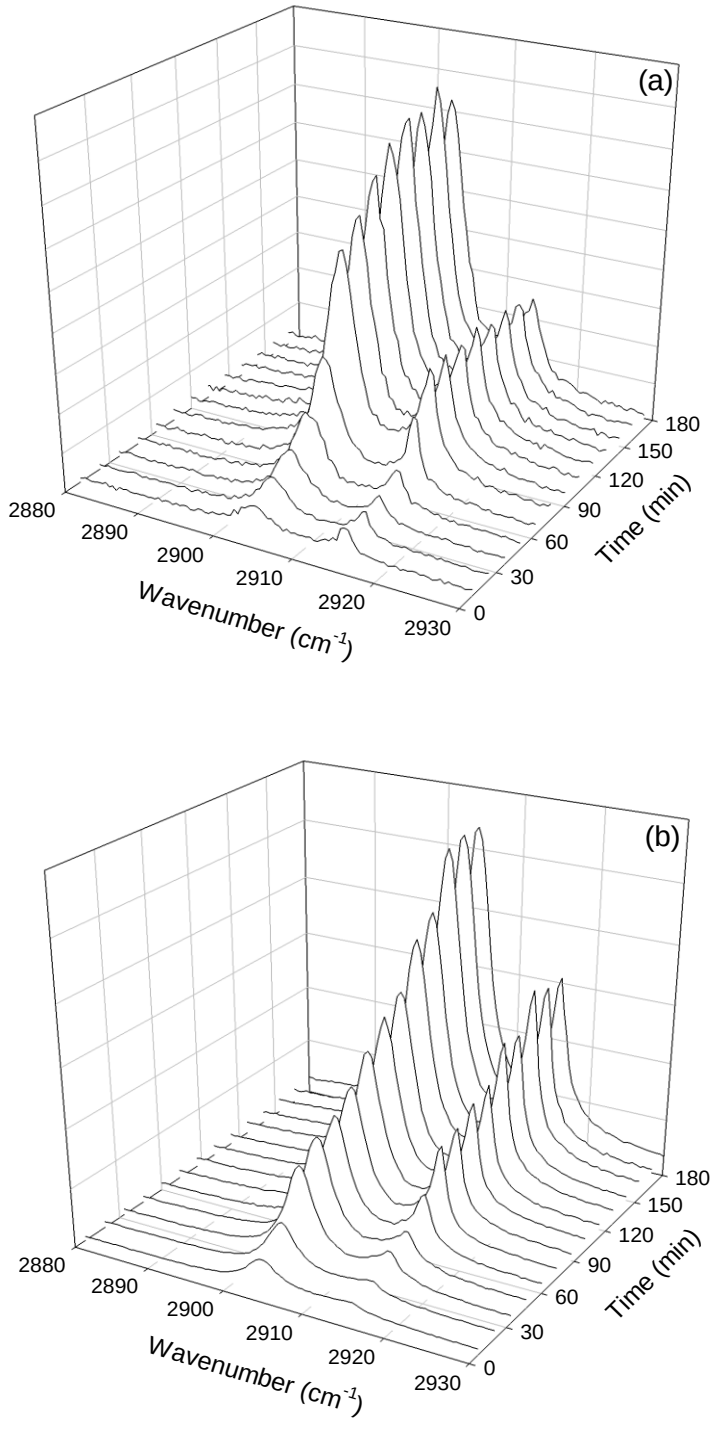

Figure 3.3.6. Time-dependent Raman spectra of (a) pure CH_4 hydrate and (b) CH_4 + glycine (0.5 wt%) + [BMIM][BF_4] (0.5 wt%) hydrate at 8.0 MPa and ΔT = 4.0 K.

The changes in the area ratio (A_L/A_S) of two Raman peaks and the fractional cage occupancy (θ) of CH_4 molecules in both the small 5^{12} cages (θ_S) and large $5^{12}6^2$ cages (θ_L) of sI hydrate were observed to examine the synergistic inhibition effect of the glycine + [BMIM][BF_4] mixture on CH_4 hydrate formation (Figure 3.3.7.). As seen in Figure 3.3.7 (a), because the small 5^{12} cages were more populated by CH_4 molecules than the large $5^{12}6^2$ cages at the beginning of pure CH_4 hydrate formation, the A_L/A_S value (~1.5) was lower than the theoretical one (3.0). However, after 70 min the θ_L value became slightly higher than the θ_S value due to the preferred occupation of CH_4 molecules in the large $5^{12}6^2$ cages. Thus, the final A_L/A_S value reached ~3.2. However, the changes in the A_L/A_S and θ values during CH_4 + glycine + [BMIM][BF_4] hydrate formation were totally different from those observed during pure CH_4 hydrate formation. At the initial stage of CH_4 + glycine + [BMIM][BF_4] hydrate formation, due to the lower occupancy of CH_4 in the small 5^{12} cages, the A_L/A_S value was ~4.4. However, as the gas hydrate formation proceeded, a rapid increase in the θ_S value resulted in a lowered A_L/A_S value, which finally reached ~2.6. The formation behavior of the CH_4 + glycine + [BMIM][BF_4] hydrate was significantly different from that of the pure CH_4 hydrate and was attributed to the cage-specific inhibition mechanism of glycine and [BMIM][BF_4]. Our previous work indicated that [BMIM][BF_4] is effective in hindering CH_4 molecules from occupying the small 5^{12} cages, whereas glycine predominantly prevents CH_4 molecules from entering the large $5^{12}6^2$ cages [89]. Even though the final A_L/A_S value of CH_4 hydrate in the presence of PVCap was also far below 3.0, this was because PVCap affected the formation of the large $5^{12}6^2$ cages of CH_4 hydrate [81, 90].

The injection of KHIs instead of THIs for the avoidance of gas hydrates in pipelines is advantageous because of their smaller required amount and consequently lower cost. The kinetic inhibition synergism of amino acids and ionic liquids due to their cage-specific inhibition mechanism can contribute to reducing the environmental impact, hydrate formation risk, and inhibitor usage. Further studies on the potential synergism of other eco-friendly inhibitor combinations need to be performed for environmental and economic purposes in oil and gas transmission lines.

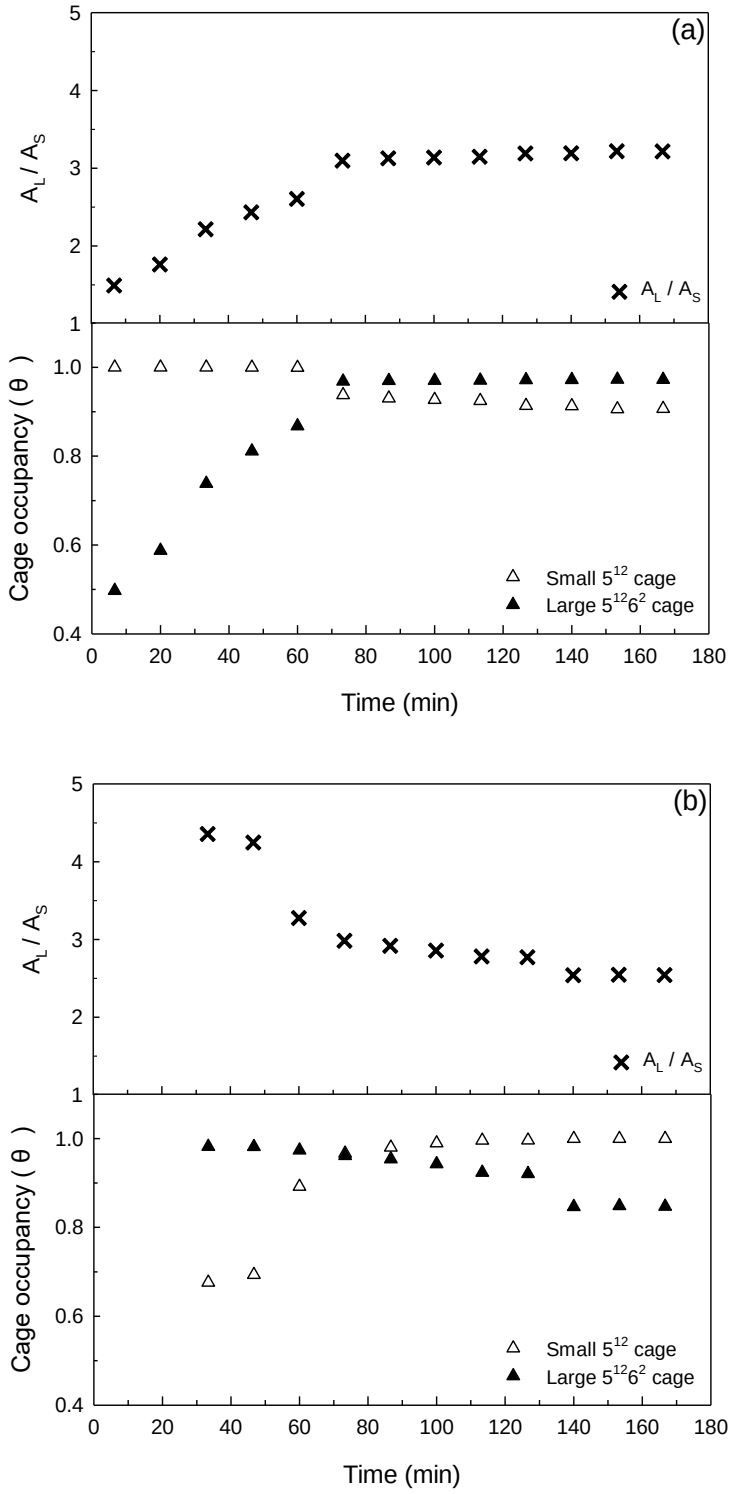

Figure 3.3.7. Changes in A_L/A_S and cage occupancy (θ) for (a) pure CH_4 hydrate and (b) CH_4 + glycine (0.5 wt%) + [BMIM][BF_4] (0.5 wt%) hydrate.

3.3.6. Conclusions

In this study, the inhibition effects of amino acids and ionic liquids and the potential synergism of their mixtures on CH_4 hydrate formation were examined for applications to flow assurance. The σ profiles of each inhibitor molecule obtained from the COSMO-RS software offered valuable insights into their ability to form hydrogen bonds with a water molecule by integrating their peak areas separately in the polar and nonpolar regions. Glycine among the amino acids and [BMIM][BF_4] among the ionic liquids, which had the smallest difference between $A_{n\text{-}p}$ and $A_{t\text{-}p}$, were selected as potential candidates for KHIs. The non-stirred HP μ-DSC revealed that the mixture of glycine (0.5 wt%) + [BMIM][BF_4] (0.5 wt%) gave the lowest onset temperature for CH_4 hydrate, indicating that the glycine and [BMIM][BF_4] mixture showed synergism as a KHI. The kinetic inhibition synergism of the glycine (0.5 wt%) + [BMIM][BF_4] (0.5 wt%) mixture was also observed in the stirred high-pressure autoclave. The onset temperature of the glycine (0.5 wt%) + [BMIM][BF_4] (0.5 wt%) mixture was found to be lower than that of PVCap (1.0 wt%) using both the non-stirred HP μ-DSC and stirred high-pressure autoclave methods. The synergistic inhibition effect of the glycine and [BMIM][BF_4] mixture on CH_4 hydrate was caused by the different inhibition mechanisms of each inhibitor; glycine inhibited the large $5^{12}6^2$ cages, whereas [BMIM][BF_4] affected the small 5^{12} cages of sI hydrate. Time-dependent Raman spectra of CH_4 hydrate in the presence of the glycine (0.5 wt%) + [BMIM][BF_4] (0.5 wt%) mixture confirmed the gradual growth of small and large cages and the cage-specific inhibition of glycine and [BMIM][BF_4]. Outcomes and new findings regarding synergism based on cage-specific inhibition will be very useful for a complete understanding of the inhibition mechanisms of eco-friendly inhibitors and the host–inhibitor interaction in gas hydrates, as well as for the selection and development of future inhibitors for flow assurance in gas and oil pipelines.

Chapter 4. Novel Inhibitors for Future Gas and Oil Industries

4.1. Recoverable and recyclable gas hydrate inhibitors based on magnetic nanoparticle-decorated metal–organic frameworks

This chapter includes the published contents:

Lee D, Jeoung S, Moon HR, Seo, Y. Recoverable and recyclable gas hydrate inhibitors based on magnetic nanoparticle-decorated metal–organic frameworks. Chem Eng J 2020;401:126081.

4.1.1. Abstract

In the oil and gas industries, the development of gas hydrate inhibitors is one of the most critical issues to prevent hydrate formation for flow assurance in pipelines. Low-dosage and recoverable/recyclable hydrate inhibitors are very important environmentally and economically. Herein, we propose a new class of kinetic hydrate inhibitors (KHIs) based on magnetic nanoparticle (NP)-decorated metal–organic frameworks (MOFs). As a KHI candidate, UiO-66 derivatives bearing different functional groups were examined, and UiO-66-NH_2 showed superior performance with low dosage (1 wt%) in terms of the onset temperature of CH_4 hydrate formation. To realize recoverability, magnetic Fe_3O_4 NPs were adopted to produce a core–shell-type composite, Fe_3O_4@UiO-66-NH_2. This core–shell inhibitor was successfully recovered and reused, exhibiting a comparable performance to fresh UiO-66-NH_2. This first example of a MOF as a KHI will contribute toward a new era of recoverable gas hydrate inhibitors.

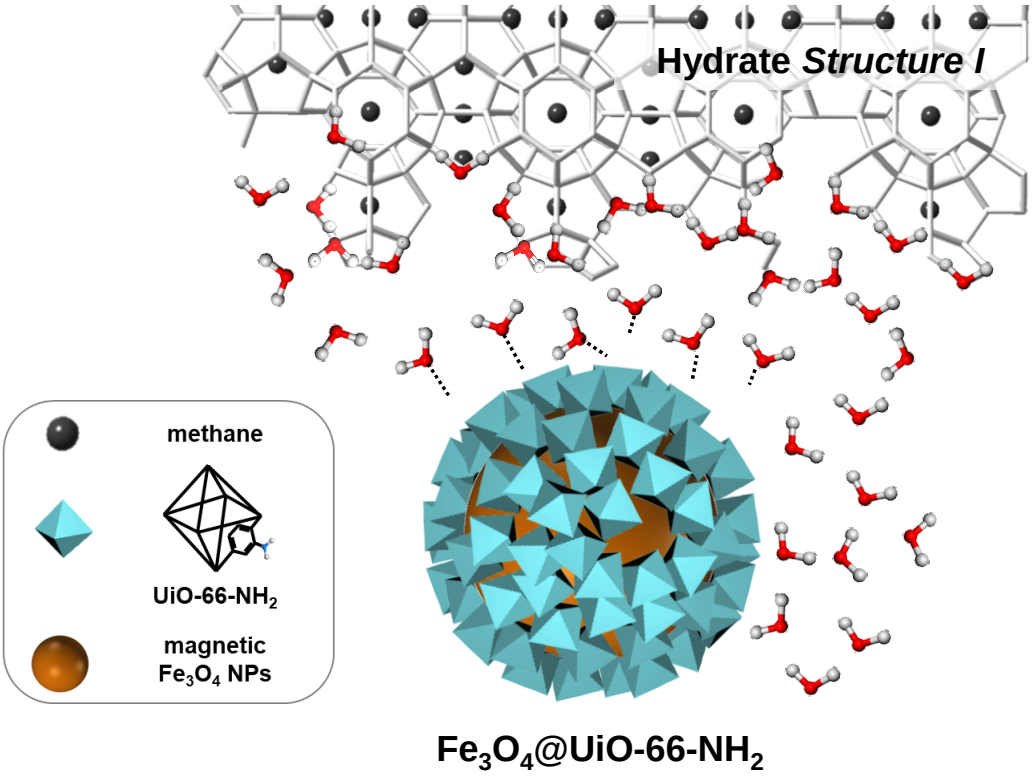

Figure 4.1.1. Schematic illustration of core–shell-type recoverable hydrate inhibitor Fe_3O_4@UiO-66-NH_2. The blue, red, white, and black balls represent nitrogen, oxygen, hydrogen, and methane, respectively. The dotted lines represent hydrogen bonds.

4.1.2. Synthesis of metal organic frameworks (MOFs)

All chemicals and solvents were of reagent grade and used without further purification. UiO-66 series, Fe_3O_4 nanoparticles, and Fe_3O_4@UiO-66-NH_2 were synthesized according to a modified literature procedure. [91-94]

Synthesis of UiO-66. $ZrCl_4$ (466 mg, 2 mmol) and terephthalic acid (320 mg, 2 mmol) were mixed with 200 mL DMF in a lab bottle (500 mL capacity) and then added 30 mL of acetic acid. The vial was sealed and placed in an oven at 120 °C for 24 h. After cooling down to RT, the yellow precipitates were obtained by centrifuge. After being washed with DMF, the solid was then washed with water and methanol. Finally, the UiO-66 nanocrystals were activated in vacuum at 150 °C for 6 h.

Synthesis of UiO-66 (200 nm). $ZrCl_4$ (466 mg, 2 mmol), terephthalic acid (320 mg, 2 mmol), and benzoic acid (3.66 g, 30 mmol) were mixed with 36 mL DMF in a vial (100 mL capacity) and then added 0.33 mL of 37% of HCl. The vial was sealed and placed in an oven at 120 °C for 48 h. After cooling down to RT, the white precipitates were obtained by centrifuge. After being washed with DMF, the solid was then washed with water and methanol. Finally, the UiO-66 nanocrystals were activated in vacuum at 150 °C for 6 h.

Synthesis of UiO-66-NH_2. $ZrCl_4$ (25.8 mg, 0.11 mmol) and 2-aminoterephthalic acid (14.5 mg, 0.08 mmol) were mixed with 10 mL DMF in a vial (20 mL capacity) and then added 1.372 mL of acetic acid. The vial was sealed and placed in an oven at 120 °C for 24 h. After cooling down to RT, the yellow precipitates were obtained by centrifuge. After being washed with DMF, the solid was then washed with water and methanol. Finally, the UiO-66-NH_2 nanocrystals were activated in vacuum at 150 °C for 6 h.

Synthesis of UiO-66-NH_2 (200 nm). $ZrCl_4$ (51.6 mg, 0.22 mmol) and 2-aminoterephthalic acid (14.5 mg, 0.08 mmol) were mixed with 10 mL DMF in a vial (20 mL capacity) and then added 1.372 mL of acetic acid. The vial was sealed and placed in an oven at 110 °C for 24 h. After cooling down to RT, the yellow precipitates were obtained by centrifuge. After being washed with DMF, the solid was then washed with water and methanol. Finally, the UiO-66-NH_2 (200 nm) nanocrystals were activated in vacuum at 150 °C for 6 h.

Synthesis of UiO-66-OH. $ZrCl_4$ (14.6 mg, 0.08 mmol) and 2-hydroxyterephthalic acid (25.8 mg, 0.11 mmol) were mixed with 10 mL DMF in a vial (20 mL capacity) and then added 1.4 mL of acetic acid. The vial was sealed and placed in an oven at 120 °C for 24 h. After cooling down to RT, the yellow precipitates were obtained by centrifuge. After being washed with DMF, the solid was then washed with water and methanol. Finally, the UiO-66-OH nanocrystals were activated in vacuum at 150 °C for 6 h.

Synthesis of Fe_3O_4 nanoparticles. 0.54 g of $FeCl_3 \cdot 6H_2O$ was completely dissolved in 20 mL of ethylene glycol to form a uniform solution under ultrasonic, Then, 0.192 g of polyacrylic acid, 1.5 mL of deionized water, and 1.2 g of urea were successively added. The mixture was ultrasonicated for 10 min and then sealed in a Teflon-lined stainless-steel autoclave (20 mL capacity). The autoclave was heated at 200 °C for 12 h and then allowed to cool to RT. The black products were washed several times with deionized water and ethanol to eliminate organic and inorganic impurities and collected by centrifugation at 7830 rpm for 10 min. Finally, the Fe_3O_4 nanoparticles were activated in vacuum at 150 °C for 6 h.

Synthesis of Fe_3O_4@UiO-66-NH_2. 25 mg of Fe_3O_4 nanoparticles were added to 10 mL of DMF and ultrasonicated for 30 min. Then, the obtained dispersion was added to a DMF solution of UiO-66-NH_2

precursors, which contained 37.5 mg of $ZrCl_4$ and 29 mg of NH_2-BDC and 9 mL of DMF. The resulting mixture was placed in a preheated oven at 80 °C for 12 h and then held at 100 °C for 24 h. After cooling down to RT, the resulting brown solid was washed several times with deionized water and ethanol and collected by centrifugation at 7830 rpm for 10 min. Finally, the Fe_3O_4@UiO-66-NH_2 were activated in vacuum at 150 °C for 6 h.

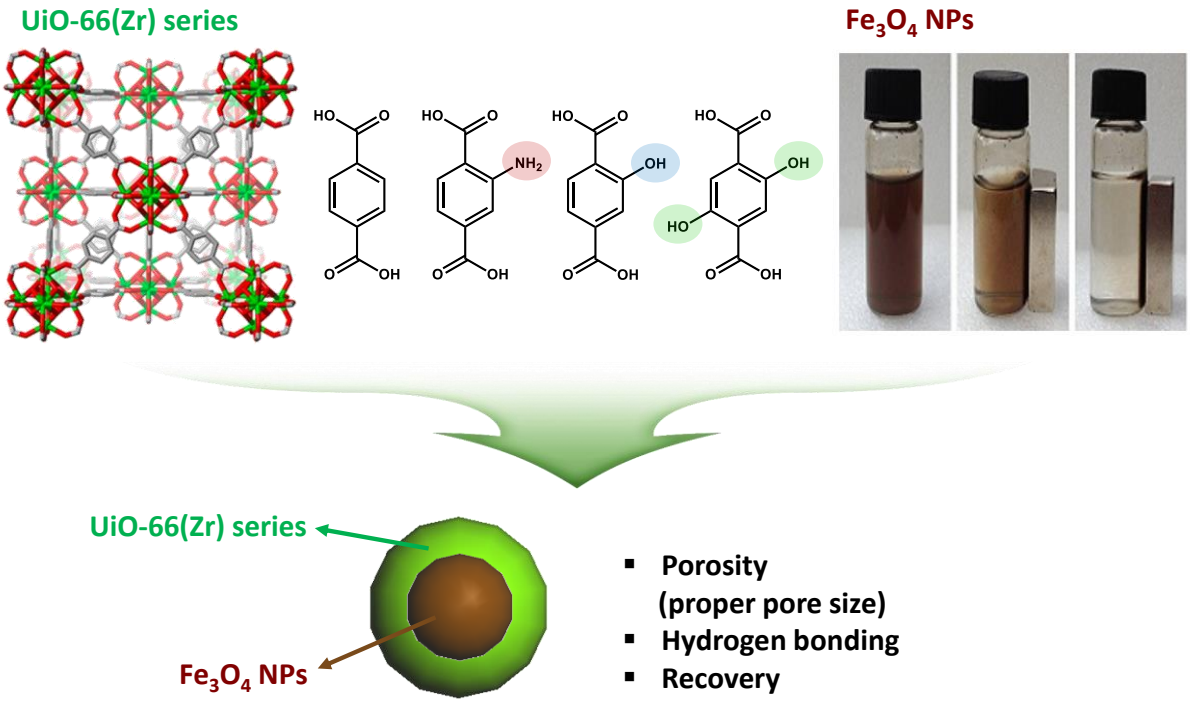

Figure 4.1.2. Synthesis of Metal Organic Framework (MOF).

4.1.3. Onset temperature measurements of CH_4 hydrate in the presence of MOF using the HP autoclave

To examine the functional group effect on hydrate inhibition, three UiO-66 derivatives (UiO-66, UiO-66-OH, and UiO-66-NH_2, ~600 nm) were prepared using terephthalic acid, 2-aminoterephthalic acid, and 2-hydroxyterephthalic acid, respectively. [91-93]. The structures of the UiO-66 series were confirmed by X-ray powder diffraction (XRPD), which indicated the formation of pure phases with identical structures. The Brunauer–Emmett–Teller (BET) surface area of UiO-66 was 880 m^2 g^{-1}, whereas despite being porous those of UiO-66-OH and UiO-66-NH_2 were slightly reduced to 752 and 817 m^2 g^{-1}, respectively, attributed to the occupancy of the functional groups in these porous materials. As the affinity of the MOFs for water molecules is the critical feature for hydrate inhibition, water vapor sorption experiments were performed. As shown in Figure 4.1.3 (a), while significant water uptake by UiO-66 occurred above ~0.4 relative humidity, water adsorption by UiO-66-OH and UiO-66-NH_2 began at a much lower relative humidity (P/P_o = 0.01). The α values, which are the relative humidities corresponding to half the total water uptake and describe the hydrophilicities of the materials, were calculated as 0.44, 0.29, and 0.25 for UiO-66, UiO-66-OH, and UiO-66-NH_2, respectively [95-97]. Thus, the introduction of hydroxyl and amine groups into UiO-66 increases the hydrophilicity. The effect of the UiO-66 materials as KHIs on CH_4 hydrate formation was studied by measuring the hydrate onset temperature (T_{onset}) using a specially designed equilibrium cell equipped with a resistance temperature detector sensor and a pressure transducer. T_{onset} is the temperature at which the gas hydrate is nucleated and starts to grow, and upon hydrate formation, an abrupt pressure drop is detected (Figure 4.1.3 (b)). A lower T_{onset} indicates better performance as an inhibitor. The pressure of a cell charged with 30 cm^3 water with or without 1 wt% inhibitor and pressurized to 10 MPa with CH_4 was monitored during cooling from 285.8 to 272.7 K at 0.02 K min^{-1}. As shown in Figures 4.1.3 (b) and (c), the T_{onset} of pure water is 284.5 K but the addition of UiO-66 significantly delayed CH_4 hydrate formation (T_{onset} = 281.7 K), with a kinetic inhibition effect comparable to that of the conventional KHI, PVP (T_{onset} = 281.1 K). Notably, introducing functional groups such as –OH and –NH_2 into UiO-66 lowered T_{onset} significantly (279.7 K for UiO-66-OH and 279.6 K for UiO-66-NH_2). This decrease was attributed to the enhanced hydrophilicity and increased strength of hydrogen bonding with water, which consequently inhibited the formation of CH_4 hydrate. The influence of the KHI particle size was also studied by comparing the performance of 200 and 600 nm UiO-66 and UiO-66-NH_2 particles, which for each MOF have similar surface areas, water adsorption capacities, and hydrophilicities. If the MOF external surface is entirely responsible for hydrate inhibition, the smaller MOF particles are expected to exhibit better inhibition performance. However, as shown in Figure 4.1.3 (d), the T_{onset} values of the MOFs with smaller (200 nm) and larger (600 nm) particles sizes are almost identical. As the MOF pores allow easy access for water molecules, as evidenced by the water adsorption measurements, the inner pore environment has a more significant impact on disrupting the hydrogen-bonded water molecular networks for gas hydrate

formation.

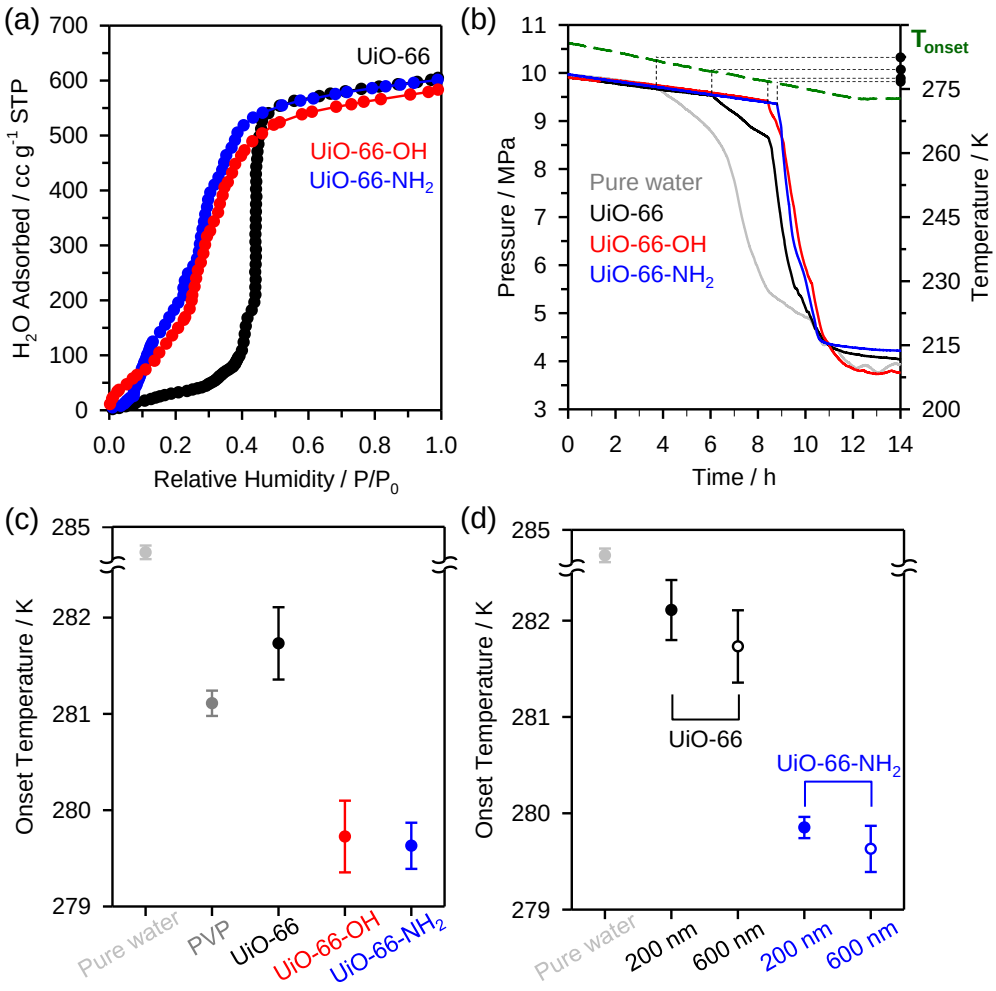

Figure 4.1.3. (a) Water adsorption isotherms of UiO-66, UiO-66-OH, and UiO-66-NH_2 at 298 K. (b) Detection of pressure drop upon hydrate formation for the UiO-66 series. (c) and (d) Hydrate onset tem-peratures in the presence of the UiO-66 series depending on func-tional groups and particle sizes

4.1.4. Cage-filling behavior of CH_4 hydrate in the presence of UIO-66-NH_2

The sI CH_4 hydrate is composed of two small cages of 5^{12} and six large cages of $5^{12}6^2$ in the unit cell (46 H_2O), in which one CH_4 molecule is enclathrated per cage. The CH_4 molecules enclathrated in the large $5^{12}6^2$ and small 5^{12} cages are distinguishable in the Raman spectra, appearing at 2905 and 2915 cm^{-1} (symmetric C−H stretching mode), respectively. Therefore, the cage-filling behavior of CH_4 hydrates in the presence of UiO-66-NH_2 was examined using *in situ* Raman spectroscopy to obtain further insights into the inhibition mechanism during hydrate nucleation and growth. The Raman spectra were collected in real time at 8 MPa and 275.9 K, which is 4 K lower than the hydrate equilibrium condition in order to induce CH_4 hydrate formation. For pure water, two distinct peaks corresponding to CH_4 in two different cages started to appear upon hydrate nucleation and continued to grow gradually until 150 min, when hydrate formation was completed (Figure 4.1.4 (a)). In contrast, in the presence of UiO-66-NH_2, the CH_4 hydrate growth behavior was different, with the peak for CH_4 in the large cages growing more rapidly than that for CH_4 in the small cages in the early stage of hydrate formation, and then, both peaks reached a plateau within 300 min (Figure 4.1.4 (b)). For the spectra obtained after the completion of hydrate formation, the area ratio of the peak for the large cages (A_L) to that for the small cages (A_S) was 2.75, which is much smaller than the value for the pure CH_4 hydrate (A_L/A_S = 3.12). This difference indicates that UiO-66-NH_2 significantly inhibited CH_4 hydrate growth after nucleation and, in particular, prevented CH_4 molecules from entering the large $5^{12}6^2$ cages, leaving the large $5^{12}6^2$ cages less populated.

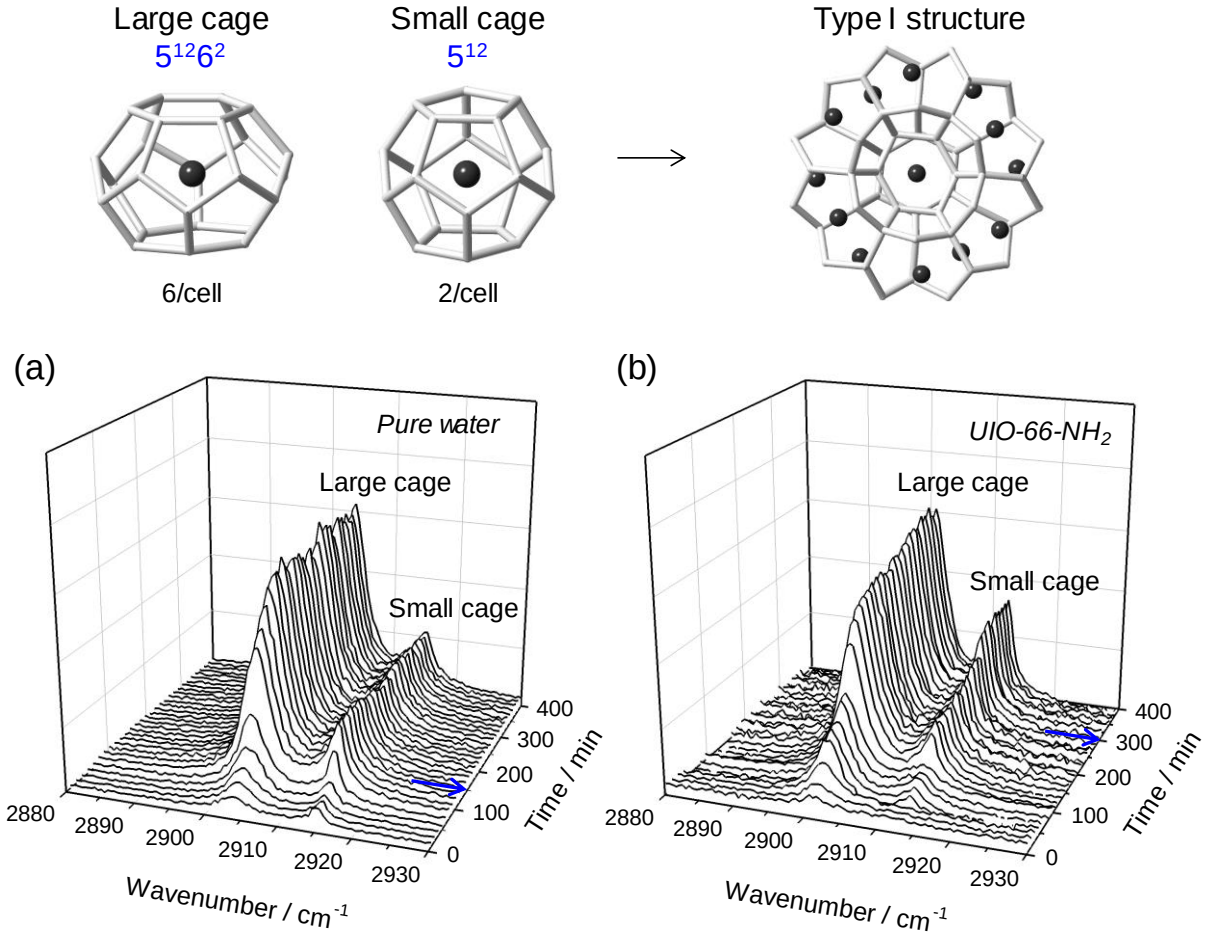

Figure 4.1.4. *In situ* Raman spectra of CH_4 hydrates for (a) pure water and (b) water in the presence of UiO-66-NH_2 at 8 MPa and 275.9 K.

4.1.5. Onset temperature measurements of CH_4 Hydrate in the presence of Fe_3O_4@UiO-66-NH_2

Composites of KHIs with magnetic species provide a facile model for recoverable KHIs. Herein, we adopted magnetic Fe_3O_4 NPs to construct core–shell-type MOF composites. The most promising KHI, UiO-66-NH_2, was chosen as the shell MOF, which was grown on 100 nm Fe_3O_4 NPs as a core through a solvothermal reaction (Figures 4.1.5 (a)) [94]. Energy-dispersive X-ray spectroscopy (EDS) elemental mapping of Fe and Zr (Figure 4.1.5 (b)) and XRPD patterns (Figure 4.1.5 (c)) verified the successful formation of a core–shell structure in the Fe_3O_4@UiO-66-NH_2 composite. The amount of Fe_3O_4 NPs in Fe_3O_4@UiO-66-NH_2 was 68 wt%, as confirmed by inductively coupled plasma-mass spectrometry. To determine the inhibition effect of the recoverable core–shell-type material on CH_4 hydrate, T_{onset} was measured using 1 wt% (based on UiO-66-NH_2) Fe_3O_4@UiO-66-NH_2 (Figure 4.1.5 (d)). In the presence of Fe_3O_4@UiO-66-NH_2, T_{onset} was similar to that using UiO-66-NH_2. As the Fe_3O_4 NP core does not have any effective functional groups for hydrate inhibition and is well covered by UiO-66-NH_2 crystals, the UiO-66-NH_2 shell inhibits CH_4 hydrate formation.

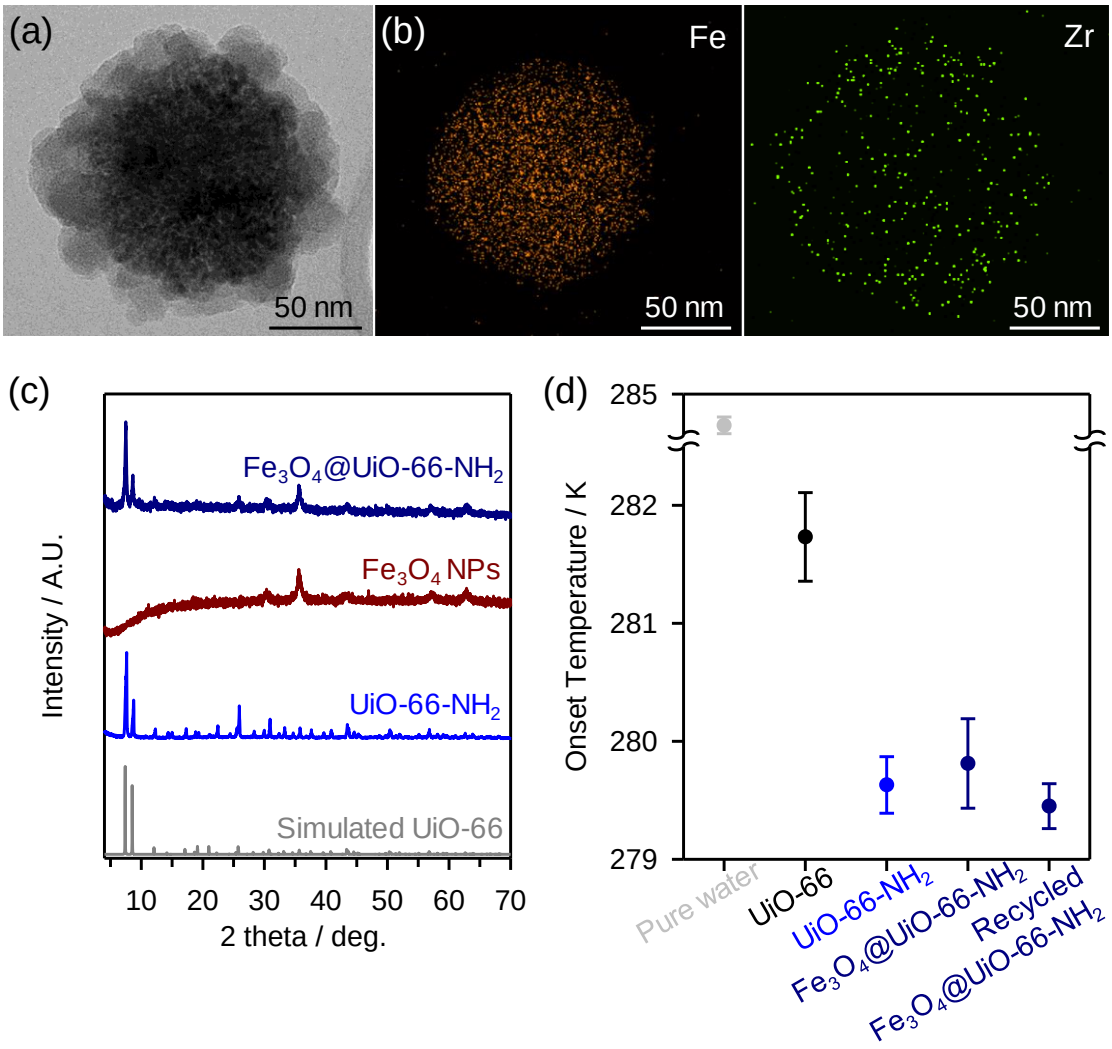

Figure 4.1.5. (a) TEM image of Fe_3O_4@UiO-66-NH_2 and (b) corresponding EDS mapping of Fe (orange) and Zr (green). (c) XRPD patterns of UiO-66-NH_2, Fe_3O_4 NPs, and core–shell-type Fe_3O_4@UiO-66-NH_2. (d) Hydrate onset temperatures of UiO-66-NH_2, Fe_3O_4@UiO-66-NH_2, and recycled Fe_3O_4@UiO-66-NH_2.

4.1.6. Recycling of core–shell-type Fe_3O_4@UiO-66-NH_2

As intended, the core–shell-type Fe_3O_4@UiO-66-NH_2 composite was easily separated from solution using a bar magnet after gas hydrate dissociation, as shown in Figures 4.1.6 (a) and (b), and the recovery of used inhibitors was 99.3%. The TEM image of recovered Fe_3O_4@UiO-66-NH_2 shows that the core–shell morphology was well maintained after the hydrate formation experiment (Figure 4.1.6 (c)), and also confirmed that no substances remained in water, indicating that the MOF shell on the Fe_3O_4 NPs was intact. To test the recyclability, T_{onset} was measured using recovered Fe_3O_4@UiO-66-NH_2. The inhibition performance of recovered Fe_3O_4@UiO-66-NH_2 was comparable (T_{onset} = 279.5 K) to that of UiO-66-NH_2 (279.6 K) and fresh Fe_3O_4@UiO-66-NH_2 (279.8 K).

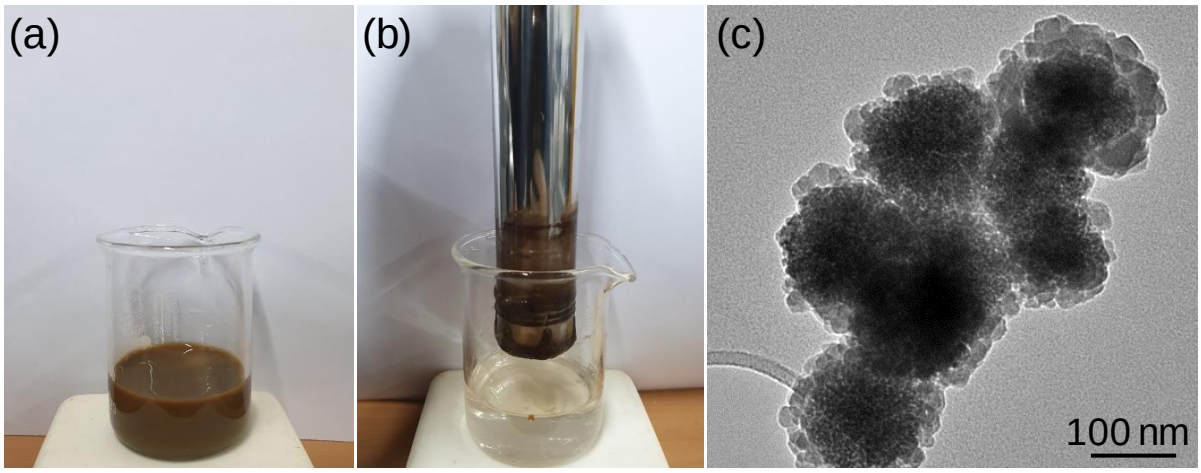

Figure 4.1.6. Images of (a) Fe_3O_4@UiO-66-NH_2 in solution and (b) Fe_3O_4@UiO-66-NH_2 separated from solution using a bar magnet. (c) TEM image of recovered Fe_3O_4@UiO-66-NH_2.

4.1.7. Conclusions

In this work, we suggested a new MOF-based class of KHIs that provides considerable inhibition of CH_4 hydrate formation with easy recoverability. The functional groups and particle sizes of the MOFs were controlled to understand the CH_4 hydrate inhibition mechanism. The introduction of functional groups such as –OH and $–NH_2$ to UiO-66 increased the hydrophilicity of the MOF material, which lowered the onset temperature for gas hydrate formation by disturbing the hydrogen bonding network between water molecules. In contrast, the particle size of UiO-66-NH_2 had little effect on the hydrate onset temperature. Moreover, time-dependent Raman spectra demonstrated that UiO-66-NH_2 had a unique cage-specific inhibition effect on the growth of CH_4 hydrate, effectively inhibiting CH_4 molecules from occupying the large $5^{12}6^2$ cages. We also designed a recoverable KHI by encapsulating Fe_3O_4 NPs within UiO-66-NH_2 shells. The Fe_3O_4@UiO-66-NH_2 composite was structurally and thermodynamically stable as well as easily recoverable, resulting in no deterioration of its inhibition performance after repeated use. We believe that these results for the MOF composite with Fe_3O_4 NPs as a KHI will provide novel insights into recoverable gas hydrate inhibitors that can address the environmental issues associated with subsea flow lines and contribute to broadening the field of MOF-based applications.

4.2. Experimental and Computational Investigation of Deep Eutectic Solvent (DES) as THI

This chapter includes the published contents:

Lee D, Go W, Oh J, Lee J, Jo I, Kim KS, Seo Y. Thermodynamic inhibition effects of an ionic liquid (choline chloride), a naturally derived substance (urea), and their mixture (deep eutectic solvent) on CH_4 hydrates. Chem Eng J 2020;125830. Reproduced with permission.

4.2.1. Abstract

In this study, the thermodynamic inhibition effects of choline chloride (ChCl, a hydrogen bond acceptor), urea (a hydrogen bond donor), and their mixture (deep eutectic solvent, DES) on CH_4 hydrates were investigated with both experimental and computational approaches. The synthesis of DES from the mixture of ChCl and urea was confirmed by measuring its melting temperature (285.7 K) through a high-pressure micro-differential scanning calorimeter. Sigma (σ)-profiles of ChCl, urea, and DES obtained by the COSMO-RS software indicated that these substances have great potential to be used as thermodynamic hydrate inhibitors (THIs). The three-phase (gas hydrate (H) – liquid water (L_w) – vapor (V)) equilibria of CH_4 hydrates in the presence of ChCl (1.0, 3.0, and 5.0 mol%), urea (1.0, 3.0, and 5.0 mol%), and DES (3.0 mol%) demonstrated that ChCl, urea, and DES contributed to the significant shift of hydrate equilibrium temperature to inhibition regions at a specified pressure and thus can function as effective THIs. Moreover, quantum theory of atoms in molecules (QTAIM) analysis also demonstrated that the strength of hydrogen bonding between inhibitor molecules and hydrate cages (small 5^{12} and large $5^{12}6^2$ cages) of CH_4 hydrates was in the order of ChCl > DES > urea, which was consistent with experimental results. The experimental and computational results from this study would be helpful for a better understanding of the inhibition mechanism of ChCl, urea, and DES and for their possible application to flow assurance in oil and gas pipelines.

4.2.2. Melting point measurement of DES

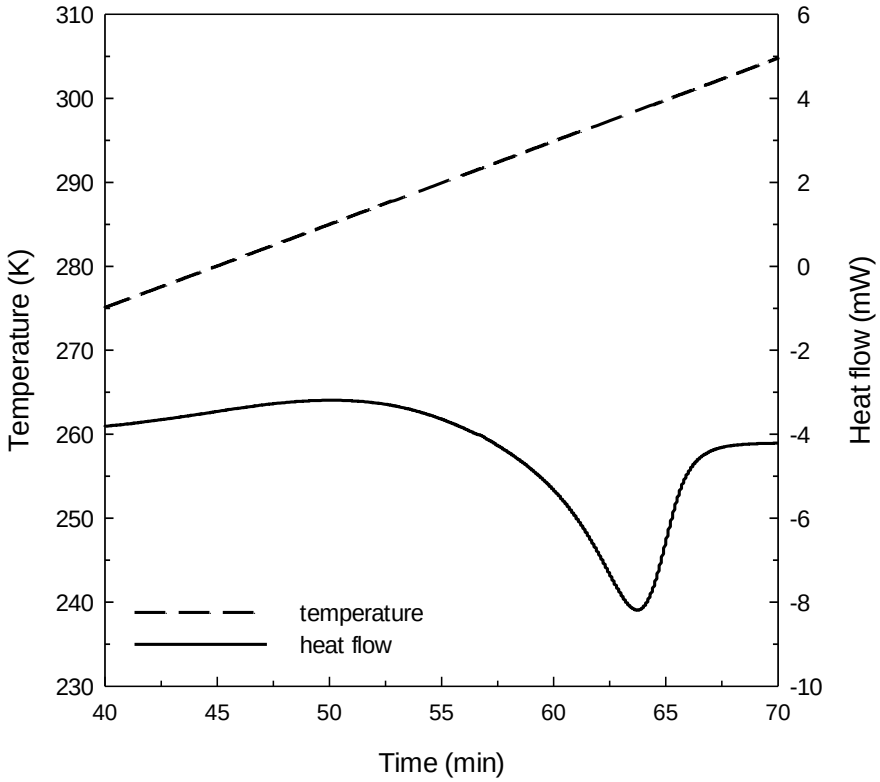

Figure 4.2.1. Heat flow curve of the synthesized DES.

A HP μ-DSC can be effectively used to monitor changes in heat flow during a phase transition of a certain substance [98-99]. The phase transition can be detected by the appearance of endothermic or exothermic peaks from heat flow curves. The DES formed from ChCl and urea is expected to have a lower melting temperature than that of ChCl (575 K) and that of urea (406 K). Figure 4.2.1 demonstrates the heat flow curve of the synthesized DES between 275.2 K and 305.2 K. From the drastic change in the slope of the heat flow curve, the DES was found to start to melt at around 285 K, which was in agreement with the value in prior literature [100], indicating that the DES composed of ChCl and urea was successfully and properly synthesized.

4.2.3. Sigma profiles of potential inhibitors

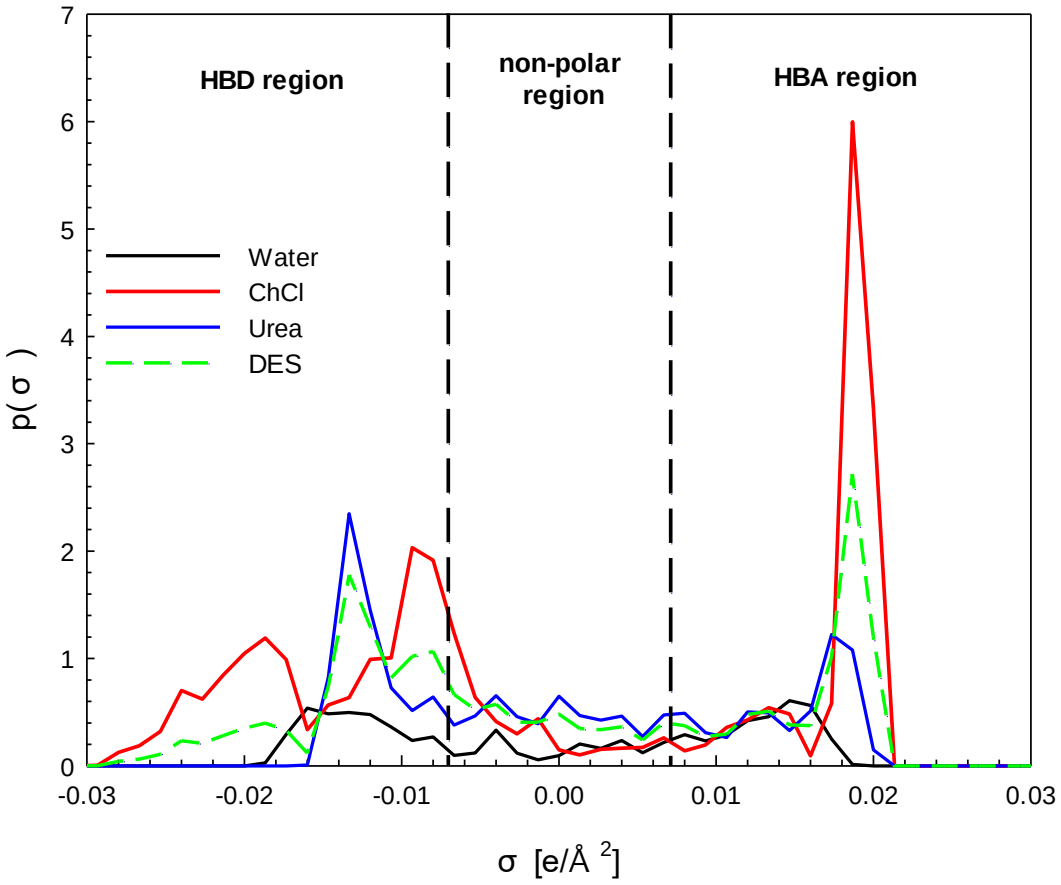

Figure 4.2.2. σ- profiles of ChCl, urea, DES, and water in polar and non-polar regions.

Figure 4.2.2 shows the σ-profiles of ChCl, urea, DES, and water in polar and non-polar regions. The two dotted perpendicular lines located at σ = -0.079 e/Å^2 and 0.079 e/Å^2 represent boundaries between a non-polar region and two polar (HBD and HBA) regions. A substance that has marked peaks in the range of -0.03 < σ < -0.079 e/Å^2 or in the range of 0.079 < σ < 0.03 e/Å^2 is thought to have considerable potential to act as a HBD or a HBA, respectively, and to have strong interactions with water [101]. Urea is a standard HBD, whereas ChCl is a well-known HBA [102]. Therefore, urea had a high peak of p(σ) in the HBD region (-0.03 < σ < -0.079 e/Å^2), whereas ChCl had a strong peak of p(σ) in the HBA region (0.079 < σ < 0.03 e/Å^2). However, the σ-profile pattern of the DES was fairly different from that of each substance (urea and ChCl). Unlike urea and ChCl, the DES showed pronounced peaks in both HBD (-0.03 < σ < -0.079 e/Å^2) and HBA (0.079 < σ < 0.03 e/Å^2) regions, and its σ-profile pattern was similar

to that of water, which implies a strong affinity between DES and water. The σ-profiles of the substances offered by COSMO-RS indicate that ChCl, urea, and DES have strong potential as gas hydrate inhibitors.

4.2.4. Influence of inhibitors on thermodynamic stability of CH_4 hydrates

The three-phase equilibria (H – L_w – V) of the CH_4 + inhibitor (1.0, 3.0. and 5.0 mol%) + water mixtures measured using a high-pressure autoclave are presented in Figure 4.2.3 and Table 4.2.1. As seen in Figure 4.2.3 (a) and (b), the equilibrium curves of the CH_4 + ChCl and CH_4 + urea hydrates shifted to inhibition regions, which are represented by higher pressure and lower temperature depending on the inhibitor concentration, compared to CH_4 hydrate. It can be seen from Figure 4.2.3 (c) that when 3.0 mol% of THIs were added, both ChCl and urea functioned as effective THIs even though ChCl was a stronger THI for CH_4 hydrate than urea was. ChCl is a kind of ionic liquid that disrupts hydrogen bonds of host water frameworks, and urea has two types of functional groups (-NH_2 and -C=O), which have the potential to form hydrogen bonds with host water molecules, leading to the requirement of higher pressure and lower temperature conditions to maintain the hydrate lattice structures. In this manner, the addition of ChCl and urea resulted in the shift of H–L_w–V equilibrium curves to harsher conditions. The equilibrium curve of the CH_4 + DES hydrate was located between that of the CH_4 + ChCl hydrate and that of the CH_4 + urea hydrate, which indicates that DES also acted as an effective THI.

To examine the inhibition effects of each inhibitor accurately, the equilibrium temperature shifts at 8.0 MPa– i.e., the difference in equilibrium temperatures between CH_4 hydrate and CH_4 + inhibitor (3.0 mol%) hydrates at 8.0 MPa–are depicted in Figure 4.2.4. As estimated by COSMO-RS in Figure 4.2.2 and also as expected from Figure 4.2.3, all substances (ChCl, urea, and DES) used in this study contributed to significant shift of the equilibrium curve of the CH_4 hydrate to inhibition regions, indicating that all three substances functioned as powerful THIs for CH_4 hydrates. ChCl was found to be the best THI among those used in this study. The inhibition performance of DES was slightly higher than that of urea, which was comparable to that of methanol.

Methanol is the most widely used THI in oil and gas pipelines, and there have been many studies on THI candidates with better thermodynamic inhibition effects, less environmental impact, and easier recoverability as compared to methanol [21]. However, due to the cheapness and effectiveness of methanol as a THI, appropriate and competitive candidates that can beat methanol have not yet been found [36, 81, 103-106]. However, experimental results demonstrated that ChCl, urea, and DES have great advantages as THIs because they have strong thermodynamic inhibition effects (ChCl), eco-friendly characteristics (urea), and excellent physical properties (DES). Despite these advantages, further research on the recovery of ChCl, urea, and DES after use should be performed because of their high solubility in water.

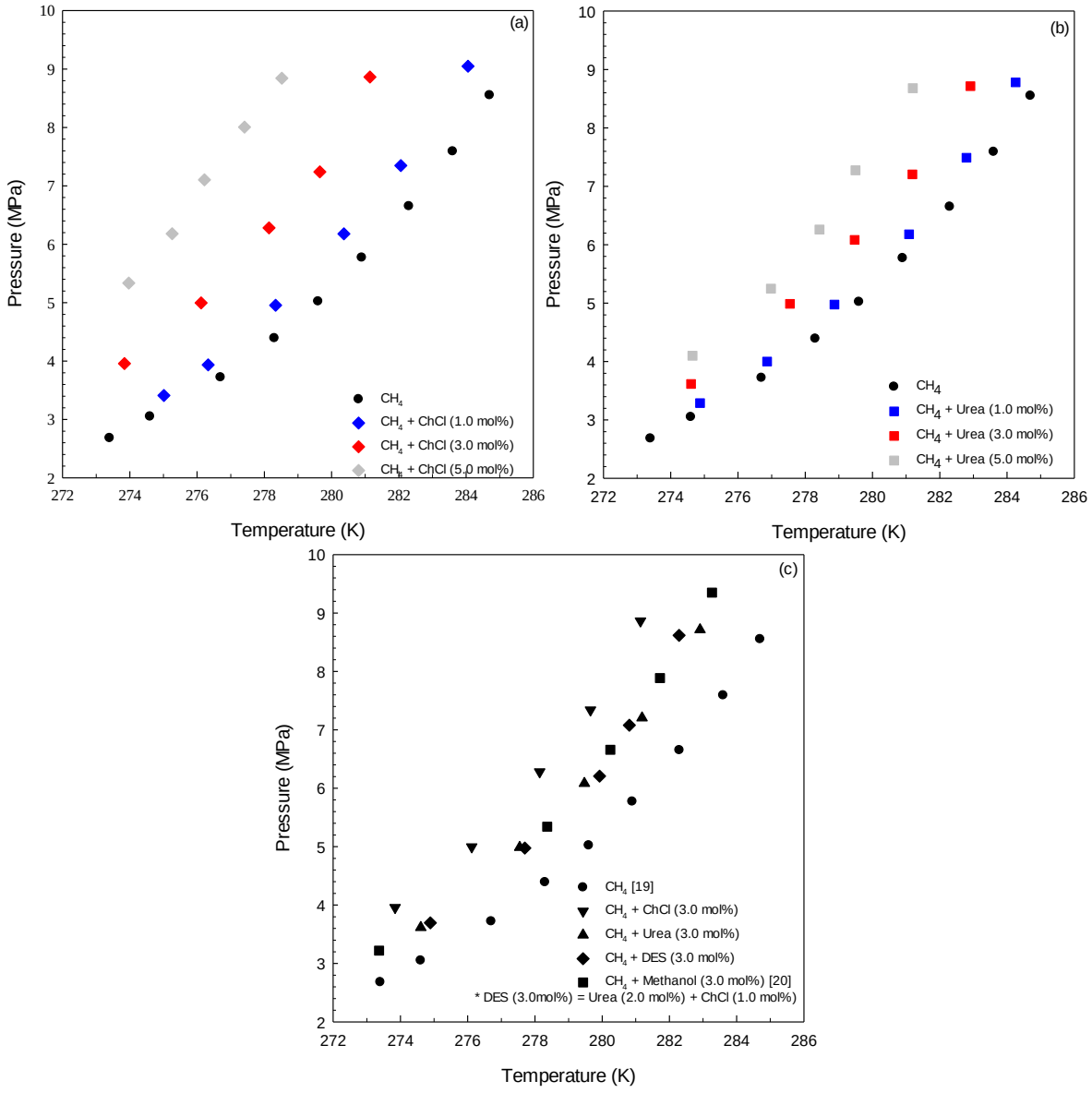

Figure 4.2.3. Phase equilibria of CH_4 hydrates in the presence of (a) ChCl (1.0, 3.0, and 5.0 mol%), (b) urea (1.0, 3.0, and 5.0 mol%), and (c) ChCl (3.0 mol%), urea (3.0 mol%), and DES (3.0 mol%) [78].

Table 4.2.1. Hydrate phase equilibrium data of the CH_4 + inhibitor (1.0, 3.0, 5.0 mol%) + water systems.[b]

[b] Standard uncertainties *u* are *u*(T) = 0.1 K and *u*(P) = 0.02 MPa.

ChCl						**Urea**						**DES**	
1.0 mol% (6.3 wt%)		3.0 mol% (17.0 wt%)		5.0 mol% (25.9 wt%)		1.0 mol% (3.3 wt%)		3.0 mol% (9.4 wt%)		5.0 mol% (14.9 wt%)		3.0 mol% (11.8 wt%)	
T (K)	P (MPa)	T (K)	P (MPa)	T(K)	P (MPa)	T(K)	P (MPa)	T(K)	P (MPa)	T (K)	P(MPa)	T(K)	P (MPa)
275.0	3.41	273.8	3.96	274.0	5.34	274.9	3.29	274.6	3.62	274.6	4.10	274.9	3.70
276.3	3.94	276.1	5.00	275.3	6.18	276.9	4.00	277.5	4.99	277	5.25	277.7	4.98
278.3	4.96	278.1	6.28	276.2	7.10	278.9	4.98	279.5	6.08	278.4	6.26	279.9	6.21
280.4	6.18	279.7	7.24	277.4	8.01	281.1	6.18	281.2	7.21	279.5	7.28	280.8	7.08
282.1	7.35	281.1	8.86	278.5	8.84	282.8	7.49	282.9	8.71	281.2	8.68	282.2	8.61
284.1	9.05					284.3	8.78						

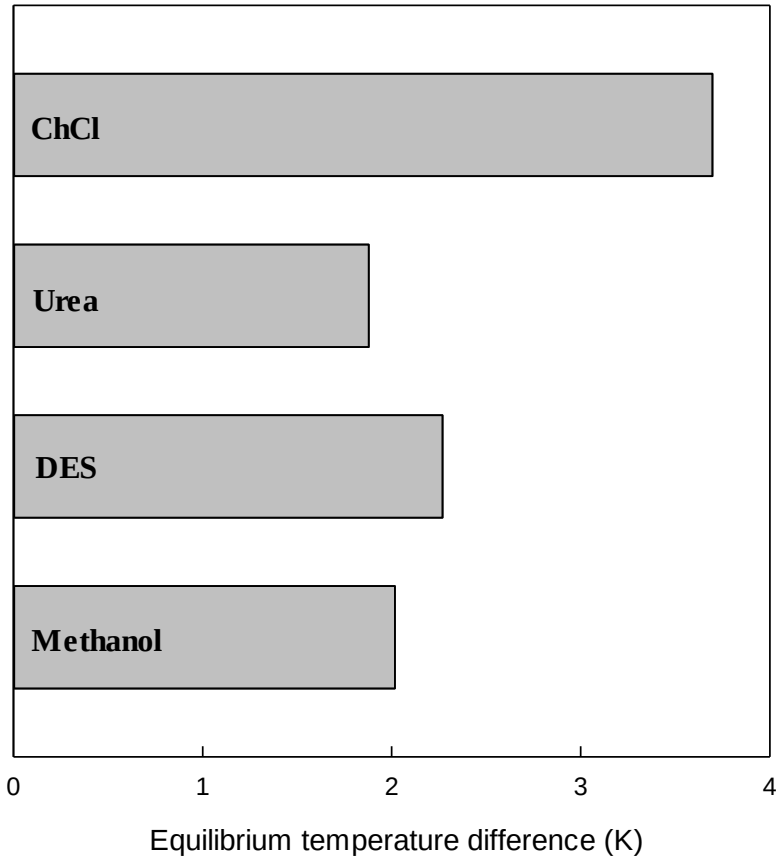

Figure 4.2.4. Equilibrium temperature difference between CH_4 hydrate and CH_4 + inhibitor (3.0 mol%) hydrates at 8.0 MPa [81].

4.2.5. QTAIM (Quantum Theory of Atoms in Molecules) approaches

QTAIM analysis accompanied by optimization of molecules is very helpful in investigating the characteristics of substances more in detail. In this study, QTAIM analysis was used to find all BCPs and the semi-empirical PM6 method was applied to optimize geometric structures of hydrate cages and inhibitor molecules as shown in Figure 6. Every noticeable (3, -1) point marked as yellow-colored dots was located on the place where the hydrogen bond occurs. Notably, it is vital to check critical points between hydrate cages and attached substance molecules in order to estimate the performance of these substances as THIs. By sorting these spots out, their electron density (ρ), Laplacian of electron density ($\nabla^2\rho$), potential energy density at BCP (V(r)), and hydrogen bond energy (E_{HB}) data could be obtained; these results are listed in Table 4.2.2. It is known from QTAIM studies that the values of ρ and $\nabla^2\rho$ are highly related to bonding strength, and V(r) values are linked to the E_{HB} data [107, 108]. By examining these physical properties of BCPs, it was possible to estimate the performance of THIs (ChCl, urea, and DES) from the perspective of quantum theory. For this purpose, the linear relationship between E_{HB} and ρ values was demonstrated by plots of E_{HB} versus ρ shown in Figure 4.2.6. Calculated E_{HB} values were plotted with respect to ρ values and linearly fitted using equation (2). All parameters of linear fitting (A, B, and R-square values), depending on the types of inhibitors attached to the built hydrate cages, are individually given in Table 4.2.3.

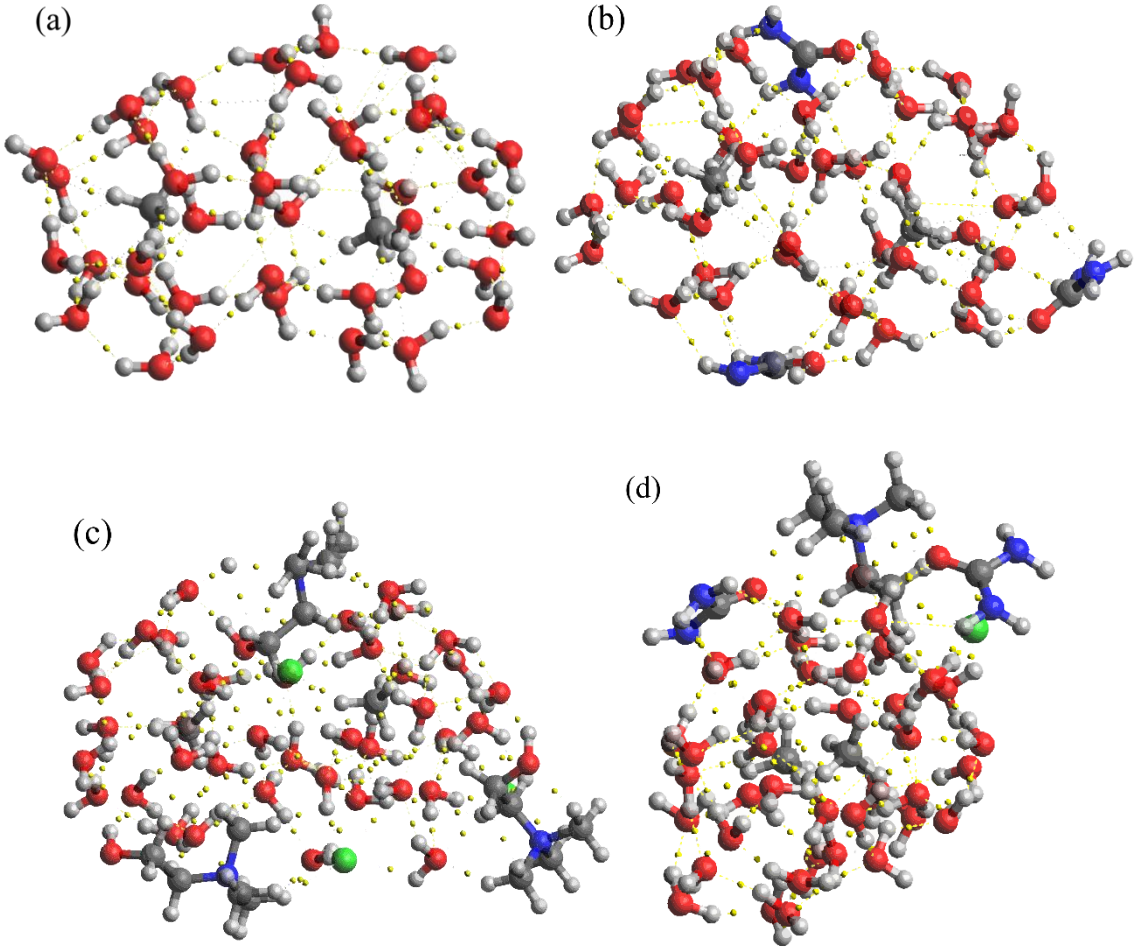

Figure 4.2.5. Geometric structures and discovered (3, -1) BCPs of (a) sI (5^{12} + $5^{12}6^2$ cages), (b) sI (5^{12} + $5^{12}6^2$ cages) + urea, (c) sI (5^{12} + $5^{12}6^2$ cages) + ChCl and (d) sI (5^{12} + $5^{12}6^2$ cages) + DES, discovered with QTAIM analysis.

Table 4.2.2. Physical properties of (3, -1) BCPs discovered for different types of inhibitors.

Inhibitor Type	BCP #	Electron Charge Density (ρ) [e Å^{-3}]	Laplacian of Electron Charge Density ($\nabla^2\rho$) [e Å^{-5}]	Potential Energy (V(r)) [kJ/mol]	Hydrogen Bond Energy (E_{HB}) [kJ/mol]
sI (5^{12} + $5^{12}6^2$ cages) + urea	1	0.019	0.098	-47.78	-23.89
	2	0.015	0.087	-36.78	-18.39
	3	0.018	0.091	-44.03	-22.01
	4	0.018	0.094	-45.11	-22.56
	5	0.018	0.095	-43.54	-21.77
	6	0.012	0.075	-29.57	-14.79
	7	0.014	0.089	-35.25	-17.63
	8	0.022	0.108	-55.66	-27.83
	9	0.036	0.167	-96.62	-48.31
	10	0.030	0.151	-82.44	-41.22
	11	0.026	0.133	-69.84	-34.92
sI (5^{12} + $5^{12}6^2$ cages) + ChCl	12	0.014	0.072	-29.57	-14.79
	13	0.011	0.057	-20.86	-10.43
	14	0.008	0.042	-14.20	-7.10
	15	0.081	0.183	-196.01	-98.00
	16	0.022	0.090	-49.28	-24.64
	17	0.014	0.078	-31.50	-15.75
	18	0.015	0.079	-33.59	-16.79
	19	0.010	0.068	-24.67	-12.34
	20	0.016	0.067	-33.04	-16.52
	21	0.087	0.170	-204.97	-102.49
	22	0.012	0.067	-26.19	-13.09
	23	0.011	0.067	-24.60	-12.30
	24	0.037	0.145	-87.01	-43.50
	25	0.042	0.167	-99.97	-49.99
	26	0.065	0.244	-143.82	-71.91

sI (5^{12} + $5^{12}6^2$ cages) + DES	27	0.009	0.059	-21.17	-10.59
	28	0.012	0.071	-27.85	-13.92
	29	0.023	0.105	-55.62	-27.81
	30	0.018	0.095	-44.19	-22.09
	31	0.013	0.067	-27.98	-13.99
	32	0.079	0.173	-186.52	-93.26
	33	0.012	0.061	-24.68	-12.34
	34	0.051	0.003	-6.81	-3.41
	35	0.035	0.002	-4.94	-2.47
	36	0.024	0.003	-8.28	-4.14

Table 4.2.3. Parameters of linear fitting for the equation $E_{HB} = A\rho + B$ (E_{HB} [kJ/mol] versus ρ [e Å^{-3}]) at discovered BCPs.

Inhibitor Type	A/kJ mol^{-1} [e Å^{-3}]$^{-1}$	B/kJ mol^{-1}	R^2
sI (5^{12} + $5^{12}6^2$ cages) + urea	-1431.59	3.07	0.9951
sI (5^{12} + $5^{12}6^2$ cages) + ChCl	-1198.85	1.47	0.9972
sI (5^{12} + $5^{12}6^2$ cages) + DES	-1177.25	-0.44	0.9949

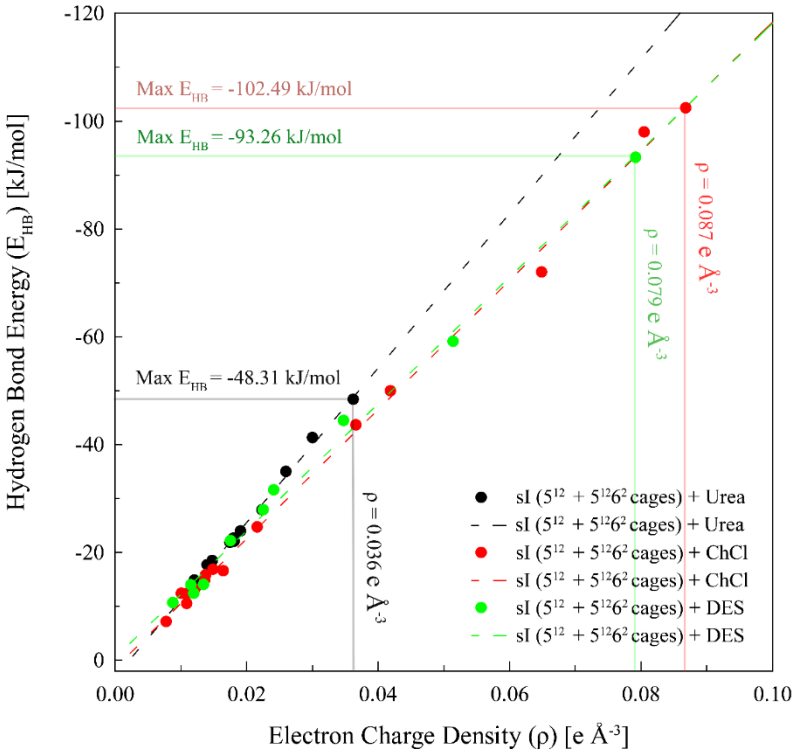

Figure 4.2.6. Plots of E_{HB} versus ρ in the discovered BCPs between sI (5^{12} + $5^{12}6^2$ cages) and inhibitor substances. Their maximum E_{HB} values were marked as horizontal lines.

In Figure 4.2.6, ρ distributions of inhibitor substances and their maximum E_{HB} values illustrate the inhibition performance of ChCl, urea, and DES as THIs toward the CH_4 hydrate cages. The black-colored dots (denoting urea) were located in the lowest E_{HB} value regions (in terms of absolute value of E_{HB}) with the narrowest E_{HB} distribution, which can be linked to the weak thermodynamic inhibition effect of urea. In contrast, the red-colored dots (denoting ChCl) showed the widest and broadest E_{HB} distribution and had the largest maximum E_{HB} value (-102.49 kJ/mol, in terms of absolute value of E_{HB}), which is highly related to the excellent thermodynamic inhibition effect of ChCl. The green-colored dots (denoting DES) showed quite wide E_{HB} distribution and high E_{HB} values (in terms of absolute value of E_{HB}), but not as much as the red-colored dots (denoting ChCl). It should be noted that the maximum E_{HB} value of each substance is a good indicator for estimating and evaluating the performance of each substance as a THI [109]. The results from ρ distributions and maximum E_{HB} values of substances clearly demonstrate that QTAIM analysis of the potential THI substances could validate and support

the experimental results of the THI performance for CH_4 hydrates. From these experimental and computational results, ChCl, urea, and their mixture (DES) were found to act as effective THIs for CH_4 hydrates. ChCl, a cheap ionic liquid, was the most powerful THI among them. The inhibition performance of urea, a naturally derived substance, was not better than that of ChCl and DES. Although the thermodynamic inhibition effect of DES was not superior to that of ChCl, judging from its various advantages such as liquid phase at room temperature, low toxicity, biodegradability, and negligible vapor pressure, DES is a good candidate as a potential THI for CH_4 hydrate. The performance of ChCl, urea, and DES as kinetic hydrate inhibitors (KHIs) should be also investigated for a better understanding of their inhibition mechanism and for further applications of these substances to flow assurance in oil and gas pipelines.

4.2.6. Conclusions

In this study, the thermodynamic inhibition effects of ChCl, urea, and their mixture (DES) on CH_4 hydrates were examined with both experimental and computational approaches. The formation of DES from ChCl and urea was confirmed by measuring its melting point (285.7 K) through a HP μ-DSC. The COSMO-RS software was effectively used to pre-screen potential THIs by providing σ-profiles of substances. ChCl showed a strong peak of p(σ) in the HBA region, whereas urea exhibited a high peak of p(σ) in the HBD region. DES showed both peaks in the HBA and HBD regions, which was a similar σ-profile pattern to water molecules. The p(σ) patterns of ChCl, urea, and DES implied that these substances had great potential to be used as THIs. The addition of ChCl, urea, and DES resulted in the significant shift of equilibrium curve of CH_4 hydrates to inhibition regions, indicating that they effectively acted as THIs for CH_4 hydrates. ChCl showed the most powerful inhibition effect as a THI, and the inhibition performance of DES was slightly higher than that of urea, which was comparable to that of methanol. Physical properties of (3, -1) BCPs between CH_4 hydrate cages and THI substances were obtained by the QTAIM method. These physical properties were used to obtain ρ distributions and maximum E_{HB} values of potential THI substances, which were effectively utilized to validate and support the experimental results of the THI performance for CH_4 hydrates. The overall experimental and computational results indicate that ChCl, urea, and DES have great potential as THIs because ChCl is a cheap ionic liquid with the best THI performance, urea is a naturally derived substance, and DES has several advantageous properties as a THI. Furthermore, ChCl, urea, and DES are also expected to have the potential to be used as KHIs, and thus further research on their KHI performance needs to be conducted in the near future for a better understanding of their inhibition mechanism and their real application to flow assurance in oil and gas pipelines.

4.3. High Sub-cooling Kinetic Hydrate Inhibitor: Fused Aromatic Networks (FANs)

This topic is currently in progress:

Lee D, Go W, Noh HJ, Baek JB, Seo Y. High Sub-cooling Kinetic Hydrate Inhibitor: Fused Aromatic Networks (FANs). In progress

---

4.3.1. Abstract

Recently, numerous fused aromatic network (FAN) structures are attracting considerable interest in the scientific community due to their intriguing electronic properties and superior physiochemical stability coming from a fully fused aromatic system. As unique FAN materials, three-dimensional (3D) cage-like organic network (3D-CON) structure and vertical two-dimensional (2D) layered ladder structure (designated as V2D-BBL structure) have been prepared as gas hydrate inhibitor materials. The resulting V2D-BBL structure has shown remarkable performances as gas hydrate inhibitors in both methane (onset: 277.5 K) and carbon dioxide (onset: 271.5 K), which are comparable to conventional one-dimensional polymer, poly (N-vinyl caprolactam) (PVCap). To investigate the inhibition performance, the IR, Raman, and surface area were measured the wavenumber shift, cage-specific inhibition effect, and hydrophilicity of each inhibitor. The V2D-BBL shows remarkable wavenumber shift and inhibits the large-cage growth. Furthermore, prepared FAN structures exhibit lower chemical oxygen demand (COD) and biological oxygen demand (BOD) values compared to PVCap, indicating better biodegradability, which is very important for practical use. Given the designability and stable structural nature, the V2D-BBL structure provides huge potential to design ideal gas hydrate inhibitor materials.

4.3.2. Synthesis of fused aromatic networks (FANs)

The 3D-CON and V2D-BBL structure were synthesized by the following procedures. The 3D-CON was obtained from the reaction between triptycene hexamine (THA) hexahydrochloride and hexaketocyclohexane (HKH) octahydrate in the reaction solvent (ethylene glycol and acetic acid) at 120 ℃. The V2D-BBL structure was prepared from a polycondensation reaction between THA and naphthalenetetracarboxylic dianhydride (NDA) in polyphosphoric acid (PPA) media. The resulting 3D-CON and V2D-BBL structures can be seen in Figure 4.3.1. The 3D-CON is constructed by stable fused aromatic pyrazine rings. The V2D-BBL structure has vertically oriented building blocks, which composed of poly(benzimidazobenzophenanthroline), or BBL polymer.

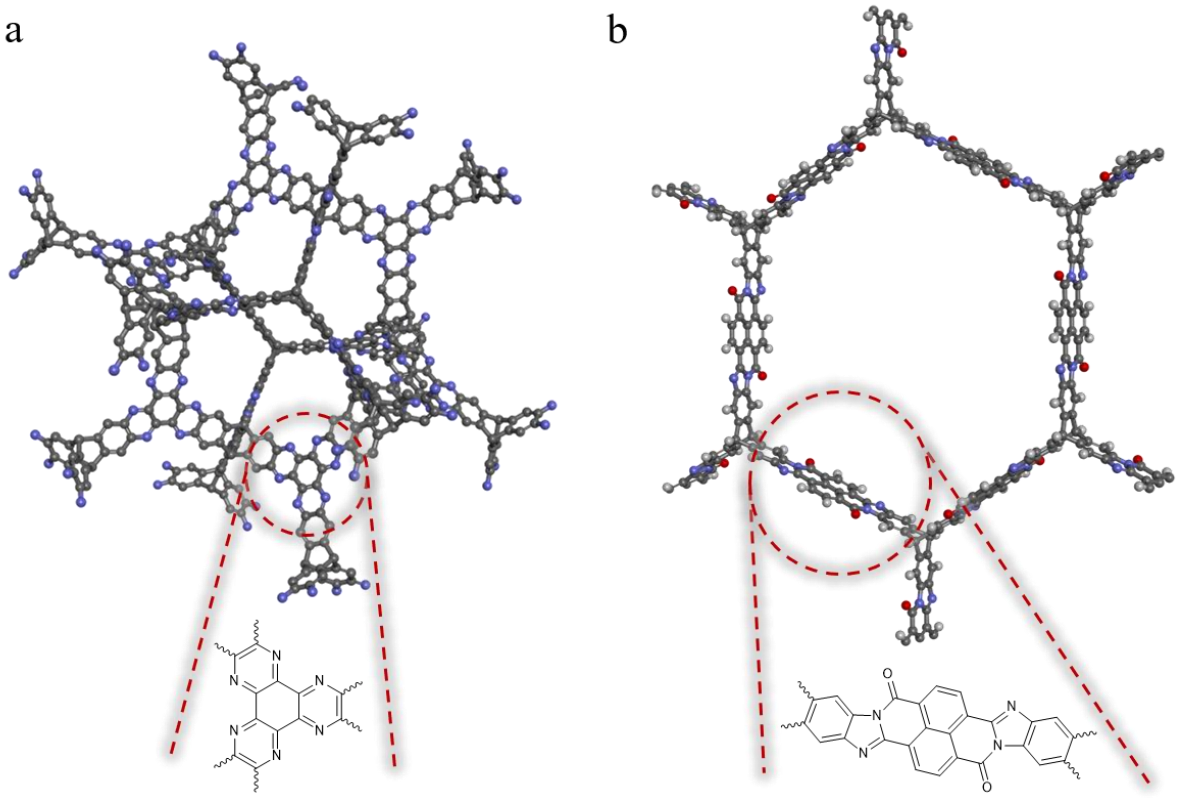

Figure 4.3.1. Illustration of fused aromatic network structures. **a**) 3D-CON composed of pyrazine rings. **b**) V2D-BBL structure.

4.3.3. Characterization of the 3D-CON and V2D-BBL structures

To confirm the structural formation of pyrazine ring in 3D-CON and benzimidazole rings and pyrrolidinone moieties in V2D-BBL structure, Fourier-transform infrared (FT-IR) and solid-state ^{13}C cross-polarization magic-angle spinning (MAS) nuclear magnetic resonance (NMR) spectroscopy were examined in Figure 4.3.2. The FT-IR spectrum of V2D-BBL structure exhibited C-N-C moiety peak (1378 cm^{-1}) and C=N bonds (1626 cm^{-1}) in benzimidazole ring (Figure 4.3.1.). Furthermore, appearance peak 1701 cm^{-1} indicates formation of carbonyl (C=O) bonds in pyrrolidone moiety. The formation of pyrazine ring could be confirmed by appearance of peaks at 1353, 1458 and 1616 cm^{-1} in FT-IR spectrum of 3D-CON (Figure 4.3.1)

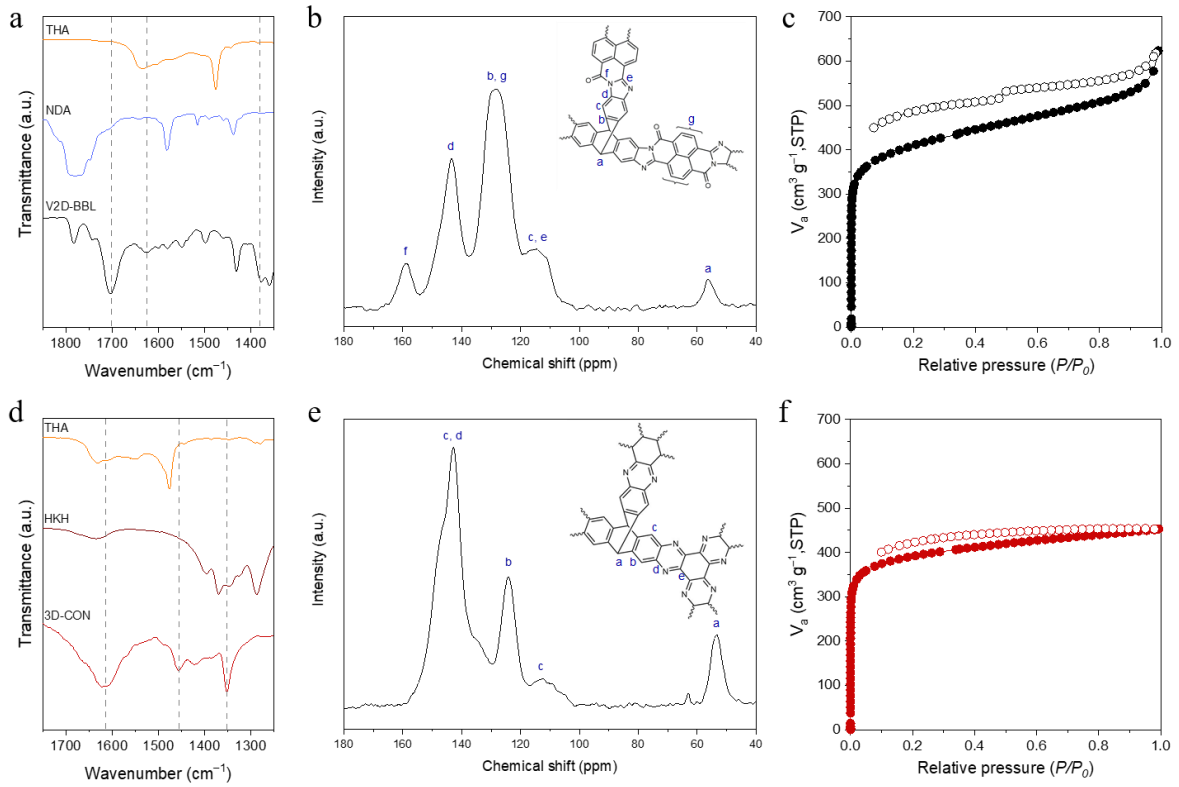

Figure 4.3.2. Characterization of the 3D-CON and V2D-BBL structures. a) FTIR spectra (KBr pellets) of THA (orange line), NDA (Pale blue line) and V2D-BBL structure (black line). Spectra were magnified in the range of 1350−1850 cm^{-1}, highlighting the formation of benzimidazole. b) Solid-state ^{13}C CP-MAS NMR spectrum of V2D-BBL structure. c) N_2 adsorption-desorption isotherm of V2D-BBL structure measured at 77 K and 1 bar. d) FTIR spectra (KBr pellets) of THA (orange line), HKH (wine line) and 3D-CON (Red line). Spectra were magnified in the range of 1250−1750 cm^{-1},

highlighting the formation of pyrazine ring. e) Solid-state ^{13}C CP-MAS NMR spectrum of 3D-CON. f) N_2 adsorption-desorption isotherm of 3D-CON obtained at 77 K and 1 bar.

The porosities of the 3D-CON and V2D-BBL structure were studied by nitrogen adsorption-desorption isotherms measured at 77 K and 1 bar. Both materials exhibited steep nitrogen uptake in the low-pressure range (0−0.01), indicating highly microporous nature. The specific surface areas of 3D-CON and V2D-BBL structure were observed to be 1506 and 1530 $m^2 g^{-1}$, respectively. Compared to 3D-CON, the V2D-BBL structure revealed relatively high hysteresis between adsorption and desorption graphs. It is because pore surfaces of V2D-BBL structure has higher gas binding force than 3D-CON, which is attributed highly polarizable per in one group. Thermo gravimetric analysis (TGA) revealed that 3D-CON and V2D-BBL structures are thermally very stable under air and nitrogen. The decomposition temperatures of samples were found to be above 550 ℃, which is associated with formation of stable fused aromatic structures. Along with rigid nature of FANs and abundant hydrogen bonding sites toward water, such high surface area and exceptional thermal stability promotes us to use those materials as practical application, especially, kinetic hydrate inhibitors.

4.3.4. Onset temperature measurements on CH_4 and CO_2 hydrates

The hydrate onset temperatures of FANs were compared with conventional inhibitors (PVP and PVCap in Figure 4.3.3. The nucleation and growth histogram of CH_4 and CO_2 hydrates were measured by using the cooling ramping method (cooled down from 285.8 K to 270.7 K at 0.02 K/min). The lower the onset temperature indicates the better kinetic inhibition performance. As seen in CH_4 hydrate results, not only PVCap significantly inhibits the CH_4 hydrate nucleation, but also V2D-BBL delayed CH_4 hydrate formation and its kinetic inhibition effect is comparable to conventional inhibitors. It is because of the similar functional groups and advantages of three-dimensional features. It shows a great chance to interact with water molecules and structurally hinder the water networks for hydrate nucleation. The 3D-CON itself did not have functional groups, but it was confirmed that a certain degree of KHI effect may appear due to three-dimensional characteristics. Moreover, the onset temperatures of FANs indicate that their performances were much better at CO_2 hydrates. It indicates that the FAN-based inhibitors could be work at high sub-cooling condition, which is an example of overcoming the weakness of the polymer-based inhibitor. It should be suggested that the mechanism by which FANs inhibit hydrate nucleation is because of the similarity of functional groups and there are so many possible hydrogen bonding sites per area (3D-structure).

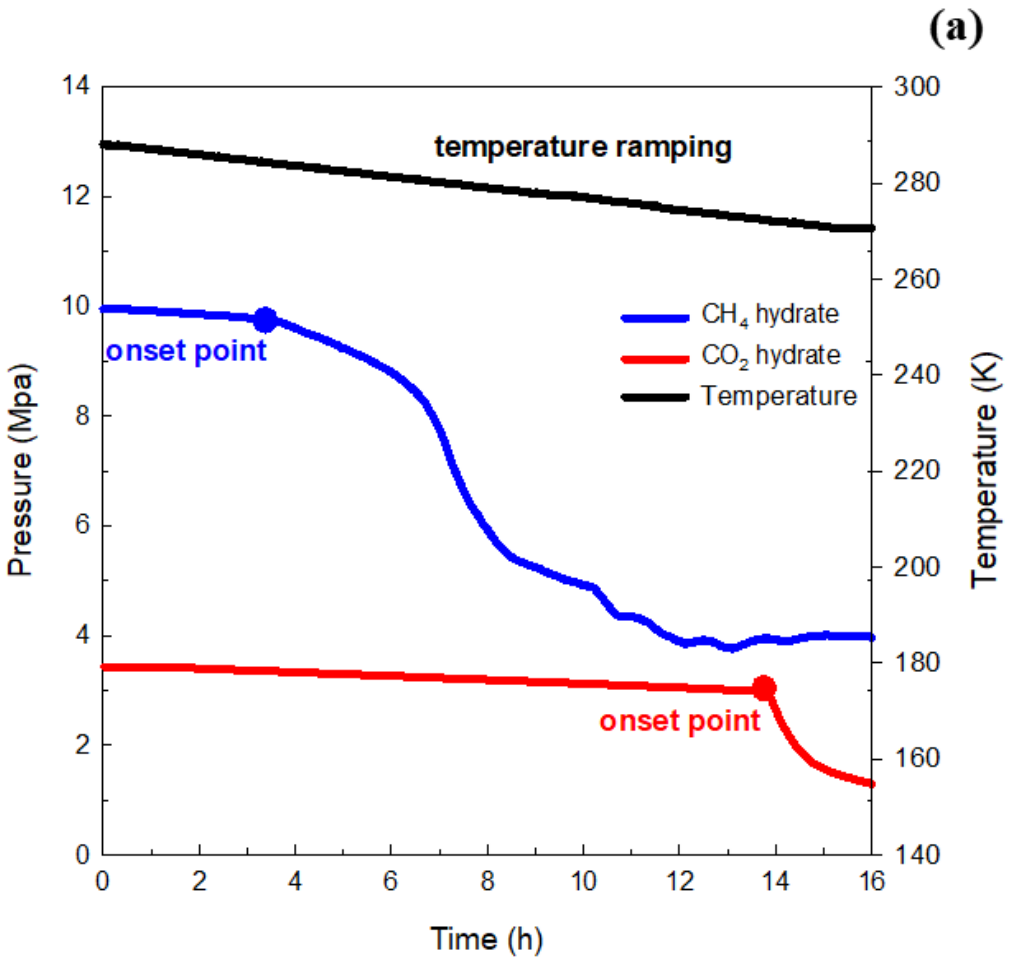

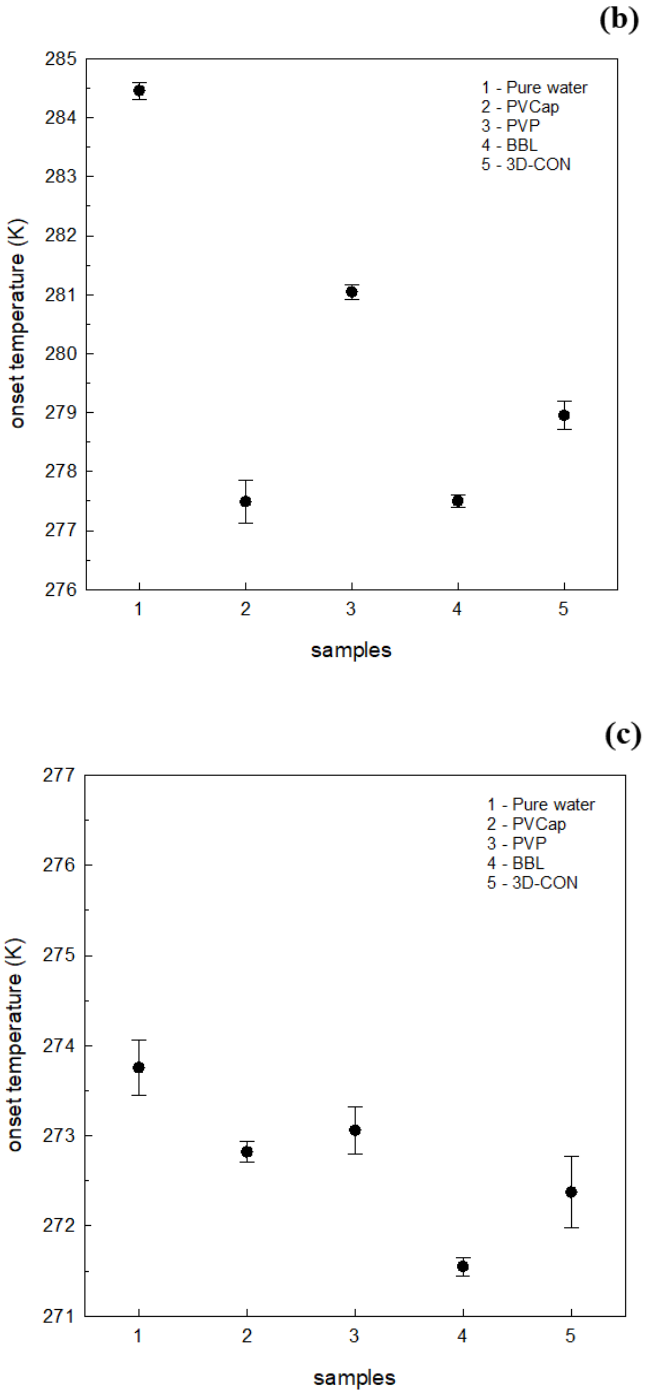

Figure 4.3.3. (a) Determination of the onset temperature for CH_4 and CO_2 hydrates, respectively, in the temperature-ramping method. onset temperatures of (b) CH_4 and (c) CO_2 hydrates in the presence of pure wate, PVCap, V2D-BBL and 3D-CON.

4.3.5. Infrared Raman (IR) results between inhibitor and water molecules

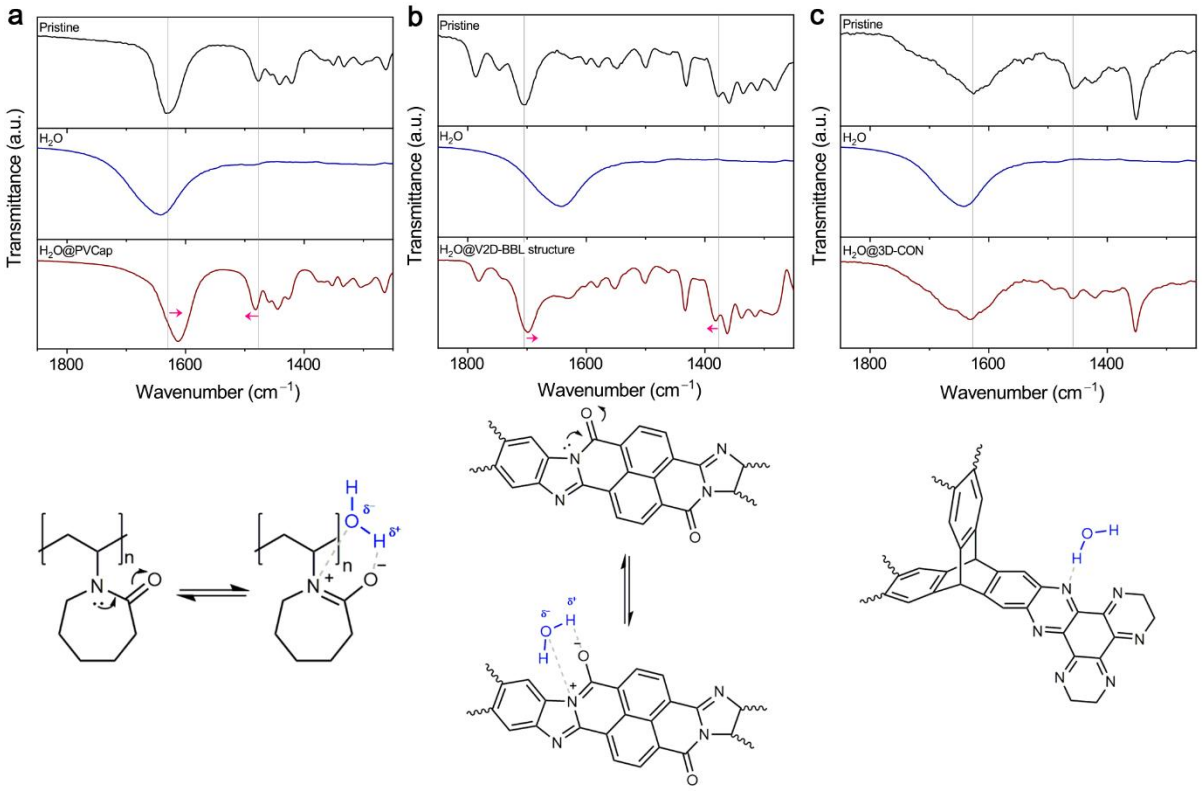

Figure 4.3.4. ATR-FTIR spectra (up) and proposed KHI mechanism (bottom) of (a) PVCap, (b) V2D-BBL structure and (c) 3D-CON, respectively.

Table 4.3.1. Wavenumber shifts of each inhibitor.

	PVCap	**PVP**	**V2D-BBL**	**3D-CON**
C=O bond	1632 cm^{-1} → 1612 cm^{-1}	1658 cm^{-1} → 1650 cm^{-1}	1705 cm^{-1} → 1698 cm^{-1}	-
C-N bond	1477 cm^{-1} → 1482 cm^{-1}	1493 cm^{-1} → 1496 cm^{-1}	1378 cm^{-1} → 1382 cm^{-1}	-
Note	Peak intensity changes occur (-C-H bonds)		C=N peak intensity increase	No change

To investigate the interaction sites toward water, ATR-FTIR spectra of samples were measured before/after water capture. The peak at 1632 cm^{-1} assigned to the carbonyl bond (C=O) in lactam ring dramatically shifts to 1612 cm^{-1} after uptake of water, because charge delocalization makes C=O bonds to C−O^-, indicating decrease of electron cloud density such as proposed structure in Figure 4.3.4. In addition, peak shift from 1477 to 1482 cm^{-1} was observed because C−N−C bond becomes like C=N^+−C after H_2O uptake. Due to this charge delocalization enables materials to interact well with water, PVCap shows good performance as KHI. The similar peak shifts in ATR-FTIR were found in case of the V2D-BBL structure. The peak shifts from 1704 to 1697 cm^{-1} occurred for carbonyl (C=O) group and C−N−C moiety in benzimidazole ring from 1378 to 1382 cm^{-1}. All of these peak shifts are strong evidence for charge delocalization like proposed structures. Meanwhile, 3D-CON exhibited no peak shift after water adsorption in ATF-FTIR, implying weak interaction with water as can be observed in less performance for KHIs. It is clear that superior performance of V2D-BBL structure comes from charge delocalization which makes strong interaction with water.

4.3.6. Inhibition mechanism verification in the presence of FANs

The cage-filling behavior of CH_4 molecules on the sI hydrate formation in the presence of V2D-BBL was examined to provide further insights into the inhibition mechanism after hydrate nucleation from in-situ Raman spectroscopy. Figure 4.3.5. indicated the growth patterns of a) pure CH_4 hydrate system and b) CH_4 hydrate + V2D-BBL system. For pure CH_4 hydrate, the Raman peaks appearing at 2905 cm^{-1} and 2915 cm^{-1} are corresponding to CH_4 molecules enclathrated in the large $5^{12}6^2$ and small 5^{12} cages of sI hydrate, respectively. Two peaks for pure CH_4 hydrate grow simultaneously after hydrate nucleation and increased gradually until 50 min (reached). Although the driving force ($\Delta P = 4.0$ K) for two systems is exactly the same, the growth patterns of CH_4 hydrate + V2D-BBL system are totally different from pure CH_4 hydrate. The enclathrated CH_4 molecules at small cages were easily shown at the early stage of hydrate formation, and the small cages gradually grow. However, the captured CH_4 molecules at the large cages were not observed during the hydrate growth. This growth pattern was shown to be very similar to the previously reported PVCap results. As is well known, PVCap has a significant influence on the growth of large cages due to its structural characteristics. V2D-BBL can also predict a similar trend due to the presence of hydrogen bonding spots similar to PVCap. Therefore, the Raman peaks appearing at 2905 cm^{-1} cannot be identified because there is a weak driving force to enclathrated in CH_4 molecules in the large cages. Further studies will cover this unusual growth trend in detail through molecular dynamics (MD).

4.3.7. Conclusions

In summary, we have developed a new class of a KHI, which is composed of an extended π-conjugated aromatic skeleton with rich benzimidazole rings and pyrrolidinone units. Moreover, high specific surface area of the prepared V2D-BBL structure makes abundant pyrrolidinone functional group interact with water well. When the V2D-BBL structure was tested as KHI, outstanding performance (onset: 277.6 K) was observed which is similar to commercial material (PVCap, onset: 277.5 K). Moreover, we suggested that these outstanding inhibition effect was caused by structural advantages regarding functional groups, 3D-dimensional effect, and cage-specific inhibition effect. We believe that promising performance as a KHI of the fused aromatic network (FAN) structure provides insights to design and develop more potential KHI materials in future.

Chapter 5. Conclusions and Future Works

5.1. Conclusions

In this study, under the theme of "Experimental and Computational Approaches for Prevention and Remediation of Gas Hydrates in the Presence of Novel Inhibitors", I propose a cage-specific inhibition effect, synergistic inhibition effect of amino acid + ionic acid, novel gas hydrate inhibitors through three different approaches. This subject is differentiated from other existing studies and will be helpful in future hydrate inhibitor studies as a reference for existing studies.

First, in Topic 1, the thermodynamic effects of glycine and [BMIM][BF_4] among amino acids and ionic acids and their inhibition effects were examined through microscopic and kinetic experiments, as well as the interaction between cage and inhibitor through density functional theory calculations. By calculating the energy, a cage-specific inhibition effect for each inhibitor was proposed. [BMIM][BF_4] gave more negative interaction energy between a cage and an inhibitor molecule, so it had a large potential to inhibit gas hydrate formation. Through these experiments, it was proved that glycine inhibited the enclathration of CH_4 into the large cage, and [BMIM][BF_4] hindered CH_4 molecules from occupying small (5^{12}) cages, whereas glycine had a strong influence on large ($5^{12}6^2$) cages of sI hydrates.

Based on this, stability condition, structural analysis, gas uptake, cage filling behavior, COSMO-RS, and onset temperature were measured to determine whether the combination of glycine + [BMIM][BF_4] exhibited synergistic effects as THI and KHI.

For THI experiments, it was confirmed that the mixture of glycine (1.5 mol%) + [BMIM][BF_4] (1.5 mol%) had no thermodynamic synergistic effect when used as THI, and the presence of inhibitor mixtures did not affect the structural characteristics of CH_4 hydrates because of their large molecular sizes. However, the glycine (1.5 mol%) + [BMIM][BF_4] (1.5 mol%) system showed that the conversion of water into gas hydrates and the formation rates of CH_4 hydrate were significantly influenced.

Besides, as a KHI, their mixture of glycine (0.5 wt%) + [BMIM][BF_4] (0.5 wt%) showed synergistic inhibition in nucleation (onset temperature), and it was confirmed that in terms of growth, it had a consequent slow growth rate of CH_4 hydrate. The cage-specific inhibition of glycine, which has a strong influence on large ($5^{12}6^2$) cages, and [BMIM][BF_4], which hinders CH_4 molecules from occupying small (5^{12}) cages, caused kinetic inhibition synergism from nucleation to growth. This topic reports a novel investigation of synergistic gas hydrate inhibition effects that demonstrate significant scientific and engineering advances in flow assurance for the oil and gas industry.

The following Topic 2 is a study that applies three new materials as gas hydrate inhibitors for the first

time and proves the inhibition effects of the unique physical and chemical properties of each material through computational approaches such as COSMO-RS, QTAIM, and MD. First, we used various UiO-66 derivatives having different functional groups to reveal the inhibition effect on gas hydrate formation and magnetic Fe_3O_4 nanoparticles were adopted to construct the core-shell type composite with MOFs as inhibitors for recoverability. From screening process, we measured the onset temperature of each inhibitor and revealed that UiO-66-NH_2 make hydrogen a bond with water showed the superior performance to PVP by disrupting the hydrogen-bonded water molecular networks. Furthermore, we showed that the Fe_3O_4@UiO-66-NH_2 was successfully synthesized and was easily recoverable, allowing reuse without significant deterioration of the inhibition performance.

DESs are generally formed by mixing HBDs with HBAs, which have great potential for use as effective and eco-friendly THIs because they have functional groups capable of forming hydrogen bonds with water, have low toxicity, exhibit negligible vapor pressure and exist in a liquid state (fluidity). From the stability condition measurement, it demonstrated that ChCl, urea, and DES contributed to the significant shift of hydrate equilibrium line and thus can function as effective THIs. Among them, ChCl and DES showed the potential as a substitute for methanol. Also, these thermodynamic properties were proved through the hydrogen bond energy (E_{HB}). The strength of hydrogen bonds was calculated by using a computational method called QTAIM, and this result was confirmed to be the same as the tendency of the stability condition measurements.

All of the newly reported KHIs described above delayed the time or onset temperature for nucleation of hydrates, but did not outperform PVCap alone. In other words, the development of new KHIs is highly desirable to replace PVCap for future industry with study on the interaction of inhibition mechanism. To overcome these issues, we employed two kinds of novel FAN materials as KHIs. Especially, V2D-BBL structure is structurally similar to lactam-based PVCap and increases the number of molecules capable of hydrogen bonding per surface area (3D-structure) to increase the effect of KHI. As can be seen from the results of the onset temperature, it was confirmed that V2D-BBL showed a good effect in terms of nucleation of CH_4 and CO_2 hydrates, and among them, it showed a very superior effect than conventional PVCap in CO_2 hydrate (high sub-cooling condition). Also, V2D-BBL, similar to PVCap, showed a cage-specific inhibition effect on a large cage, and experimentally proved that the structural characteristics of C=O and C-N-C bonds hinder the participation of CH_4 molecule in large cage. Further studies on molecular behavior that cannot be confirmed by experimental methods will be conducted by proving such cage-specific inhibition effects through MD.

The overall experimental and computational results obtained in this study are expected to understand a new avenue to design and develop novel class of gas hydrate inhibitors and may contribute toward

lessening the environmental impact of gas hydrate inhibition for oil and gas industries.

5.2. Future works

The development of a new gas hydrate inhibitor requires a proposal for a new concept and a complete understanding of the existing inhibitors. Although Topic 1 and 2 tried to approach these concepts and obtained reasonable results, the results and suggestions for sufficient hydrate inhibitors were not provided. Thus, more advanced experimental methods and materials will be applied for the development and understanding of hydrate inhibitors in future works.

The first research currently underway is to demonstrate the thermodynamic and kinetic mechanisms of PVCap through nucleation and dissociation behaviors. Injection of Poly(N-vinylcaprolactam) (PVCap) for an offshore oil field to prevent the risk of hydrate formation was well-known method. However, there are limited studies on gas hydrate formation and dissociation in the presence of PVCap. Thus, the formation and dissociation behaviors with different concentrations of PVCap considering phase equilibria, cage-specific inhibition effect and structure characteristics were studied in this paper. We measured phase equilibria in the presence of PVCap from high-pressure autoclave with different dissociation scanning rate. Then, we compared the formation-dissociation process in the presence of PVCap with a pure water system to understand inhibition and dissociation mechanisms. Furthermore, we measured PXRD patterns to understand the structure characteristics of methane hydrate with PVCap. From our view, PVCap leading to a higher dissociation temperature compared to pure methane hydrate. It could be suggested that the stability of gas hydrates increases when PVCap is added, which then takes longer to melt. It was confirmed that the MD results showed similar trends to those of the experimental results. In the case of PVCap, it participates in the growth of large cages during nucleation and prevents methane from entering, thereby inhibiting the growth of hydrate. In this case, the formed PVCap-based cage is thermodynamically stable and dissociates later than pure methane hydrate, which requires a lot of energy. As a result, it should be considered that further energy is needed to eliminate hydrate plugs formed under conditions where PVCap is applied. Therefore, future experiments will find the remediation methods to help dissociate the gas hydrate in the presence of PVCap.

In the second study, we try to propose a hydrate inhibition mechanism through the interaction of the guest-inhibitor, not the interaction of the water-inhibitor. A newly considered kinetic hydrate inhibitor based on hydrophobic anions and cations of ionic liquid (IL) has been proposed to prevent gas hydrate plugging. The kinetic inhibition effect of hydrophilic ILs such as [BMIM][BF_4], [BMIM][I], [EMIM][BF_4], and [EMIM][I] was well known, but inhibitor experiments for hydrophobic ILs did not

proceed. In this study, three different types of cations with [TF_2N^-] and [PF_6^-] were compared to understand the side chain effect and hydrophobicity effect. First, onset temperature and pressure drop were measured in the presence of hydrophobic ILs to investigate the inhibition effect. As can be seen by T_{onset}, hydrophobic IL has a very weak hydrogen bond strength with water, so it can be expected that it will have no effect on hydrate nucleation in general. However, as can be seen from the experimental results, they exhibit similar inhibition effects to Hydrophilic ILs. In addition, the in-situ Raman analysis was used to find the inhibition mechanism of hydrophobic ILs. Furthermore, synthesized inhibitors that take all the advantages of the above characteristics into consideration, we propose an inhibitor with a new inhibition mechanism. Since this is the first report of the use of hydrophobic ionic liquid as KHI, we expect that the use of hydrophobic IL can potentially be applied in offshore flow assurance strategies.

Lastly, in the future research, not only the research on transportation in the current industry (upstream, downstream), but also the CO_2 hydrate generated during CO_2 storage process will be conducted. Thus, we plan to look at the practical approach through THI/KHI blend as well as the application of CO_2 hydrate of representative THI and KHI currently used in the industry. CH_4 hydrate and CO_2 hydrate are sI hydrates, but there are differences in microscopic, kinetic, and thermodynamic characteristics, and problems that may occur during the input of the inhibitor have not been studied so far, so fundamental studies will be conducted for the future applications. Furthermore, since the present and future industries always have the goal of developing eco-friendly inhibitors, research on new materials, mechanisms and systems will be continued.

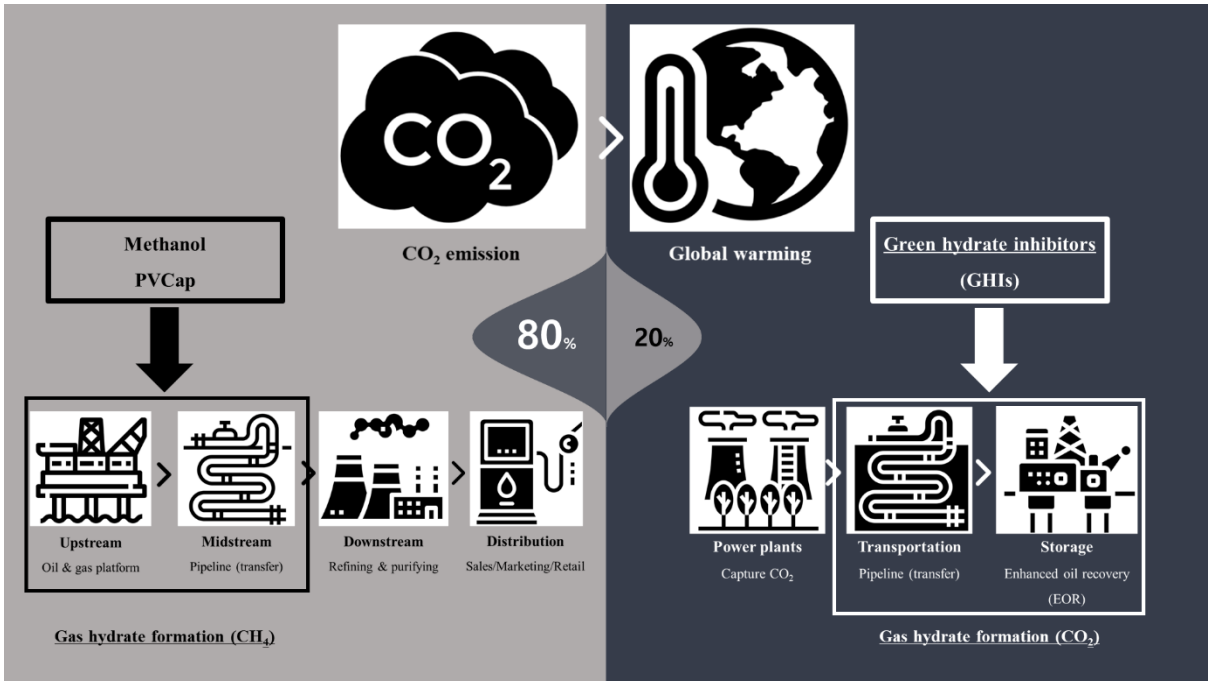

Figure 5.2.1. Future perspectives – for CO_2 hydrates

References

[1] Sloan ED, Koh CA. Clathrate hydrates of natural gases. 3rd ed. Boca Raton: CRC Press/Taylor & Francis; 2008.

[2] Lu H, Seo YT, Lee JW, Moudrakovski I, Ripmeester JA, Chapman NR, Richard BC, Gardner G, Pohlman J. Complex gas hydrate from the Cascadia margin. Nature 2007;445:303-6.

[3] Ripmeester JA, Tse JS, Ratcliffe CI, Powell BM. A new clathrate hydrate structure. Nature 1987;325:135-6.

[4] Yuan Q, Sun CY, Yang X, Ma PC, Ma ZW, Liu B, Chen GJ. Recovery of methane from hydrate reservoir with gaseous carbon dioxide using a three-dimensional middle-size reactor. Energy 2012:40:47-58.

[5] Jiang X, Li S, Zhang L. Sensitivity analysis of gas production from Class I hydrate reservoir by depressurization. Energy 2012;39:281-5.

[6] Koh CA, Sloan ED, Sum AK, Wu DT. Fundamentals and applications of gas hydrates. Annu Rev Chem Biomol Eng 2011;2:237–57

[7] Linga P, Adeyemo A, Englezos P. Medium-pressure clathrate hydrate/membrane hybrid process for postcombustion capture of carbon dioxide. Environ Sci Technol 2007;42:315-20.

[8] Kim S, Kang SP, Seo Y. Semiclathrate-based CO_2 capture from flue gas in the presence of tetra-n-butyl ammonium chloride (TBAC). Chem Eng J 2015;276:205-12.

[9] Xu CG, Li XS. Research progress of hydrate-based CO_2 separation and capture from gas mixtures. RSC Adv 2014;4:18301-16

[10] Babu P, Linga P, Kumar R, Englezos P. A review of the hydrate based gas separation (HBGS) process for carbon dioxide pre-combustion capture. Energy 2015;85:261-79.

[11] Sun D, Ripmeester J, Englezos P. Phase equilibria for the $CO_2/CH_4/N_2/H_2O$ system in the hydrate region under conditions relevant to storage of CO_2 in depleted natural gas reservoirs. J Chem Eng Data 2016;61:4061-7.

[12] Kim NJ, Lee JH, Cho YS, Chun W. Formation enhancement of methane hydrate for natural gas transport and storage. Energy, 2010;35:2717-22.

[13] Linga P, Kumar R, Englezos P. The clathrate hydrate process for post and pre-combustion capture of carbon dioxide. J Hazardous Mater 2007;149:625-9.

[14] Hao W, Wang J, Fan S, Hao W. Evaluation and analysis method for natural gas hydrate storage and transportation processes. Energy Convers Manag 2008;49:2546-53.

[15] Kang SP, Lee H. Recovery of CO_2 from flue gas using gas hydrate: thermodynamic verification through phase equilibrium measurements. Environ Sci Technol 2000;34:4397-4400.

[16] Dashti H, Yew LZ, Lou X. Recent advances in gas hydrate-based CO_2 capture. J Nat Gas Sci Eng

2015;23:195-207.

[17] Cha JH, Seol Y. Increasing gas hydrate formation temperature for desalination of high salinity produced water with secondary guests. ACS Sustain Chem Eng 2013;1:1218-24.

[18] Park KN, Hong SY, Lee JW, Kang KC, Lee YC, Ha MG, Lee JD. A new apparatus for seawater desalination by gas hydrate process and removal characteristics of dissolved minerals (Na^+, Mg^{2+}, Ca^{2+}, K^+, B^{3+}). Desalination 2011;274:91-6.

[19] Corak D, Barth T, Høiland S, Skodvin T, Larsen R, Skjetne T. Effect of subcooling and amount of hydrate former on formation of cyclopentane hydrates in brine. Desalination 2011;278:268-74.

[20] Lee D, Lee Y, Lee S, Seo Y. Accurate measurement of phase equilibria and dissociation enthalpies of HFC-134a hydrates in the presence of NaCl for potential application in desalination. J Korean Chem Soc 2016;33:1425-30.

[21] Sloan ED, Koh CA, Sum AK. Natural gas hydrates in flow assurance. Gulf Professional Publishing; 2010

[22] Zerpa LE, Salager JL, Koh CA, Sloan ED, Sum AK. Surface chemistry and gas hydrates in flow assurance. Ind Eng Chem Res 2010;50:188-97.

[23] Mokhatab S, Wilkens RJ, Leontaritis KJ. A review of strategies for solving gas-hydrate problems in subsea pipelines. Energy Source Part A 2007;29:39-45.

[24] Kelland MA. Production chemicals for the oil and gas industry. 2nd ed. CRC press; 2014

[25] Cha M, Shin K, Kim J, Chang D, Seo Y, Lee H, Kang SP. Thermodynamic and kinetic hydrate inhibition performance of aqueous ethylene glycol solutions for natural gas. Chem Eng Sci 2013;99:184-90.

[26] Masoudi R, Tohidi B, Anderson R, Burgass RW, Yang J. Experimental measurement and thermodynamic modelling of clathrate hydrate equilibria and salt solubility in aqueous ethylene glycol and electrolyte solutions. Fluid Phase Equilib 2004;219:157-63.

[27] Sum AK, Sandler SI. Ab initio calculations of cooperativity effects on clusters of methanol, ethanol, 1-propanol, and methanethiol. J Phys Chem A 2000;104:1121-9.

[28] Kelland MA. History of the development of low dosage hydrate inhibitors. Energy Fuels 2006;20:825-47.

[29] Del Villano, L, Kommedal, R, Kelland, MA. Class of kinetic hydrate inhibitors with good biodegradability. Energy Fuels 2008;22:3143-9.

[30] Lederhos JP, Long JP, Sum A, Christiansen RL Sloan ED. Effective kinetic inhibitors for natural gas hydrates. Chem Eng Sci 1996;51:1221-9.

[31] Hammerschmidt EG. Formation of gas hydrates in natural gas transmission lines. J Ind Eng Chem 1934;26:851-5.

[32] Sloan ED. A changing hydrate paradigm—from apprehension to avoidance to risk management.

Fluid Phase Equilibr 2005;228:67-74.

[33] Creek JL. Efficient hydrate plug prevention. Energy Fuels 2012;26:4112-6.

[34] Chong ZR., Chan AHM, Babu P, Yang M, Linga P. Effect of NaCl on methane hydrate formation and dissociation in porous media J Nat Gas Eng 2015;27:178-89.

[35] Zhao X, Qiu Z, Zhou G, Huang W. Synergism of thermodynamic hydrate inhibitors on the performance of poly (vinyl pyrrolidone) in deepwater drilling fluid. J Nat Gas Eng 2015;23:47-54.

[36] Mohammadi AH, Richon D. Gas hydrate phase equilibrium in the presence of ethylene glycol or methanol aqueous solution. Ind Eng Chem Res 2010;49:8865-9.

[37] Anderson, FE, Prausnitz, JM. Inhibition of gas hydrates by methanol. AIChE journal 1986;32:1321-33.

[38] Perrin A, Musa OM, Steed JW. The chemistry of low dosage clathrate hydrate inhibitors. Chem Soc Rev 2013;42:1996-2015.

[39] Sa JH, Melchuna A, Zhang X, Rivero M, Glénat P, Sum AK. Investigating the effectiveness of anti-agglomerants in gas hydrates and ice formation. Fuel 2019;255:115841.

[40] Daraboina N. Linga P. Experimental investigation of the effect of poly-N-vinyl pyrrolidone (PVP) on methane/propane clathrates using a new contact mode. Chem Eng Sci 2013;93:387-94.

[41] Daraboina N, Pachitsas S, von Solms N. Natural gas hydrate formation and inhibition in gas/crude oil/aqueous systems. Fuel 2015;148:186-90.

[42] Huo Z, Freer E, Lamar M, Sannigrahi B, Knauss DM, Sloan ED. Hydrate plug prevention by anti-agglomeration. Chem Eng Sci 2001;56:4979-91.

[43] Gao S. Hydrate risk management at high watercuts with anti-agglomerant hydrate inhibitors. Energy Fuels 2009;23:2118-21.

[44] Khan MS, Lal B, Bavoh CB, Keong LK, Bustam A. Influence of ammonium based compounds for gas hydrate mitigation: a short review. Indian J Sci Technol 2017;10:1-6.

[45] Yagasaki T, Matsumoto M, Tanaka H. Adsorption mechanism of inhibitor and guest molecules on the surface of gas hydrates. J Am Chem Soc 2015;137:12079-85.

[46] Xu J, Li L, Liu J, Wang X, Yan Y, Zhang J. The molecular mechanism of the inhibition effects of PVCaps on the growth of sI hydrate: an unstable adsorption mechanism. Phys Chem Chem Phys 2018;20:8326-32.

[47] Xu S, Fan S, Fang S, Wang Y, Lang X. Excellent synergy effect on preventing CH4 hydrate formation when glycine meets polyvinylcaprolactam. Fuel 2017;206:19-26.

[48] Kvamme BB, Huseby G, Forrisdahl OK. Molecular dynamics simulations of PVP kinetic inhibitor in liquid water and hydrate/liquid water systems. Mol. Phys. 1997;90:979-92.

[49] Anderson BJ, Tester JW, Borghi GP, Trout BL. Properties of inhibitors of methane hydrate formation via molecular dynamics simulations. J Am Chem Soc 2005;127:17852-62.

[50] Kim KS, Kang JW, Kang SP. Tuning ionic liquids for hydrate inhibition. ChemComm 2011;47:6341-3.

[51] Sa JH, Kwak GH, Han K, Ahn D, Cho SJ, Lee JD, Lee, KH. Inhibition of methane and natural gas hydrate formation by altering the structure of water with amino acids. Sci Rep 2016;6:31582.

[52] Lee W, Shin JY, Kim KS, Kang SP. Kinetic promotion and inhibition of methane hydrate formation by morpholinium ionic liquids with chloride and tetrafluoroborate anions. Energy Fuels 2016;30:3879-85.

[53] Furukawa H, Cordova KE, O'Keeffe M, Yaghi OM. The chemistry and applications of metal-organic frameworks. Science 2013;341:1230444.

[54] Farha, Lee JK. Roberts OJ, Scheidt KA, Nguyen ST, Hupp JT. Metal–organic framework materials as cata-lysts. Chem Soc Rev 2009;38:1450-9.

[55] Czaja AU, Trukhan N, Müller U. Industrial applications of metal–organic frameworks. Chem Soc Rev 2009;38:1284-93.

[56] Guillerm V, Ragon F, Dan-Hardi M, Devic T, Vish-nuvarthan M, Campo B, Vimont A, Clet G, Yang Q, Maurin G, Férey G, Vittadini A, Gross S, Serre CA. Series of isoreticu-lar, highly stable, porous zirconium oxide based metal–organic frameworks. Angew Chem Int Ed 2012;51:9267-71.

[57] Wu H, Yildirim T, Zhou W. Exceptional mechanical stability of highly porous zirconium metal–organic framework UiO-66 and its important implications. J Phys Chem Lett 2013;4:925-30.

[58] Kandiah N, Nilsen MH, Usseglio S, Jakobsen S, Ols-bye U, Tilset M, Larabi C, Quadrelli EA, Bonino F, Lillerud KP. Synthesis and stability of tagged UiO-66 Zr-MOFs. Chem Mater 2010:22:6632-40.

[59] Katz MJ, Brown ZJ, Colón YJ, Siu PW, Scheidt KW, Snurr RQ, Hupp JT, Farha OK. A facile synthesis of UiO-66, UiO-67 and their derivatives. Chem Commun 2013;49:9449-51.

[60] Miao Z, Qi C, Wensley AM, Luan Y. Development of a novel Brønsted acid UiO-66 metal–organic framework catalyst by post synthetic modification and its application in catalysis. RSC Adv 2016;6:67226-31.

[61] Sowa B, Zhang XH, Kozielski KA, Hartley PG, Dunstan DE, Maeda N. Nucleation probability distributions of methane–propane mixed gas hydrates in salt solutions and urea, Energ Fuel 2015;29:6259-70.

[62] Muromachi S, Abe T, Maekawa T, Yamamoto Y. Phase equilibrium for clathrate hydrate formed in methane+ water+ urea system. Fluid Phase Equilibr 2015;398:1-4.

[63] Mohamed NA, Tariq M, Atilhan M, Khraisheh, G. Rooney, D. Garcia, G. Aparicio S. Investigation of the performance of biocompatible gas hydrate inhibitors via combined experimental and DFT methods. J Chem Thermodyn 2017;111:7-19.

[64] Tariq M, Atilhan M, Khraisheh M, Othman E, Castier M, García G, Aparicio S, Tohidi B. Experimental and DFT approach on the determination of natural gas hydrate equilibrium with the use of excess N_2 and choline chloride ionic liquid as an inhibitor. Energy Fuels 2016;30:2821-32.

[65] Abbott AP, Capper G, Davies DL, Rasheed RK, Tambyrajah V. Novel solvent properties of choline chloride/urea mixtures. Chem Comm 2003;1:70-1.

[66] Zhu A, Jiang T, Han B, Zhang J, Xie Y, Ma X. Supported choline chloride/urea as a heterogeneous catalyst for chemical fixation of carbon dioxide to cyclic carbonates. Green Chem 2007;9:169-72.

[67] Mahmood J, Anjum MAR, Baek JB. Fused aromatic network structures as a platform for efficient electrocatalysis. Adv Mater 2019;31:1805062.

[68] Ahmad I, Li F, Kim C, Seo JM, Kim G, Mahmood J, Baek JB. Robust fused aromatic pyrazine-based two-dimensional network for stably cocooning iron nanoparticles as an oxygen reduction electrocatalyst. Nano Energy 2019;56:581-7.

[69] Mahmood J, Lee EK, Jung M, Shin D, Jeon IY, Jung SM, Park N. Nitrogenated holey two-dimensional structures. Nat commun 2015;6:1-7.

[70] Mahmood J, Kim SJ, Noh HJ, Jung SM, Ahmad I, Li F, Baek JB. A robust 3D cage-like ultramicroporous network structure with high gas-uptake capacity. Angew Chem Int Ed 2018;57:3415-20.

[71] Noh HJ, Im YK, Yu SY, Seo JM, Mahmood J, Yildirim T, Baek JB. Vertical two-dimensional layered fused aromatic ladder structure. Nat Commun 2020;11:1-8.

[72] Daraboina N, Malmos C, von Solms N. Synergistic kinetic inhibition of natural gas hydrate formation. Fuel 2013;108:749-57.

[73] Sa JH, Kwak GH, Lee BR, Park DH, Han K, Lee KH. Hydrophobic amino acids as a new class of kinetic inhibitors for gas hydrate formation. Sci Rep 2013;3:2428.

[74] Sa JH, Lee BR, Park DH, Han K, Chun HD, Lee KH. Amino acids as natural inhibitors for hydrate formation in CO_2 sequestration. Environ Sci Technol 2011;45:5885-91

[75] Sa JH, Kwak GH, Han K, Ahn D, Lee KH. Gas hydrate inhibition by perturbation of liquid water structure. Sci Rep 2015;5:11526.

[76] Xiao C, Wibisono N, Adidharma H. Dialkylimidazolium halide ionic liquids as dual function inhibitors for methane hydrate. Chem Eng Sci 2010;65:3080-7.

[77] Shin BS, Kim ES, Kwak SK, Lim JS, Kim KS, Kang JW. Thermodynamic inhibition effects of ionic liquids on the formation of condensed carbon dioxide hydrate. Fluid Phase Equilib 2014;382:270-8.

[78] Adisasmito S, Frank III RJ, Sloan ED. Hydrates of carbon dioxide and methane mixtures. J Chem Eng Data 1991;36:68-71.

[79] Kumar P, Mishra BK, Sathyamurthy N. Density functional theoretic studies of host–guest

interaction in gas hydrates. Comput Theor Chem 2014;1029:26-32.

[80] Seo YT, Lee H. ^{13}C NMR analysis and gas uptake measurements of pure and mixed gas hydrates: Development of natural gas transport and storage method using gas hydrate. Korean J Chem Eng 2003;20:1085-91.

[81] Lee D, Go W, Seo Y. Experimental and computational investigation of methane hydrate inhibition in the presence of amino acids and ionic liquids. Energy 2019;182:632-40.

[82] Bavoh CB, Partoon B, Lal B, Gonfa G, Khor SF, Sharif AM. Inhibition effect of amino acids on carbon dioxide hydrate. Chem Eng Sci 2017;171:331-9.

[83] Man MS, Abdullah MAM, Abdullah SB, Yaacob Z. Screening Cation and Anion of Ionic Liquid for Dissolution of Silicon Dioxide using COSMO-RS. Indian J Sci Technol 2017;10;1-6.

[84] Khan MS, Bavoh CB, Partoon B, Lal B, Bustam MA, Shariff AM. Thermodynamic effect of ammonium based ionic liquids on CO_2 hydrates phase boundary. J Mol Liq 2017;238:533-9.

[85] Mullins E, Oldland R, Liu YA, Wang S, Sandler SI, Chen CC, Zwolak M, Seavey KC. Sigma-profile database for using COSMO-based thermodynamic methods. Ind Eng Chem Res 2006;45:4389-415.

[86] Daraboina N, Malmos C, von Solms N. Investigation of kinetic hydrate inhibition using a high pressure micro differential scanning calorimeter. Energy Fuels 2013;27:5779-86.

[87] Maeda N, Kelland MA, Wood CD. Ranking of kinetic hydrate inhibitors using a high pressure differential scanning calorimeter. Chem Eng Sci 2018;183:30-6.

[88] Kang SP, Jung T, Lee JW. Macroscopic and spectroscopic identifications of the synergetic inhibition of an ionic liquid on hydrate formations. Chem Eng Sci 2016;143:270-5.

[89] Del Villano L, Kelland MA. An investigation into the kinetic hydrate inhibitor properties of two imidazolium-based ionic liquids on Structure II gas hydrate. Chem Eng Sci 2010;65:5366-72.

[90] Hong SY, Lim JI, Kim JH, Lee JD. Kinetic studies on methane hydrate formation in the presence of kinetic inhibitor via in situ Raman spectroscopy. Energy Fuels 2012;26:7045-50.

[91] Katz MJ, Brown ZJ, Colón YJ, Siu PW, Scheidt KA, Snurr RQ, Farha OK. A facile synthesis of UiO-66, UiO-67 and their derivatives. Chem Commun 2013;49:9449-51.

[92] Miao Z, Qi C, Wensley AM, Luan Y. Development of a novel Brønsted acid UiO-66 metal–organic framework catalyst by postsynthetic modification and its application in catalysis. RSC Adv 2016;6:67226-31.

[93] Zhu X, Gu J, Wang Y, Li B, Li Y, Zhao W, Shi J. Inherent anchorages in UiO-66 nanoparticles for efficient capture of alendronate and its mediated release. Chem Commun 2014;50:8779-82.

[94] Zhao HX, Zou Q, Sun SK, Yu C, Zhang X, Li RJ, Fu YY. Theranostic metal–organic framework core–shell composites for magnetic resonance imaging and drug delivery. Chem Sci 2016;7:5294-301.

[95] Reinsch H, van der Veen MA, Gil B, Marszalek B, Verbiest T, de Vos D, Stock N. Structures,

Sorption characteris-tics, and nonlinear optical properties of a new series of highly stable aluminum MOFs. Chem Mater 2013;25:17-26.

[96] Wright AM, Reith AJ, Yang S, Wang EN, Dincă M. Precise control of pore hydrophilicity enabled by post-synthetic cation exchange in metal-organic frameworks. Chem Sci 2018;9:3856-9.

[97] Kalmutzki MJ, Diercks CS, Yaghi OM. Metal-organic frameworks for water harvesting from air. Adv Mater 2018;30:1704304.

[98] Nassu RT, Gonçalves LAG. Determination of melting point of vegetable oils and fats by differential scanning calorimetry (DSC) technique. Grasas Aceites 1999;50:16-21.

[99] Naumann C. Brumm T. Bayerl TM. Phase transition behavior of single phosphatidylcholine bilayers on a solid spherical support studied by DSC, NMR and FT-IR. Biophys J 1992;63:1314-9.

[100] Durand E. Lecomte J. Villeneuve P. Deep eutectic solvents: Synthesis, application, and focus on lipase-catalyzed reactions. Eur J Lipid Sci Tech 2013;115:379-85.

[101] Klamt A. Eckert F. COSMO-RS: a novel and efficient method for the a priori prediction of thermophysical data of liquids. Fluid Phase Equilibr 2000;172:43-72.

[102] Abbott AP, Capper G, Davies DL, Rasheed RK, Tambyrajah V. Novel solvent properties of choline chloride/urea mixtures. Chem Comm 2003;1:70-1.

[103] Sa JH., Kwak GH, Han K, Ahn D, Cho SJ, Lee JD, Lee KH. Inhibition of methane and natural gas hydrate formation by altering the structure of water with amino acids. Sci Rep 2016;6:31582.

[104] Teixeira AM, de Oliveira Arinelli LE, de Medeiros JL, Ofélia de Queiroz FA. Recovery of thermodynamic hydrate inhibitors methanol, ethanol and MEG with supersonic separators in offshore natural gas processing. J Nat Gas Sci Eng 2018;52:166-86.

[105] Bavoh CB, Nashed O, Khan MS, Partoon B, Lal B, Sharif AM. The impact of amino acids on methane hydrate phase boundary and formation kinetics. J Chem Thermodyn 2018;117:48-53.

[106] Qasim A, Khan MS, Lal B, Ismail MC, Rostani K. Quaternary ammonium salts as thermodynamic hydrate inhibitors in the presence and absence of monoethylene glycol for methane hydrates. Fuel 2020;259:116-219.

[107] Espinosa E, Molins E, Lecomte C. Hydrogen bond strengths revealed by topological analyses of experimentally observed electron densities. Chem Phys Lett 1998;285:170-3.

[108] Becke A. The quantum theory of atoms in molecules: from solid state to DNA and drug design. John Wiley & Sons; 2007.

[109] Bavoh CB, Lal B, Nashed O, Khan MS, Keong LK, Bustam MA. COSMO-RS: An ionic liquid prescreening tool for gas hydrate mitigation. Chin J Chem Eng 2016;24:1619-24.

Acknowledgement

My greatest debt is to prof. Yongwon Seo. As my dissertation advisor, I will not forget his continuous support and assistance. He gave me thoughtful advice as a researcher, which motivated me to do my research. The gifts the professor taught me will be of great guideline to my future life and I will try to become a better researcher.

I would like to thank the examining committee of my Ph.D. thesis/dissertation, prof. Youngnam Kwon, prof. Sungdeuk Choi, prof. Hoi Ri Moon, and Dr. Seungmin Lee. Their varied advice and perspective have helped to strengthen my research and broaden my research field.

Thank you to my fellow ACE lab mates who gave me great motivation and support during my Ph.D. study. My colleagues are more enthusiastic about research than anyone else and they are a great teacher to each other, so I hope to keep a good relationship with each other in the future.

Lastly, I would like to express my gratitude to my family. Thank you, mom and dad, for your generous support and endless love. Without their encouragement I could not accomplish the Ph.D. degree. I give my all honor to them. And, final voted of thanks must go to my wife and son, whose support in every respect has stimulated me to work harder. I will do my best for their happiness in the future life